POTENTIAL VORTICITY DYNAMICS DRIVING VARIABILITY IN MEAN TIDAL

CURRENTS FLOWING THROUGH BOUNDED ESTUARINE CHANNELS

BY

KATHERINE A. KIRK

BS, Cornell University, 2012

MEng, Cornell University & Woods Hole Oceanographic Institution, 2013

DISSERTATION

Submitted to the University of New Hampshire

in Partial Fulfillment of

the Requirements for the Degree of

Doctor of Philosophy

in

Oceanography

December 2023

ii

This dissertation has been examined and approved in partial fulfillment of the requirements for the degree of Doctor of Philosophy in Oceanography by:

Dissertation Director, Dr. Thomas Lippmann, Professor
UNH Department of Earth Sciences

Dr. James Pringle, Professor
UNH Department of Earth Sciences

Dr. Diane Foster, Director
UNH School of Marine Science and Ocean Engineering

Dr. Tracy Mandel, Assistant Professor
UNH Ocean and Mechanical Engineering

Dr. John Kelley
UNH CCOM, Affiliate Research Professor
NOAA National Ocean Service's Office of Coast Survey, Physical Scientist

Dr. Gregory Dusek
Senior Scientist
NOAA National Ocean Service's Center for Operational Oceanographic Products and Services

On December 4, 2023

Original approval signatures are on file with the University of New Hampshire Graduate School.

DEDICATION

I dedicate this work and any success I may have had to all of my family members, especially my late mother, Diane Kelly Kirk, who will forever be my role model and my father, Ed Kirk Jr, who taught me to sail and inspired my love of being on, in, and near the water. Also to my late grandfather, Ed Kirk Sr., whose support and welcoming household was essential in helping me get to where I am today. You valued your education and set the standard of hard work, perseverance, and optimism. Thank you.

ACKNOWLEDGEMENTS

TABLE OF CONTENTS

LIST OF TABLES

LIST OF FIGURES

ABSTRACT

POTENTIAL VORTICITY DYNAMICS DRIVING VARIABILITY IN MEAN TIDAL

CURRENTS FLOWING THROUGH BOUNDED ESTUARINE CHANNELS

by

Katherine A. Kirk

University of New Hampshire, December, 2023

Tidally induced pressure gradients in sea level drive mean estuarine tidal currents that can have horizontal spatial variability across a bounded channel or inlet. Strong cross-channel gradients in along-channel mean velocity set up extremums in the background potential vorticity that can support instabilities of tidal currents flowing through narrow, bounded estuarine channels and tidal inlets. In addition, conservation of potential vorticity including frictional terms, results in intensification of along-channel tidal currents over shallow lateral shelves. In the first part of this dissertation (Chapter 2), the dispersion equation of barotropic instabilities of tidal currents is analytically solved for simple bathymetry defined by idealized and variable channel geometries that include lateral shelves. The solution is third-order and the cross-channel velocity structure, bathymetry, and geometry can be altered to approximate typical natural inlet geometries allowing for a range of scenarios to be examined. The resulting fastest growing unstable modes have wavelengths of $O(10^2$ m$)$, periods of $O(10^2$ - 10^3 s$)$, and growth rates of $O(10^{-3}$ - 10^{-2} s$^{-1})$ with phase speeds approximately one third of the maximum velocity, consistent with instabilities of longshore currents studied in the nearshore (Bowen and Holman, 1989; Dodd and Thornton, 1990). In the second part of this dissertation (Chapter 3), the presence of instabilities of tidal currents is

observed from a spatially lagged along-channel array consisting of seven current meters and pressure sensors deployed in the Hampton-Seabrook Inlet, NH for one week encompassing the spring tides in May 2021. Using iterative maximum likelihood estimators, wavenumber-frequency spectra are estimated during 3-4 hour time periods with approximately steady currents on both the flood and ebb tides. Dominant wavenumbers ($\pm$ 0.002 - 0.02 m^{-1}) of the low frequency motions (0.0006 - 0.01 s^{-1}) with corresponding wavelengths ($\pm$ 314.2 – 3141.6 m) and periods (628.3 – 10472 s) are resolved and consistent with motions estimated in Chapter 2. The lack of breaking wave group modulations within the inlet and the presence of the seaward (shoreward) propagating instabilities on the ebb (flood) flow indicate that the presence of the instabilities can be attributed to the shear of the tidal current. In the third part of the dissertation (Chapter 4), a numerical hydrodynamic model (ROMS) is used to better understand the forcing mechanisms driving intensification of velocity over the shallow lateral shelf in the Piscataqua River observed from ADCP transects obtained in 2015 during both the flood and ebb of the spring tide. Results show that the along-channel flow is intensified (convergence of streamlines) over the lateral shelf under high Reynolds number conditions, where the inertial forces dominate over the frictional and viscous forces, during both quasi-steady flooding and ebbing currents. Given the cross-channel structure of the velocity, the water circulates up onto the shelf by the conservation of potential vorticity. Due to the shallower depth over the shelf, the velocities increase due to conservation of volume, which leads to even stronger horizontal shear in the mean along-channel tidal currents. The spatial and temporal variability in mean tidal currents (consistent with instabilities of the flow) results from the background potential vorticity that mixes momentum horizontally across the channel and smooths the cross-channel velocity structure; thus, the potential vorticity balance leads to both velocity intensification over the shelf and unstable motions. Changes to the mean flow

structure and mixing by instabilities have implications for estuarine dynamics such as the fate and transport of organic and inorganic matter, navigational safety, and tidal energy resource assessment.

CHAPTER I

1   INTRODUCTION

Astronomical tidal forcing leads to pressure gradients in sea level that drive mean tidal currents throughout estuaries, where outgoing fresh, buoyant, riverine discharge is exchanged and mixed with incoming dense, saline ocean water leading to horizontal and vertical mixing, tidal exchange, and estuarine circulation. Herein, the mean tidal current refers to the time averaged flow over at least one hour and up to four hours during either an ebb or flood current. The tidal currents transport organic and inorganic substances, including sediment, pollutants, nutrients, and larvae. Sediment transport, in particular, leads to areas of deposition and erosion significantly altering bed geometry and bed form migration. The local bathymetry and topography impacts the tidal currents as the frictional stresses dampen the velocity. Understanding the tidal currents and having accurate tidal current predications is critical for emergency managers to quickly respond to oil spills and other natural disasters that involve the transport of harmful substances. Policy makers also need to make informed decisions regarding restoration efforts that may depend on the transport of larvae into or out of various habitats and ecosystems. Additionally, mariners rely on tidal current information to safely navigate increasingly larger ships through harbors and restricted channels with limited maneuverability. Accurate estimates of the tidal currents is also important for tidal energy resource assessments that depend on the velocity to the third power, but these assessments typically don't take into account the temporal variability about the mean current.

Variations in the mean tidal current are caused by both changes in tidal phases (e.g. spring and neap, perigee and apogee, lunar nodal cycle) and non-tidal effects (e.g. wind, storms, waves, nonlinearities, unstable motions). Relative to the dominant tidal current frequency (i.e. one cycle every 12.42 hour for semidiurnal tides), these variations can be characterized as high frequency

variability (e.g. unstable turbulent motions) or low frequency variability (e.g. the 18.6 year lunar nodal cycle) about the mean current. It is important to characterize and quantify the spatial and temporal variability in the mean tidal current on time scales ranging a few minutes to several hours to fully understand the fluid dynamics throughout an estuary and the consequential implications on other processes.

Areas with a large tidal range, such as the Gulf of Maine, can have fast tidal current velocities, especially in narrow channels bounded by land or jetties leading to reversing, rectilinear currents. Two study site locations within the Gulf of Maine are considered in this thesis: the Hampton-Seabrook Inlet (HSI) and the lower Piscataqua River in the Great Bay Estuary. Both sites are known for experiencing strong tidal currents (> 2 m/s), especially on the spring tides, and are further described in Sections 3.3 and 4.3, respectively.

Tidal currents flowing through a narrow inlet or channel bounded by land or manufactured structures (e.g. jetties) can have strong horizontal, cross-channel gradients in the along-channel flow. A small disturbance in the velocity gradient can cause the mean flow to become unstable leading to a meandering of the mean along-channel current and potentially the spinoff of large eddies of $O(10^1 - 10^2$ m). This instability and the resulting high-frequency variability of the currents and vorticities may affect small vessel navigation, the transport of organic and inorganic matter, and cause lateral mixing of momentum across the inlet. In Chapter 2, the dispersion of the linear instabilities of tidal current are solved analytically for a given range of wavenumbers. The frequencies associated with unstable motions were determined under various idealized channel geometries and bathymetry that includes lateral shelves. The restoring force for the unstable motions is the background potential vorticity, which here is dominated by the relative vorticity

while the planetary vorticity is ignored. The instabilities lead to horizontal mixing that smooths the cross-channel velocity structure (and can have consequential impacts on ecosystem transport).

In Chapter 3, instabilities of the mean current are observed in HSI using a seven-element array of current meters and pressure sensors. The dominant wavelengths and periods are estimated from iterative maximum likelihood estimators and compared with theoretical linear stability predictions discussed in Chapter 2. The instabilities are observed on both the ebb and flood tide, and propagate in the direction of the mean flow. The forcing is from the strong gradient in velocity and is not tied to breaking incident gravity wave groups that are absent in the inlet, indicating that the restoring force is due to the conservation of potential vorticity.

In Chapter 4, an intensification of velocity over a shallow lateral shelf on the northern side of the Piscataqua River off Henderson Point south of Seavey Island is investigated. Observations show fast currents over the shallow area as opposed to occurring in the adjacent deeper channel during both the flood and ebb tidal current stages. In deeper water where bottom friction has a smaller influence on the depth-averaged currents, it is often expected that the topography would result in the strongest currents in the deeper channel. A numerical hydrodynamic model is used to solve the 3-dimensional momentum equations to simulate the flow and better understand the forcing mechanisms driving the intensification of current magnitude over the shelf. The conservation of volume and potential vorticity are used to better understand the flow dynamics. The consequential mixing of momentum across the channel is also studied and expected to lead to smoothing of the cross-channel current structure. This study will help the research community better understand the physical forcing causing mean tidal current spatial variability, which can have implications for tidal energy resource assessments, navigation, and the fate and transport of matter.

The theme of this dissertation is the analysis of the spatial and temporal variability of the tidal currents about the mean and the role of the potential vorticity balance in driving the flow circulation and unstable nature. Chapter 2 is comprised of an analytical linear instability analysis that results in a general solution for the dispersion of unstable infragravity motions flowing through bounded estuarine channels or inlets. Chapter 3 is an analysis of unstable infragravity motions based on observations collected in an array deployed in the HSI in 2021. Chapter 4 utilizes a numerical hydrodynamic model to solve the 3-dimensional momentum equations to determine the forcing mechanisms driving an intensification of velocity over a lateral shelf in the Piscataqua River as observed in data collected in 2015. It is worth noting the coordinate system varies between Chapter 2 where the along- and cross-channel flow are in the y- and x-directions, respectively, following much of the nearshore literature orientation, while in Chapter 4 the along- and cross-channel flow are in the x- and y-directions, respectively, following the ROMS convention. Finally, general introduction (Chapter 1) and unified conclusion (Chapter 5) sections are included.

CHAPTER II

2 ANALYTICAL LINEAR INSTABILITY ANALYSIS OF LATERALLY BOUNDED, HORIZONTALLY SHEARED TIDAL CURRENTS

2.1 Abstract

Tidal currents flowing through narrow inlets and channels can have horizontal cross-channel velocity gradients that produce a background potential vorticity field that supports instabilities in the mean flow. This results in a meandering of the tidal currents along the channel that can lead to lateral mixing of momentum and transport and potentially the spinoff of large (nonlinear) eddies. Analytical solutions for linear barotropic instabilities were found for idealized cross-channel structure in along channel tidally driven flow in bounded inlets with variable inlet geometry. Analytic solutions are general and shown to converge to previous solutions for surf zone alongshore currents and are consistent with solutions for shelf currents at the continental slope. The generalized dispersion equation is third-order and depends on the wavenumber, maximum current magnitude, horizontal shear of the current, cross-inlet geometry and bathymetry, and a linear friction coefficient. The cross-channel velocity, bathymetry, and geometry can be altered to approximate typical natural inlet geometries allowing for a range of scenarios to be examined. For bounded tidal currents with inviscid flow, the characteristic wavelengths are order of magnitude, $O(10^2$ m$)$, periods are $O(10^2$ - 10^3 s$)$, and growth rates of the fastest growing unstable modes are $O(10^{-3}$ - 10^{-2} s$^{-1})$ with phase speeds approximately one third of the maximum velocity, similar to prior nearshore findings where the scales of the flow and bathymetry are of the same order as found in inlets. Bottom friction suppresses the unstable motions leading to slower initial growth rates and a reduced range of unstable wavenumbers. Faster growing modes with a larger range of

unstable wavenumbers and stronger horizontal mixing (represented by the cross-channel Reynolds shear stress) occur under stronger shear conditions and cross-channel bathymetry with wide, deep shelves. The Reynolds stress is inversely proportional to the strength of the background potential vorticity field dependent on the cross-channel shear of the along channel flows. At the location of maximum flow, horizontal mixing acts to smooth the initial velocity cross-channel structure. Stronger mixing by the instabilities occurs in the areas of higher lateral current shear. Results suggest that tidal currents in inlets will produce unstable modes that can mix momentum laterally, impacting transport of particulate and dissolved organic and inorganic matter through the inlet.

2.2 Introduction

Coastal and estuarine tidal currents vary both temporally and spatially as a function of tidal forcing, bottom friction, surface stress (e.g. wind and atmospheric effects), bathymetric variation across the inlet, and nonlinear interactions with nontidal forcing such as river discharge or storm surge (Parker, 2007). Tidal currents and their variability have long been known to be important to mixing and transport between inland bays and freshwater systems and the coastal ocean (Bowden, 1965; Simpson et al., 1990; Geyer and MacCready, 2014), navigation routes and safety (Chen et al., 2013), and marine hydrokinetic energy resources (Lalander et al., 2013). Yet, little attention has been given to the details of the cross-inlet structure of the inlet flow.

Tidal currents flowing through narrow inlets and channels can have horizontal velocity gradients that produce a background potential vorticity field that supports instabilities in the mean flow. This could result in a meandering of the tidal current along the channel and potentially the spinoff of large (nonlinear) eddies (Figure 2.1). Both the linear instabilities and consequential nonlinear vortices provide a mechanism for horizontal mixing of momentum that may significantly impact the circulation, modify the cross-shore or cross-channel mean velocity profile and affect

6

dispersion and transport of organic and inorganic matter, including pollutants similar to nearshore surf zone alongshore currents (Dodd et al., 2000). Dodd and Thornton (1990) found that when instabilities of the surf zone longshore current are present and Reynolds stresses of the shear instabilities are nonzero, energy is transferred from the background flow to the perturbed flow leading to a mixing of momentum and modification to the mean current. Consequences of mixing include impacts not only on transport of matter, but also on renewable energy initiatives since hydrokinetic energy is dependent on the velocities to the third power (Lalander et al., 2013) and likely to be strongly impacted by the presence of strong instabilities.
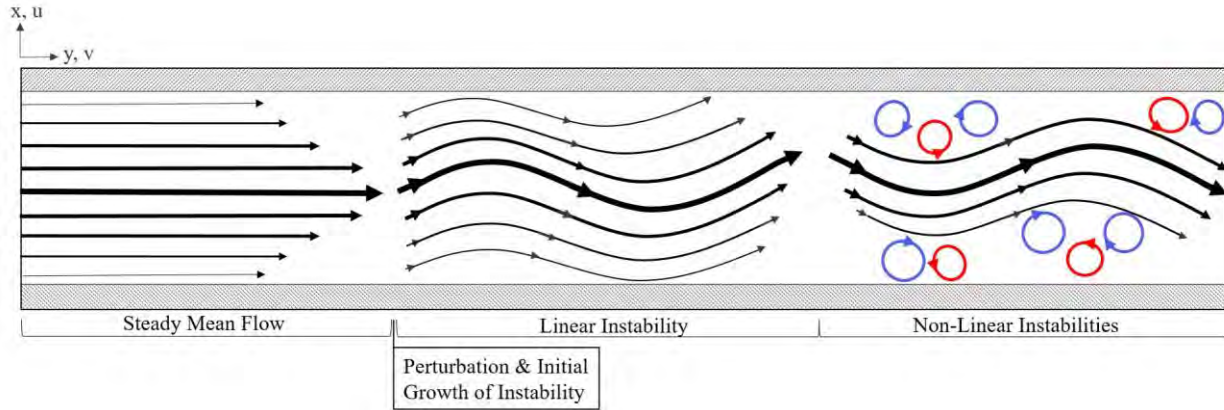
Figure 2.1. Simple schematic of the depth averaged along-channel mean stable flow (left), unstable linear flow (middle), and unstable non-linear flow with the spin-off of vorticities (right) through a bounded channel.

Linear instability analysis has previously been applied to alongshore currents on the continental shelf, nearshore and estuarine environments. Niiler and Mysak (1971) first examined barotropic non-divergent oscillations along the continental shelf in the western North Atlantic Ocean driven by the potential vorticity structure. Bowen and Holman (1989) modified Niiler and Mysak's (1971) dispersion equation for the instability motions by ignoring the Coriolis force and rescaling the flow to be representative of wave-driven alongshore currents in the surf zone. The

resulting instabilities were characterized as highly coherent, alongshore propagating, horizontal wave-like motions that are dependent on the longshore current strength, shear, and direction (Bowen and Holman, 1989; Dodd et al., 2000; Baquerizo et al., 2001). Characteristic frequencies are of order of magnitude, O, $(10^{-3} – 10^{-2}$ Hz), with alongshore wavelengths of $O(10^2$ m), and were first observed in the nearshore by Oltman-Shay et al. (1989). These low frequency motions are distinguished from alongshore progressive, low frequency surface gravity waves (i.e. edge and leaky waves) in that the wavenumbers are much larger than the lowest mode edge waves, and the instability surface elevations are negligible (Oltman-Shay et al., 1989; Bowen and Holman, 1989; Dodd and Thornton, 1990; Dodd et al., 1992). Linear instabilities are non-dispersive as the phase speed, c_p, does not depend on the frequency, but instead varies linearly as a fraction of the magnitude of the maximum current, V_{max}, varying between $0.25 < c_p/V_{max} < 0.9$ based on theoretical, observational, and numerical studies (Oltman-Shay et al., 1989; Bowen and Holman, 1989; Dodd et al., 1992, 2000; Falqués and Iranzo, 1994). Similar scales of motion are expected in the tidal inlet as that in the nearshore while the forcing of the mean flow is not wave-driven and instead primarily forced by the tidal-induced pressure gradient at the inlet mouth.

Work in riverine environments has extensively looked at instabilities that lead to bed forms (Callander, 1969; Nelson, 1990; Seminara, 2010), channel meandering or channel braiding (Blondeaux and Seminara, 1985; Parker and Andrews, 1986; Lanzoni and Seminara, 2006; Seminara, 2010), as well as instabilities that develop as a result of flow around headlands (Signell and Geyer, 1991). Analysis of both the vorticity balance along with the transfer of kinetic energy between the mean flow and turbulence gave insight into the dynamics of cross-stream circulation cells and resulting streamwise vortical motions that arise in curved channel flows (Blanckaert and De Vriend, 2004). In our theoretical work, the straight channel is assumed alongshore uniform

with non-erodible banks and bed boundaries, and the motions are progressive; therefore, this analysis focuses on the mean flow and not on the sediment transport and subsequent channel and bedform migration resulting from instabilities. Here, we solve the linear stability analysis for unstable (complex) frequencies and real-valued wavenumbers, greatly simplifying the mathematics (similar to nearshore applications with steady, uniform alongshore currents and straight and parallel bathymetric contours; Dodd and Falqués, 1996).

Estuarine work has focused on baroclinic shear instabilities in the flow produced from stratified density layers leading to vertical mixing and reduction in vertical variations in shear and stratification (Geyer and Smith, 1987; Seim and Gregg, 1994; Bourgault et al., 2001; Geyer et al., 2010). However, Mied et al. (2006) examined the horizontal stability of quasi-barotropic, inviscid, tidally driven flow through a straight channel. They found the analytical stability solutions aligned with remote observations of instabilities that had O(1 km) wavelengths and growth time scales on the order of 10% of the half period of the dominant M_2 tidal constituent and the vortices remained present for more than half of the M_2 tidal cycle leading to mixing of the flow across the river for several hours. It is expected that the analytical solutions solved in the bounded tidal inlet herein will result in similar growth time scales relative to the M_2 period.

In this work, the temporal variability of tidal currents in narrow inlets and channels with lateral shear in the mean along-channel tidal current is examined. The mean tidal current is defined herein as the average observed flow over a quasi-steady state during a flooding or ebbing tide. The cross-channel shear leads to unstable currents that may strongly modulate the flows at time scales much less than used to compute the mean consistent with similar situations on the continental shelf and surf zone (Niiler and Mysak, 1971; Bowen and Holman, 1989; and many others). We

analytically examine the expected behavior of linear barotropic instabilities for idealized cross-channel geometries that lead to a generalized solution for typical inlets in shallow water.

2.3 Methods

Following Bowen and Holman (1989), an analytical linear instability analysis was conducted that depends on the cross-shore gradient of the background potential vorticity in order to determine the expected wavenumbers, k, and frequencies, σ, of the fastest growing shear instability modes. Starting with the equations for shallow water (depth integrated) two-dimensional (x and y-direction) horizontal momentum equations, the following assumptions are applied: (1) simple linearized bottom friction, (2) horizontal eddy viscosity is neglected, (3) the Coriolis force is neglected since a characteristic shear instability frequency, σ, is much greater than Coriolis, f, at mid-latitude (i.e. $\frac{\sigma}{f} \approx \frac{10^{-2}}{10^{-4}} = 10^2$ m), (4) the flow is non-divergent (rigid-lid) since horizontal fluxes are assumed to be larger than the temporal rate of change in sea surface elevation, (5) the perturbation velocities are small compared to the mean tidal current (here, the mean is calculated over a quasi-steady state of a flooding or ebbing tide), (6) second order nonlinear terms are omitted, and (7) the along-channel length is infinitely long.

The rigid lid approximation based on non-divergent flow is considered to be a good assumption since the relative magnitude of the non-rigid lid terms are small for typical scales of inlet depths and current magnitudes. The numerical analysis by Falqués and Iranzo (1994) found that the surface oscillations due to the instabilities are small and more specifically, the rigid lid assumption is valid for small local Froude numbers, << 1, which corresponds to gravity waves having shorter periods than the instability motions. Here, the Froude number is small, F $\approx \frac{1}{10} <<$ 1 based on characteristic scales of inlet depths and current velocity.

10

In this analytical approach, the horizontal eddy mixing terms are neglected and dissipation is through the linear bottom friction term. It is expected that bottom friction will suppress the instabilities by reducing the initial growth rate of all of the unstable modes and reduce the range of unstable wavenumbers (Dodd et al., 1992; Falqués and Iranzo, 1994; Özkan-Haller and Kirby, 1999; Baquerizo et al., 2001). Although Falqués and Iranzo (1994) found the dampening effects of eddy viscosity on the frequencies and phase speeds of the instabilities to be greater than bottom friction for both planar and barred beaches, in shallow estuaries bottom friction is believed to be the dominate dissipation force of tidal flow (Scarlatos, 1993; Geyer et al., 2000). Furthermore, Özkan-Haller and Kirby (1999) found the mixing caused by the instabilities to be stronger than the mixing induced by the eddy viscosity terms. Based on results found by Falqués and Iranzo (1994) and Özkan-Haller and Kirby (1999), it is expected that the inclusion of eddy mixing would dampen the growth rates causing less energetic, longer along-channel motions due to a decrease in the high-wavenumber oscillations, and slightly slower phase speeds.

Under our assumptions, the depth-integrated horizontal momentum equations including bottom shear stress are given by

$$u'_t + \boldsymbol{u} \cdot \nabla u' = -g\eta_x - \tau_x^b$$

$$v'_t + \boldsymbol{u} \cdot \nabla v' = -g\eta_y - \tau_y^b$$

(2.1)

where x and y are the cross-channel and along-channel directions, respectively, the total flow, $\boldsymbol{u}$, is a combination of the steady along-channel tidal current, V(x), and a small perturbation of the flow, $u'(x, y, t)$ and $v'(x, y, t)$, where u', $v' \ll$ V, the sea surface elevation is η(x,y,t), and g is gravity. The bottom shear stress, τ_x^b, τ_y^b, are parametrized similarly to Özkan-Haller and Kirby (1999)

$$\tau_x^b \equiv \frac{\lambda}{h} u' \qquad\qquad \tau_y^b \equiv \frac{\lambda}{h} v' \tag{2.2}$$

with the bottom friction, $\lambda = C_f |V_m|$, defined by a linear bottom drag coefficient, C_f, and the maximum current, V_m. For this analysis, the maximum velocity is set to 1 m/s, so $\lambda = C_f$ and ranges from 0 (i.e. inviscid flow) to 0.01, consistent with the range of estimates of bed shear stress coefficients in the nearshore environment (0.001 − 0.009; Thornton and Guza, 1986; Whitford and Thornton, 1996; Özkan-Haller and Kirby, 1999), as well as in tidal estuaries (0.001 − 0.01; Ludwick, 1975; Winterwerp and Wang, 2013), with similar V_m and water depth.

Since the flow is considered to be non-divergent and incompressible, the continuity equation is reduced to

$$\nabla \cdot (h\boldsymbol{u}) = 0 \tag{2.3}$$

and the velocity can be represented in terms of a stream function

$$(hu') = -\psi_y$$

$$(hv') = \psi_x \tag{2.4}$$

where $\nabla \times \psi = (h\boldsymbol{u})$.

Cross-differentiating and subtracting the momentum equations (2.1) cancels the sea surface elevation, η, and substituting in the stream function leads to

$$\left(\frac{\partial}{\partial t} + V\frac{\partial}{\partial y} + \frac{\lambda}{h}\right)\left(\frac{\psi_{yy}}{h} + \left(\frac{\psi_x}{h}\right)_x\right) = \psi_y \left(\frac{V_x}{h}\right)_x - \frac{\psi_x}{h}\left(\frac{\lambda}{h}\right)_x \tag{2.5}$$

This equation can be shown to be the linearized version of the conservation of potential vorticity

$$\frac{D}{Dt}(\pi_s) = \left(\frac{\partial}{\partial t} + \boldsymbol{u} \cdot \nabla\right)\left(\frac{\zeta + V_x}{h}\right) = -\frac{\lambda}{h}\frac{\zeta}{h} - v'\left(\frac{\lambda}{h}\right)_x \tag{2.6}$$

Where $\pi_s \equiv \frac{\zeta + V_x}{h}$ and $\zeta = (v'_x - u'_y)$. When the flow is inviscid and thus $\lambda = 0$, $\frac{D}{Dt}(\pi_s) = 0$.

The potential vorticity, π_s, is comprised of the relative potential vorticity, $\frac{\zeta}{h}$, and the background potential vorticity, $\frac{V_x}{h}$, which here is dependent on the shear of the current, V_x (Bowen and Holman, 1989; Dodd and Thornton, 1990; Baquerizo et al., 2001). The right hand side of (2.6) shows the dependence of the growing instabilities on the relationship between the perturbation velocities and potential vorticity modified by the friction force (Dodd et al., 2000).

The solution is assumed to be wave-like

$$\psi = Re\{\psi(x)e^{i(ky-\sigma t)}\} \tag{2.7}$$

where Re indicates the real components. The phase speed, c,

$$c = \frac{\sigma}{k} \tag{2.8}$$

is made up of a complex radian frequency, σ, and a real wavenumber, k, since growth of the motions in time is assumed. It is acknowledged that spatially growing modes (vs. temporal) may be more representative of the physical motions; however, Dodd and Falqués (1996) have shown that the temporal modes are simpler to solve mathematically, yet are still good predictors of the spatially fastest growing modes. Furthermore, they showed that the spatial growth rates can be estimated from the temporal growth rates using relationships developed by Gaster (1962) given small growth rates and no singularities in the complex wavenumber – frequency domain.

When σ has a positive imaginary solution, an instability may develop with exponentially growing amplitude (Niiler and Mysak, 1971; Bowen and Holman, 1989; Oltman-Shay et al.,

1989). The necessary criteria for unstable solutions is the presence of an extremum in the background potential vorticity (Niiler and Mysak, 1971; Bowen and Holman, 1989; Dodd et al., 1992; Baquerizo et al., 2001; Vallis, 2017). Substitution of the assumed wave-like solution (2.7) into the conservation of potential vorticity (2.5) yields

$$\left(V - \frac{i}{k}\frac{\lambda}{h} - c\right)\left(\psi_{xx} - k^2\psi - \psi_x \frac{h_x}{h}\right) = h\psi \left(\frac{V_x}{h}\right)_x - \frac{i}{k}\frac{\lambda}{h}\frac{h_x}{h}\psi_x \qquad (2.9)$$

also given in Dodd et al. (1992). Analytic solutions to (2.9) for arbitrary bathymetry and spatial current structure must be solved numerically for natural situations (as in Dodd et al., 1992). However, the general behavior of the linear instabilities can be solved analytically for simple flat bottom profiles with linear alongshore current shear within each cross-inlet region (as in Niiler and Mysak, 1971; Bowen and Holman, 1989; Baquerizo et al., 2001).

In our work, we discretize the cross-inlet profile into four regions, each defined by a flat bottom profile with given depth and width, and current structure confined to the center two regions with variable maximum location (Figure 2.2). The simple inlet configuration can be altered to approximate many natural inlet geometries through the various variables; modifying region widths $(x_0, \gamma_1, \gamma_2)$ and depths (h, α_0, $\alpha_1, \alpha_2, \alpha_3$) allows for the presence (or absence) of lateral topographic shelves, the maximum current velocity magnitude, V_m, can be changed and the fractional location of V_m across the inlet, δ, which can be placed on the shelf, at the shelf break, or in the main channel. Figure 2.2 shows the parameters defining the geometry and the associated background potential vorticity field. Note that in the presence of regions on either side of the channel where the mean along-channel current goes to zero, there are two extremums in background potential vorticity (Figure 2.2, lower panel) due to shear on either side of the maximum current leading to the possibility of instabilities on either side of the maximum current.
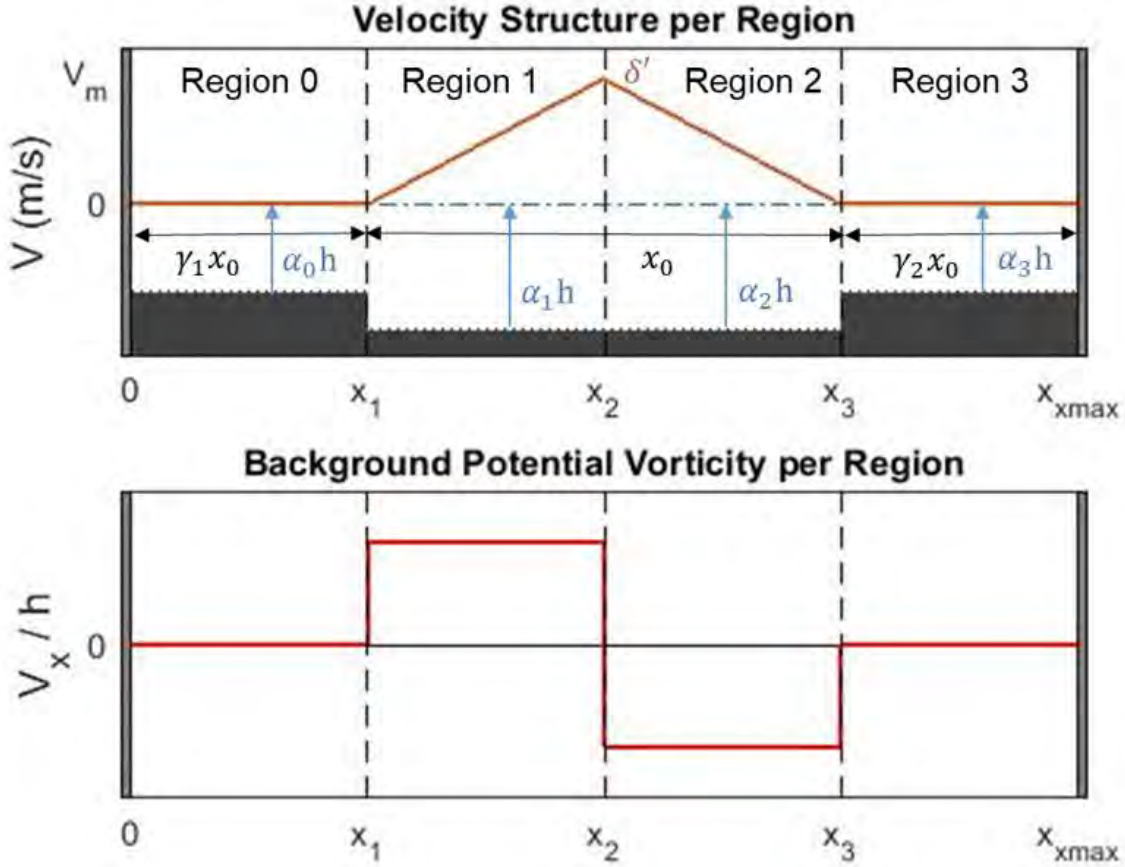
Figure 2.2. The top panel shows the along-channel depth integrated tidal current velocity (V, orange) variation across a bounded channel in the x-direction, which is broken down into four regions (labeled and separated by black dotted lines at x_1, x_2, and x_3, which are defined in Table A-1 in Appendix A). The width of the tidal current is set to x_0. The maximum tidal current is set to V_m and occurs at $x_2 = x_0(\gamma_1 + \delta)$ allowing for variability in shear through δ. The depth (h) is flat within each region, but can vary from region to region as a function of alpha (α). The bottom panel shows the background potential vorticity $\left(\frac{V_x}{h}\right)$ across the channel in the x-direction.

In each of the four regions, (2.9) reduces to the Rayleigh equation

$$\Psi_{xx} - k^2\Psi = 0 \tag{2.10}$$

with solutions given for each region as

Region 0: $\qquad\qquad \psi_0 = A_0 \sinh(kx)$

15

Region 1: $$\psi_1 = A_1 \sinh(kx) + B_1 \cosh(kx)$$

Region 2: $$\psi_2 = A_2 \sinh(kx) + B_2 \cosh(kx) \tag{2.11}$$

Region 3: $$\psi_3 = A_3[\sinh(kx) - \tanh(kx_{max}) \cosh(kx)]$$

where x_{max} is the total cross-inlet distance.

Coefficients, A_0, A_1, B_1, A_2, B_2, A_3, are found by matching conditions at the region boundaries and assuming that the stream function and the sea surface elevation are continuous (following Bowen and Holman, 1989; Baquerizo et al., 2001), resulting in an additional boundary condition given by the following, where the subscript i denotes the region.

$$\eta_i = -\frac{1}{g\alpha_i h}\left[\left(V - \frac{i}{k}\frac{\lambda}{\alpha_i h} - \frac{\sigma}{k}\right)\psi_{ix} - V_x\psi_i\right] \tag{2.12}$$

Boundary conditions at region borders are given in Appendix A: Boundary Conditions.

Solutions for the coefficients were found and are given in Appendix B: Coefficient Equations. Solutions for the complex radian frequency give a third-order dispersion equation of the form $a\sigma^3 + b\sigma^2 + c\sigma + d = 0$ (Appendix C: Cubic Solution) that depends on wavenumber, maximum current magnitude, horizontal shear of the current, cross-inlet geometry, and linear friction coefficient, i.e. $\sigma = f(k, V_m, \delta, x_0, \lambda, h, \alpha_0, \alpha_1, \alpha_2, \alpha_3, \gamma_1, \gamma_2)$. The three roots to the cubic polynomial can be comprised of either three real roots and zero imaginary roots, or one real root and two imaginary roots that are complex conjugates. In order for an exponentially growing instability to develop, there must be a positive imaginary root to the cubic dispersion equation. The wavenumber and frequency combinations that lead to unstable solutions for various shear, inlet geometries, depth profiles, and friction coefficients are discussed in the results section below.

For the fastest growing modes and initial growth rates, the stream function and resulting velocities are calculated using (2.7) and (2.4), respectively. Following Bowen and Holman (1989), the phase of the velocities are also calculated using the following

$$\theta_{u'} = \tan^{-1}\left(\frac{\psi_{re}}{\psi_{im}}\right) \qquad\qquad \theta_{v'} = \tan^{-1}\left(\frac{-\psi_{x_{im}}}{\psi_{x_{re}}}\right) \qquad\qquad (2.13)$$

$$\theta_{uv} = \theta_{v'} - \theta_{u'} \qquad\qquad (2.14)$$

The time averaged (indicated by the overbar) Reynolds shear stress of the perturbation velocities (2.4) is calculated by

$$S_{yx_j} = \overline{\int_0^x u'\, v'\, dx} \qquad\qquad (2.15)$$

and shows the relative magnitude of mixing of along-channel (y-direction) momentum across the channel (x-direction) resulting from the shear instabilities and subsequent transferring of energy from the mean flow to the perturbed flow. The Reynolds shear stress is solved within each region, where the depth, h, is constant, and the region boundaries are $x_j = [0, x_1, x_2, x_3, x_{max}]$.

$$S_{yx} = \frac{k}{2h^2}\int_{x_j}^{x_{j+1}} \psi_{im}(\psi_{re})_x - \psi_{re}(\psi_{im})_x\, dx \qquad\qquad (2.16)$$

The wavenumber, k, is chosen to be the wavenumber associated with the fastest growing mode of the initial growth rates. In order to analytically account for the time average and simulate averaging over a wave period, the Reynolds stress was averaged over one wavelength associated with the fastest growing mode, $L_{max} = \frac{2\pi}{k_{max}}$, in the along channel, y, direction similar to methods used by Dodd and Thornton (1990) and Church et al. (1992).

2.4 Results

The unstable modes occur when one of the three roots of the tertiary dispersion equation has a positive imaginary component. The solution (Appendix C: Cubic Solution) yields a range of positive imaginary frequencies associated with a range of wavenumbers that make up a continuum of unstable modes. The individual mode within this domain with the maximum imaginary frequency is referred to as the fastest growing mode (FGM) and has an associated wavenumber, k_{FGM}. Changes in the variables (shear, inlet geometry, bathymetry, and friction) affect the range of wavenumbers associated with positive imaginary radian frequencies as well as the fastest growing mode as discussed in more detail below.

2.4.1 Comparison to Prior Work

In order to check the dispersion relation solution (Appendix C: Cubic Solution), the cubic equation of the form $a\sigma^3 + b\sigma^2 + c\sigma + d = 0$ was reduced to the quadratic solution ($a\sigma^2 + b\sigma + c = 0$) that Bowen and Holman (1989) solved in the nearshore over a flat bottom with no friction ($\lambda = 0$; Appendix D: Reducing the Cubic Equation to Quadratic). This is done by setting Region 0 width to zero and Region 3 width to infinity, i.e. $\gamma_1 = 0$, $\gamma_2 = \infty$, respectively. Numerically, if Region 3 is set to a width of π or greater, the result is the equivalent to setting the width to infinity since $\tanh(\pi) \approx 1$. To set a flat bottom across the channel in all regions, the fraction of depth, $\alpha_i h$, in every region is set to one, $\alpha_0 = \alpha_1 = \alpha_2 = \alpha_3 = 1$. The resulting quadratic equation matches Bowen and Holman (1989) along with the complex radian frequency solutions for a range of real wavenumbers.

Baquerizo et al. (2001) extended Bowen and Holman's analysis by adding a fourth region and thereby having an additional extremum in the background potential vorticity and found the

18

dispersion equation to be cubic, as we did here. The Baquerizo et al. (2001) solutions can be replicated numerically using the cubic dispersion equation solved here for the tidal inlet problem by varying Region 0 width, allowing for a seaward boundary extending to infinity, setting the bathymetry to be flat and ignoring friction. It is also found that with very narrow Region 0 widths, two unstable curves emerge in the positive imaginary radian frequencies, which Baquerizo et al. (2001) attributed to the additional extremum in the background vorticity allowing for instabilities to be generated from both the frontshear (i.e. shear on the shoreward side of the maximum current) and backshear (i.e. shear on the seaward side of the maximum current), respectively. For larger Region 0 widths, there is one unstable curve allowing for a larger range of unstable wavenumbers similar to the tidal inlet solutions.

In Niiler and Mysak's (1971) continental shelf problem, four regions were defined leading to two extremums in background potential vorticity. They varied the bathymetry allowing for the first two regions in the west to be shallower mimicking a shelf and the last two regions in the east to be deeper. The maximum current occurred on the edge of the shelf. This can be simulated numerically in the tidal inlet problem by setting the depth in Regions 0 and 1 to half of the total depth (i.e. $\alpha_0 = \alpha_1 = 0.5$) in Regions 2 and 3 (i.e. $\alpha_2 = \alpha_3 = 1.0$) and having equal shear in Regions 1 and 2 (i.e. $\delta = 0.5$), putting the maximum current speed on the edge of the shelf. Region 0, 1, and 2 widths are all equal and Region 3 width extends to infinity as a seaward boundary (i.e. $\gamma_1 = 0.5$, $x_0 = 100$, $\gamma_2 = \infty$). Simulating the continental shelf problem using the tidal inlet solution would serve as another check on the cubic frictionless solution; however in order to exactly replicate Niiler and Mysak's (1971) instability motions, the Coriolis force would need to be included in the potential vorticity and the scales of motion would be need to be rescaled, considerably complicating the analysis (and not pursued herein).

Compared to the nearshore problem, the bounded tidal inlet over a flat bottom has a wider range of wavenumbers that have unstable roots, specifically at low wavenumbers (Figure 2.3). For shear profiles $\delta = 0.1 - 0.5$ over a flat bottom, the initial growth rate is faster in the bounded tidal inlet than the FGM in the nearshore (Figure 2.3). However, shear profiles $\delta = 0.6 - 0.9$ show the opposite where the nearshore growth rate exceeds the tidal inlet growth rate (Figure 2.3). Both the bounded inlet and nearshore have the FGM under strong shear conditions, which aligns with prior results (Bowen and Holman, 1989; Baquerizo et al., 2001). The bounded inlet shows symmetry in the frequency solutions when changing the shear profile, δ, from one side of the inlet to the other, e.g. $\delta = 0.1 = 0.9$, $\delta = 0.2 = 0.8$, and so on. This is attributed to having the flow bounded on either side versus in the nearshore where there is an exponentially infinite seaward boundary. When the nearshore is broken into three regions, the seaward shear is found to be more important than the shoreward shear (Dodd and Thornton, 1990). However, Baquerizo et al. (2001) added a fourth region to the nearshore and found both the seaward and shoreward shear can both be important to the growth of instabilities, similar to results in the bounded tidal inlet.
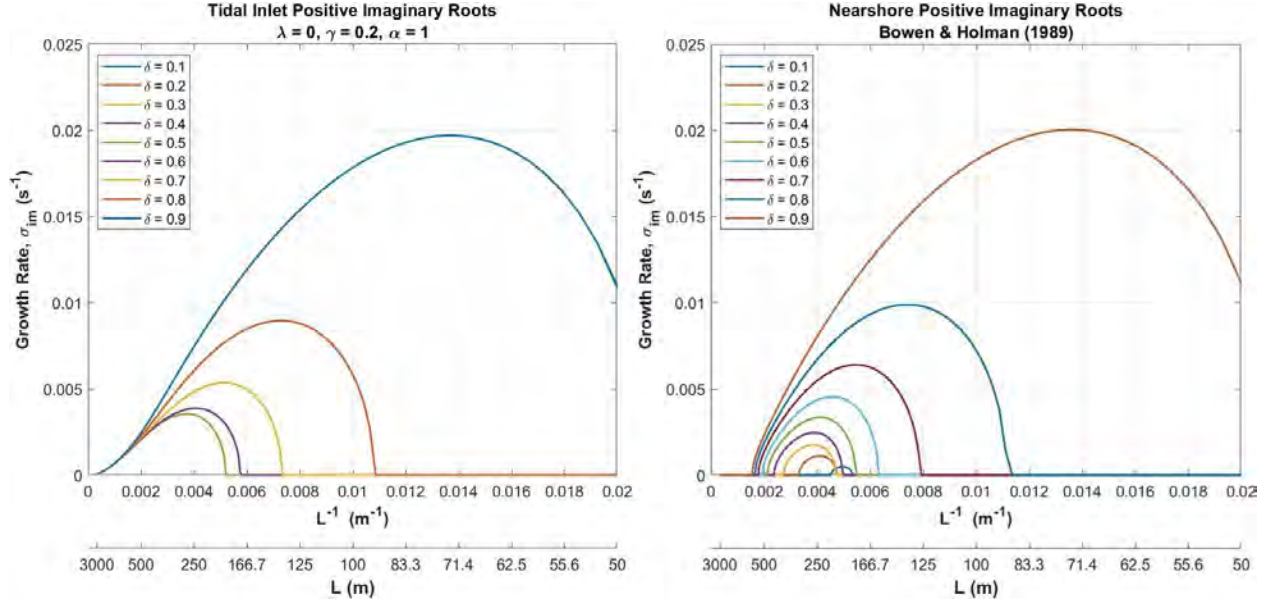
Figure 2.3. The growth rates (y-axis), inverse wavelengths (top x-axis) and corresponding wavelengths (bottom x-axis) of unstable modes in the bounded tidal inlet (left plot) and nearshore (right plot) for a variety of shear profiles (δ). The maximum velocity (V_m) was set to 1 m/s, current width was set to 100 m, the bathymetry is flat, and the flow is inviscid for each. The shelf widths for Region 0 and 3 were set to 0.2 for the bounded tidal inlet. Note, the frequency solutions are symmetric in the tidal inlet, e.g. δ=0.1=0.9 (blue line), δ=0.2=0.8 (orange line), and so on.

2.4.2 Bounded Tidal Flow Solution

The FGM of instabilities of bounded tidal currents are solved over a range of wavelengths (100 – 3000 m) while setting typical values for the maximum current speed, V_m, to 1 m/s, and width of tidal current, x_0, to 100 m. Several runs were completed allowing changes in one variable at a time, i.e. shear ($\delta = 0.1 – 0.9$), shelf widths ($\gamma_1 = \gamma_2 = 0.1 – 1.0$), shelf depths ($\alpha_0 = \alpha_3 = 0.1 – 1.0$, while $\alpha_1 = \alpha_2 = 1$), and friction ($\lambda = 0 – 0.01$). While manipulating one variable, the default case for the remaining variables is chosen to be a symmetric shear profile (i.e. $\delta = 0.5$), shelf widths to be 20% of the current width ($\gamma_1 = \gamma_2 = 0.2$), flat bathymetry ($\alpha_0 = \alpha_1 = \alpha_2 = \alpha_3 = 1.0$), and no friction ($\lambda = 0$).

21

For bounded tidal currents with inviscid flow, the characteristic FGM wavelengths are $O(10^2$ m), periods are $O(10^2 - 10^3$ s), and growth rates are $O(10^{-3} - 10^{-2}$ s^{-1}), with phase speeds approximately one third of the maximum velocity. In the presence of friction, the growth rates are slower and the range of unstable wavenumbers is reduced (Figure 2.4). The FGM occur when the shear is strongest (i.e. $\delta = 0.1$ or 0.9) regardless of what side of the channel it is on (i.e. in Region 1 where $\delta < 0.5$ or Region 2 where $\delta > 0.5$), the shelf widths are large (i.e. $\gamma_1 = \gamma_2 > 0.5$), the bathymetry is flat across the inlet (i.e. $\alpha_0 = \alpha_1 = \alpha_2 = \alpha_3 = 1.0$), and there is no bottom friction ($\lambda = 0$; Figure 2.5). Faster growth rates are typically associated with larger wavenumbers (smaller wavelengths; Figure 2.5). For the case of increasing friction, the wavenumber associated with the fastest growing mode (which reduces with increasing friction) remains the same and the range of wavenumbers with unstable modes decreases (Figure 2.4 - Figure 2.6). Friction acts to suppress the current magnitude, current shear, and the resulting instabilities uniformly across all unstable modes (as in Dodd et al., 1992) leading to a smaller range of unstable wavenumber modes and a slower growth rate (Figure 2.4 and Figure 2.6). For any given shear and shelf width, the growth rates are slowed and the wavelengths are not modified in the presence of increasing friction (Figure 2.6).
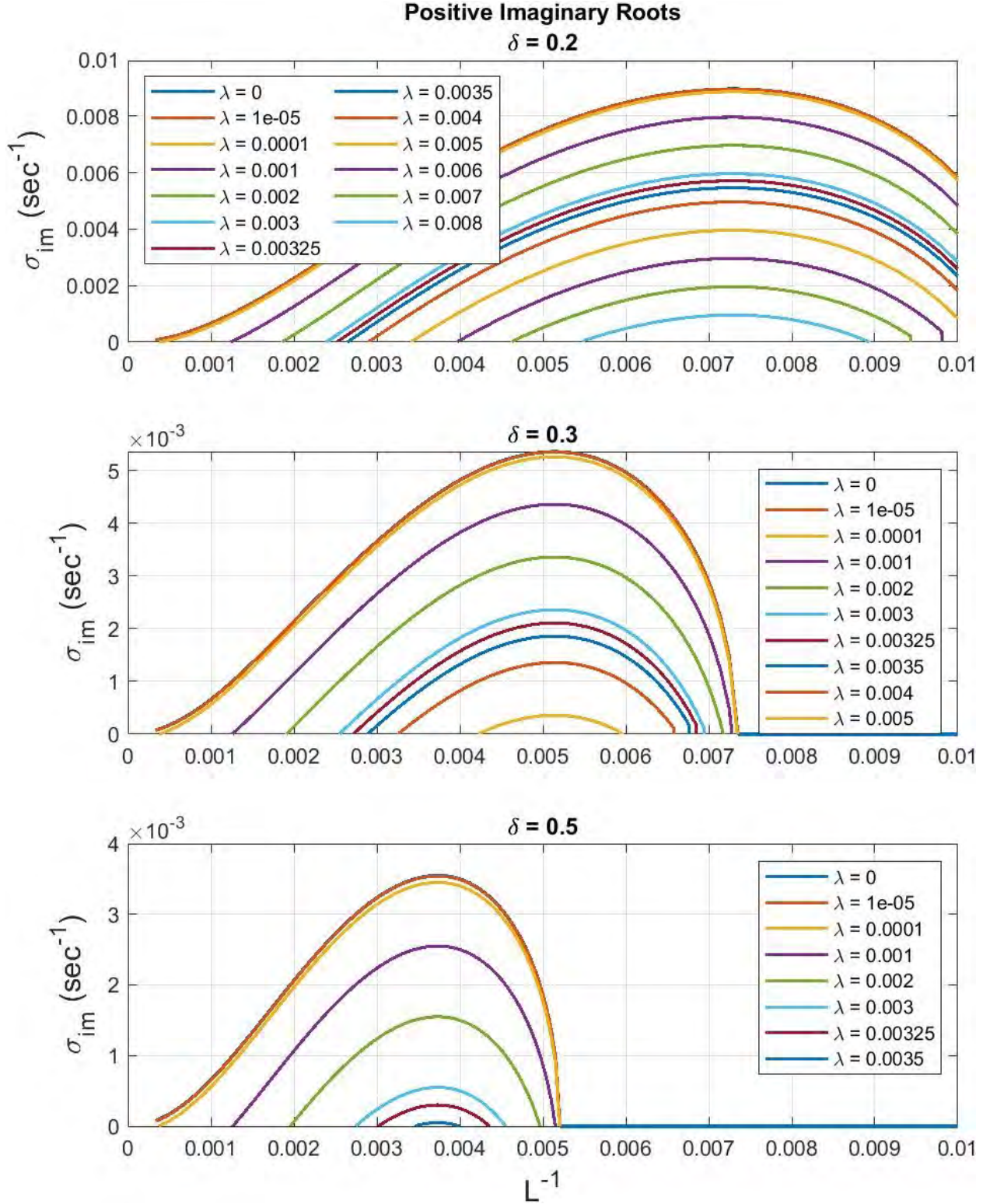
Figure 2.4. The positive imaginary roots to the tertiary dispersion equation with increasing friction (λ) for three different shear (δ) cases (strong, top panel; medium, middle panel; symmetric current and low, bottom panel). Note the change in scale of σ_{im} in each panel.
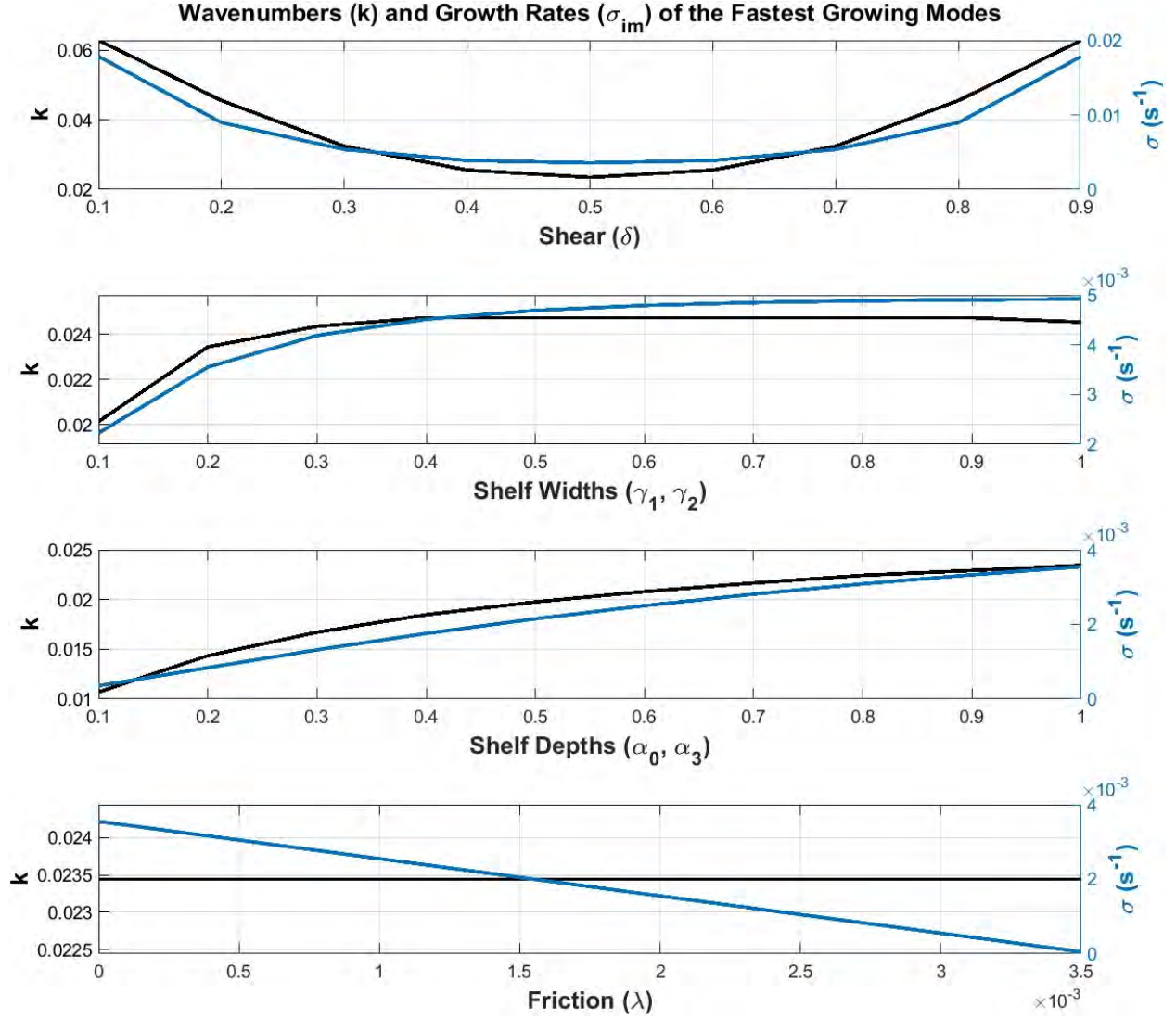
Figure 2.5. The fastest growing mode positive imaginary radian frequency (right y-axis; blue) and associated wavenumber (left y-axis; black) under changes in shear (top panel), shelf widths (second panel), shelf depths (third panel), and friction (bottom panel) given all other variables are set to the default case.

When the bathymetry tends towards a flat bottom, the growth rates are fastest and the wavelengths become smaller (Figure 2.7). In other words, as the shelf depths on either side of the main channel shoal, the growth rates of the shear instabilities are slower and wavelengths associated with the fastest growing mode are longer (Figure 2.5 and Figure 2.7). For a symmetric shear profile, $\delta = 0.5$, when Region 0 depth is set to be shallower than Region 3 depth (e.g. $\gamma_1 =$

$0.3, \gamma_2 = 0.7$) with the deeper channel in Region 1 and 2, the results are equivalent to a shallower shelf in Region 3 and slightly deeper shelf in Region 0 (i.e. $\gamma_1 = 0.7, \gamma_2 = 0.3$). This aligns with the frequency results being symmetric with changes in shear structure over a flat bottom. For a stair-step bathymetry, i.e. Region 0 is the shallowest moving down to Region 3 being the deepest, the fastest growing mode is slower than the flat bottom case and faster than having shallow shelves ($\gamma_1 = \gamma_2 \leq 0.7$) on either side of the channel.
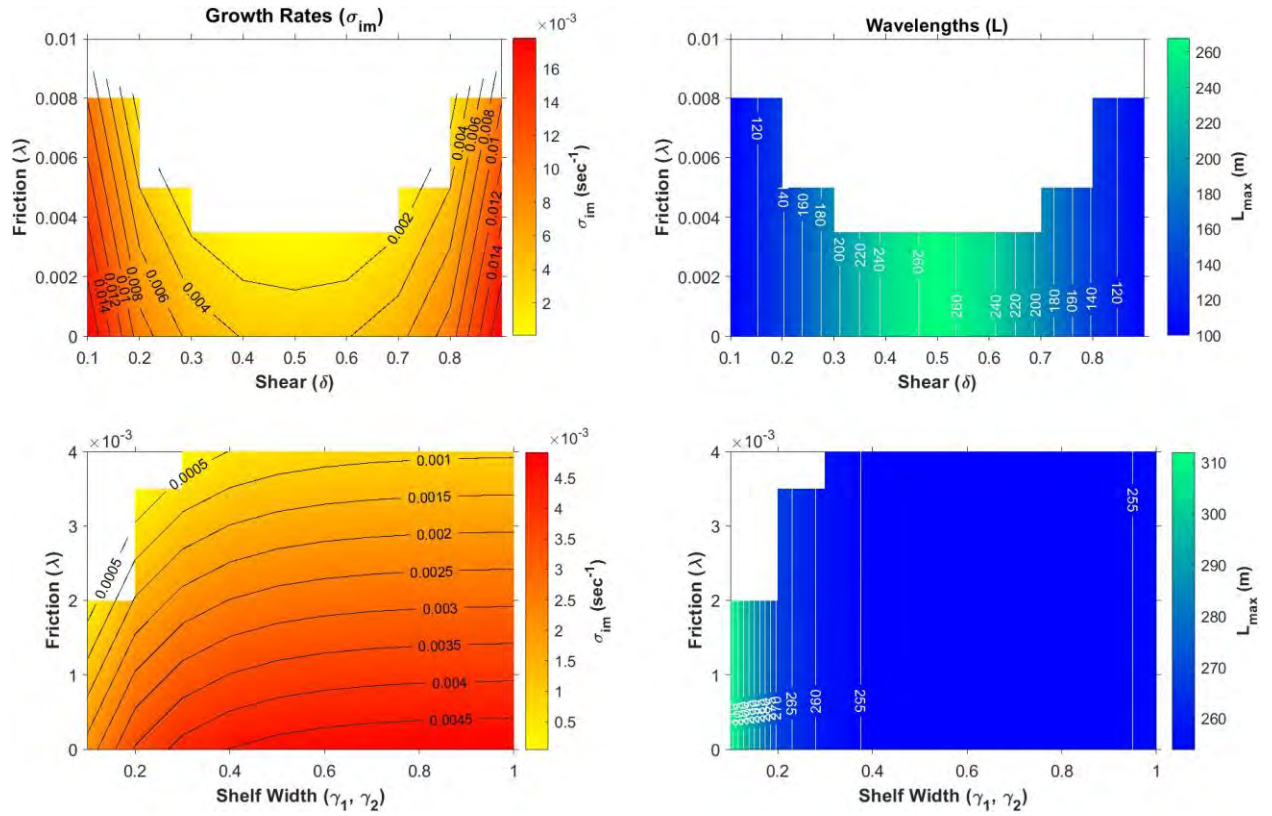
Figure 2.6. The growth rates (left column) and wavelengths (right column) of the fastest growing modes under varying friction (y-axis) with shear (top row) and shelf width (bottom row).
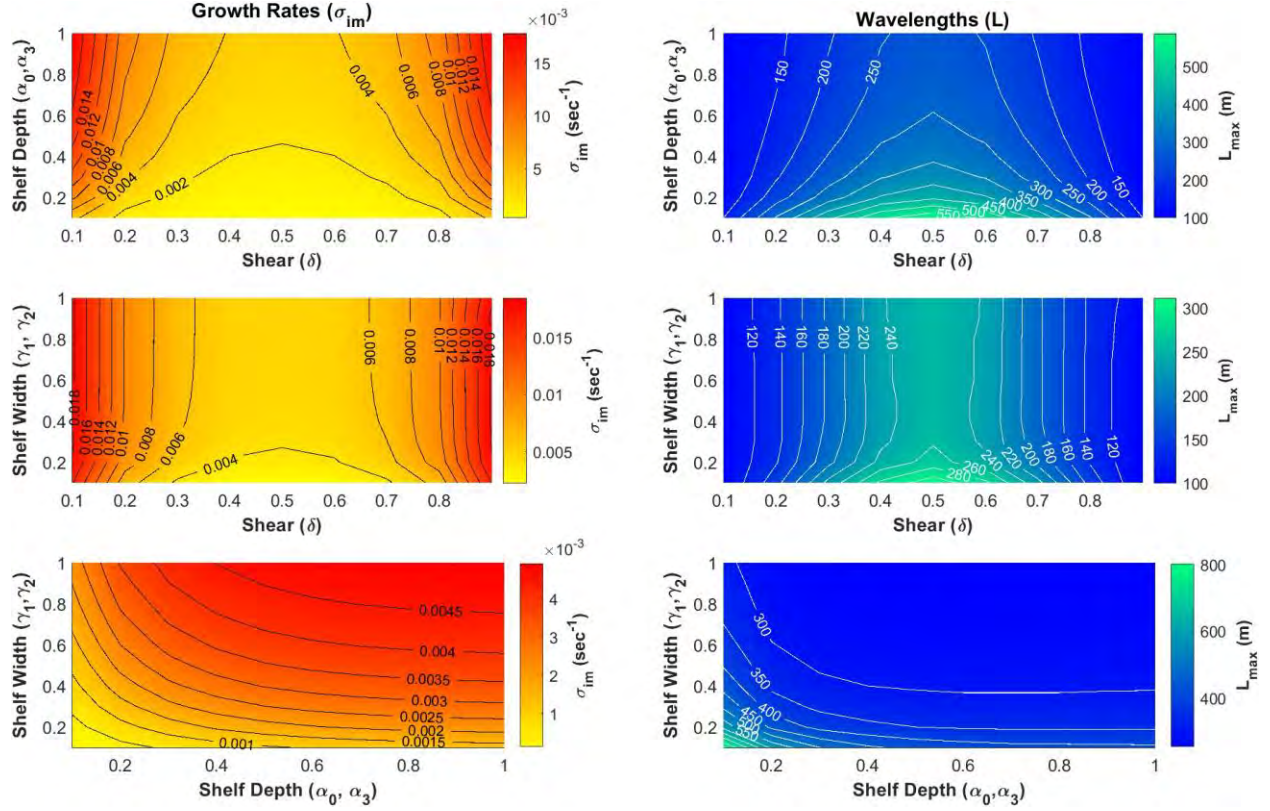
Figure 2.7. The growth rates (left column) and wavelengths (right column) of the fastest growing modes under varying shelf depth with shear (top row), shelf width with shear (middle row) and shelf width with shelf depth (bottom row). All cases are run with no friction (i.e. $\lambda = 0$).

For a given cross-inlet current profile, bathymetry, and shelf width, the stream function and resulting total velocity pattern of the fastest growing shear wave mode is found (Figure 2.8). The stream function shows the progressive nature of the shear instability moving along the channel and the velocity vectors show the meandering of the mean tidal current due to the instabilities.
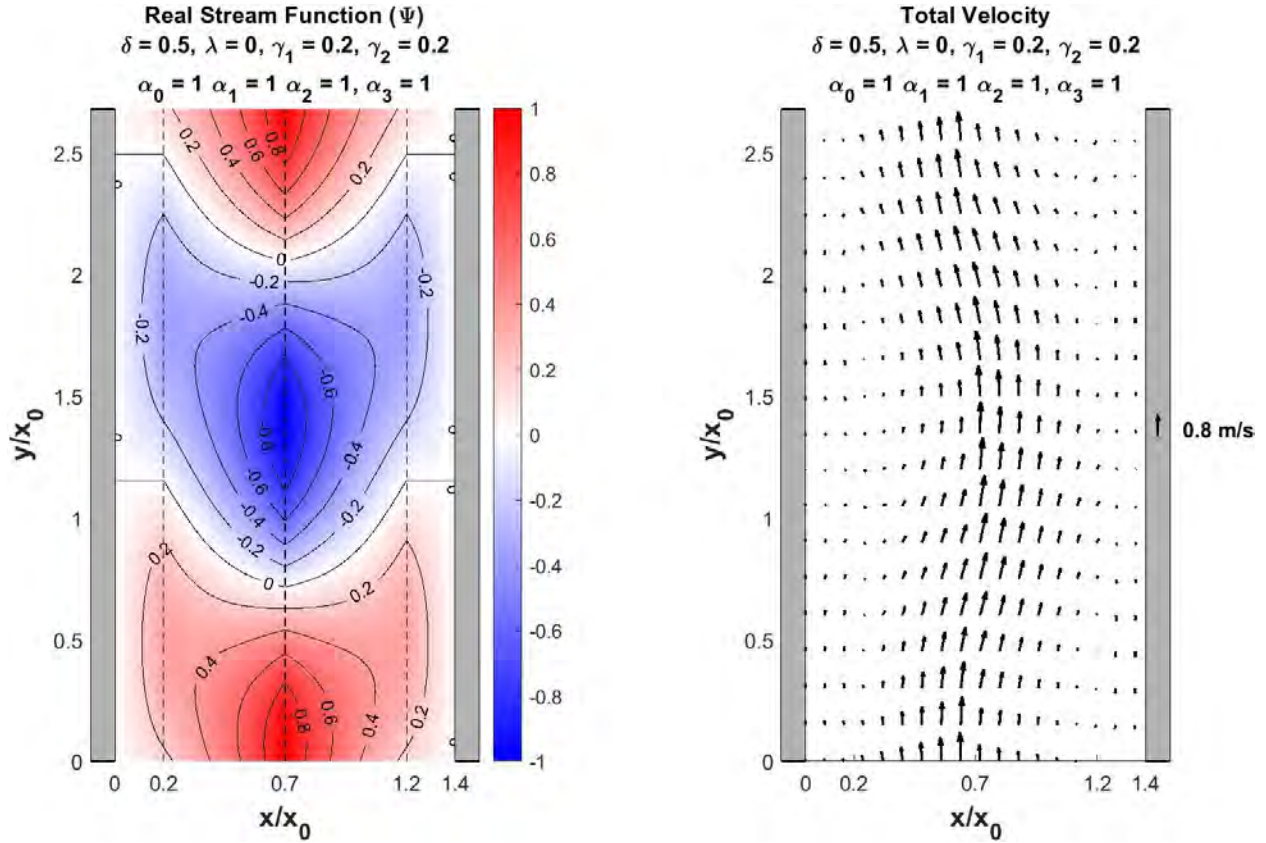
Figure 2.8. The real component of the stream function (left) and the total velocity (right) along the bounded tidal inlet normalized by the maximum velocity (V_m). The shear is set to be symmetrical ($\delta = 0.5$), the shelf widths in Regions 0 and 3 are set to 20% of the width of the tidal current (100 m), topographic shelves (50% total depth) are in regions 0 and 3, and the flow is inviscid ($\lambda = 0$).

Following Bowen and Holman (1989), the velocity phase differences, θ_{uv}, are plotted as a function of the cross-inlet distance indicating possible horizontal mixing in regions that have a phase change (Figure 2.9). When the velocity components are in quadrature (i.e. 90° apart), no mixing occurs (as in Regions 0 and 3) and when the phase gets closer to zero (Regions 1 and 2), stronger mixing is expected. This is supported with the calculation of the mixing magnitude through the cross-channel Reynolds shear stress, S_{yx}, (Figure 2.10). The mixing magnitude increases in areas of strong shear, which aligns with the velocity phase differences nearing zero (Figure 2.10). The mixing, S_{yx}, is always zero in Regions 0 and 3 where the perturbation velocities

27

are in quadrature (Figure 2.10). Stronger shear, wider shelf widths, and deeper shelves (nearing a flat bottom) lead to the strongest mixing while weak to no mixing occurs in regions with shallow, narrow shelves and weak shear. The mixing magnitude was calculated using the initial perturbation velocities. When the cross-channel velocity structure is asymmetrical ($\delta < 5$ or $\delta > 5$), the mixing magnitude is stronger in the region with higher shear. The Reynolds shear stress is the same magnitude whether the asymmetry occurs on one side of the channel or the other (e.g. $\delta = 8$ or $\delta = 2$), however the sign of the stress is opposite due to the sign of the gradient in the mean velocity profile between Region 1 and Region 2.
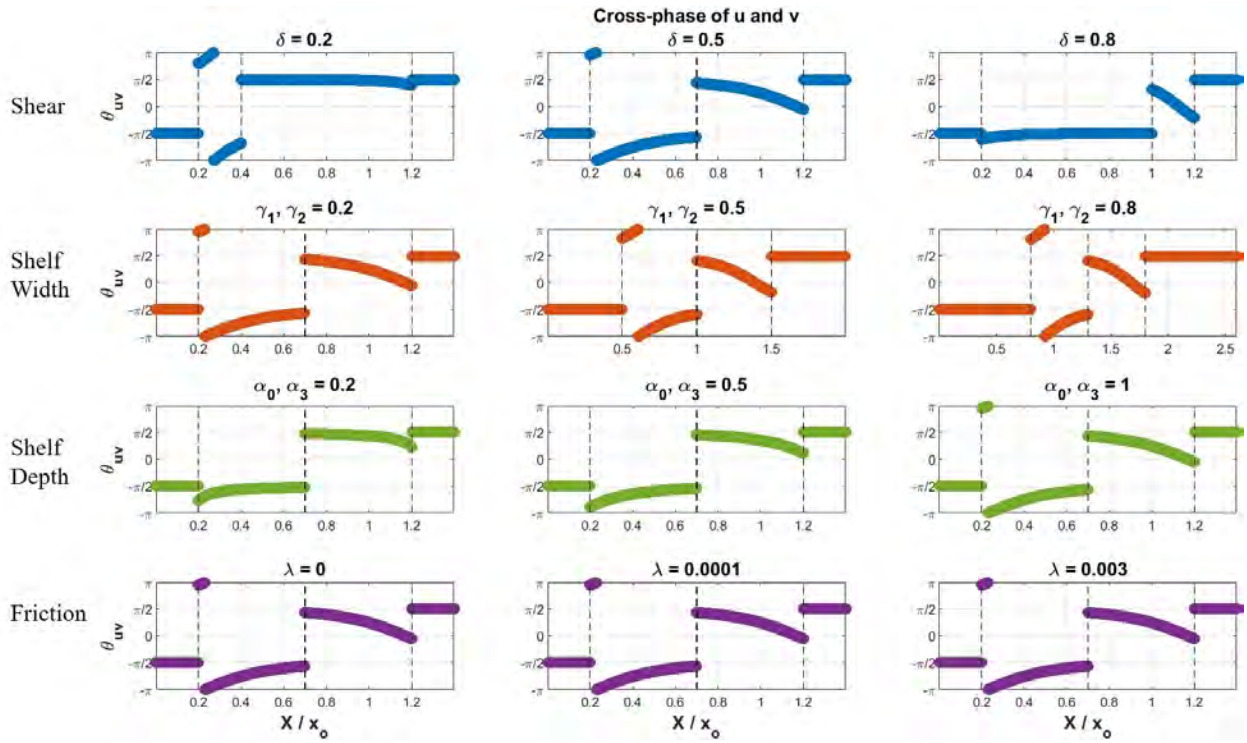
Figure 2.9. The cross-phase of the velocities, u and v, for various shear cases (first row), shelf widths (second row), shelf depths (third row), and friction (bottom row) with all other variables set to the default case.
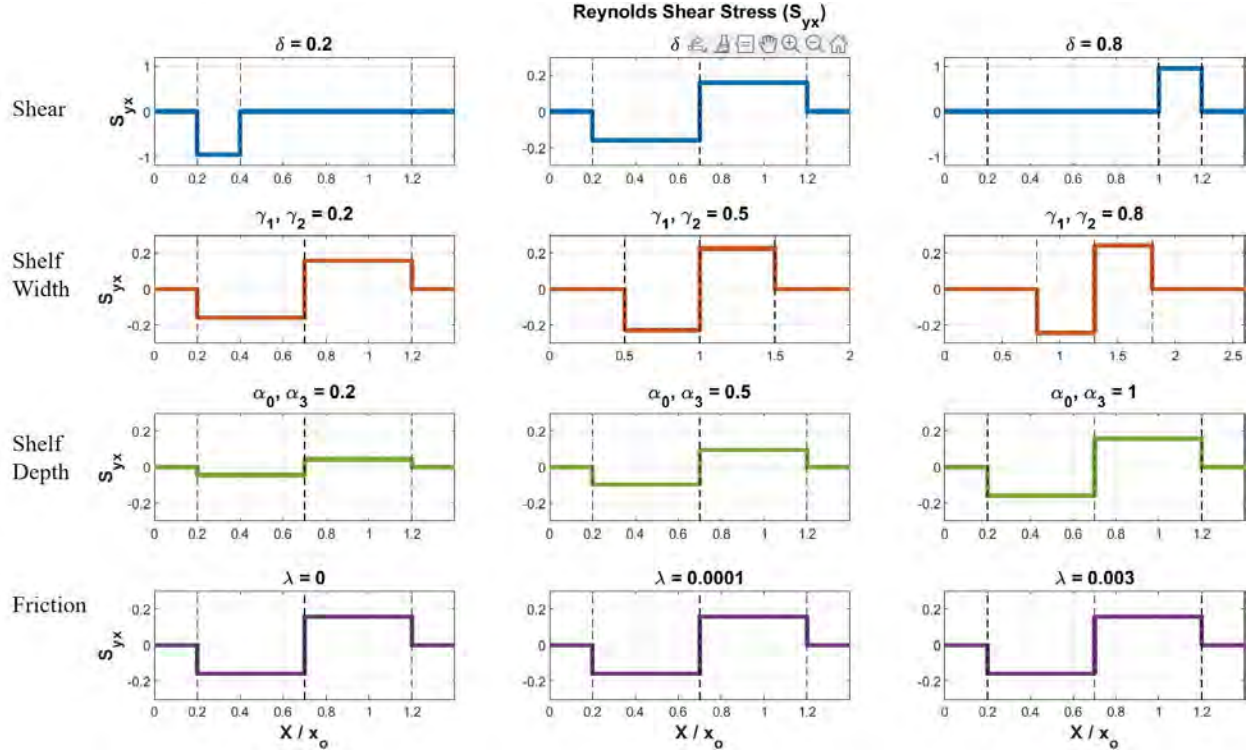
Figure 2.10. The Reynolds shear stress (S_{yx}) for various shear cases (first row), shelf widths (second row), shelf depths (third row) and friction (bottom row) with all other variables set to the default case inlet normalized by the maximum velocity (V_m). Note, the y-axis scaling is different in the first row, first column ($\delta = 0.2$) and in the first row, last column ($\delta = 0.8$) due to the large magnitudes.

2.5   Discussion

This theoretical analysis of unstable tidal currents flowing through a bounded channel is general, and under different parameter choices will reproduce the results for instabilities of longshore currents in the surf zone (such as Bowen and Holman, 1989; Baquerizo et al., 2001). The analytical instability analysis differs here from prior work in the boundary conditions and that forcing of the currents is from tidal pressure gradients and not incident gravity waves. Specifically, this analytical work deviates from Niiler and Mysak (1971), Bowen and Holman (1989), Baquerizo et al. (2001), and Mied et al. (2006) in that: (1) the flow here is bounded by land on either side of the channel versus having an infinitely extending seaward boundary, (2) the depth is variable across

all regions, (3) the widths of the cross-channel regions are variable, and (4) linear bottom friction is included. Similar to Niiler and Mysak (1971) and Baquerizo et al. (2001), an additional region in the cross-channel direction (Region 0, Figure 2.2) here leads to two extremums in the background potential vorticity, which is a necessary condition for unstable flow. This additional extremum allows shear instabilities to occur on either side of the maximum current unlike the analysis by Bowen and Holman (1989), which only allows for instabilities supported by the seaward shear of the current.

The characteristic wavelengths $O(10^2$ m), periods $O(10^2$ - 10^3 s), growth rates $O(10^{-3}$ - 10^{-2} s^{-1}), and phase speeds ($\sim V_m/3$) of instabilities of bounded tidal currents are of the same order of magnitude as the analytical solutions found in the nearshore (Bowen and Holman, 1989; Dodd and Thornton, 1990; Dodd et al., 1992; Özkan-Haller and Kirby, 1999; Dodd et al., 2000; Baquerizo et al., 2001). These motions are non-dispersive as seen by the nearly linear dispersion relationship between the real radian frequency and the wavenumber. The analytical unstable e-folding time scale, $1/\sigma_{im}$, associated with the growth rates of the fastest growing modes is approx. 2 – 5 min, which defines the time scale at which the exponentially growing motions increase by a factor of e ($\sim$2.7). This e-folding time scale is less than 1% of the half period of the dominant M_2 tidal constituent (6.21 hour) supporting the assumption of steady flow as discussed and found by Mied et al. (2006). Consistent with prior nearshore findings (Bowen and Holman, 1989; Dodd et al., 1992; Putrevu and Svendsen, 1992; Özkan-Haller and Kirby, 1999), areas of strong lateral shear lead to faster growth rates of instabilities of bounded tidal currents and a larger range of unstable wavenumber modes. Overall, shear is the dominant factor affecting the fastest growing mode followed by friction, bathymetry, and finally shelf width as seen by the changes in radian frequency magnitude in Figure 2.5 - Figure 2.7.

Consistent with prior findings (Dodd et al., 1992; Özkan-Haller and Kirby, 1999), friction acts directly to linearly damp the imaginary frequency of the fastest growing mode and limit the range of unstable wavenumbers (Figure 2.4 and Figure 2.5). The influence of friction on the radian frequency is seen mathematically by rearranging the first term in Equation 2.9, $\left(V + \frac{1}{k}\left(\sigma - \frac{i\lambda}{h}\right)\right)$. Thus, for growth of the instability, $\sigma_{im} > \frac{i\lambda}{h}$.

Once the shelf width reaches approximately half of the mean current ($\gamma_1 = \gamma_2 \approx 0.5$), the change in growth rates and wavenumbers plateau indicating any additional increases in shelf widths will no longer have a significant impact on the instability growth rates and associated wavenumbers (Figure 2.5). If the shelf widths continue to extend beyond $\gamma_1 = \gamma_2 \geq \pi$, it is essentially mimicking an open seaward boundary on either side of the channel due to the hyperbolic tangent converging to one. As a consequence, instabilities of flow through wide estuaries are not strongly impacted by the lateral boundaries and act similarly to unbounded solutions.

The spin up time to reach finite amplitude is characterized by the growth rate of the FGM and given by $1/\sigma_{im}$. Dodd et al. (1992) found this to be approximately $300 - 400$ s or in other words $1 - 2.5$ wavelengths distance, consistent with the characteristic e-folding scales of 300 s or roughly half the wave period found by Bowen and Holman (1989). The spin up time for bounded tidal currents varies depending on the inlet geometry and friction, however for the symmetric case (i.e. inviscid flow, flat bottom, symmetric shear ($\delta = 0.5$), narrow shelf widths ($\gamma_1 = \gamma_2 = 0.2$) the spin up is roughly 280 s or roughly a quarter of the period and approximately one wavelength distance, similar to the nearshore results. Both Dodd et al. (1992) and Bowen and Holman (1989) mention how this significant spin up time relative to the period indicates that the small amplitude assumption that supports linearity will likely be quickly violated. Thus, numerical models are

needed to simulate and analyze the instability motions as they reach finite amplitude in order to account for the nonlinearities.

For an instability to grow in time, the perturbed flow must gain energy in time, which requires a transfer of energy from the mean flow to the perturbed flow through the Reynolds stresses (Dodd and Thornton, 1990). Therefore, another condition for the presence of instabilities to develop is for the Reynolds stress to be negatively correlated with the current shear leading to a nonzero cross-shore gradient in the horizontal Reynolds stress (Dodd and Thornton, 1990; Dodd et al., 2000). For the bounded tidal inlet problem, this occurs over the region covered by the mean flow (i.e. in Regions 1 and 2) indicating horizontal mixing and a transfer of energy across the channel, resulting in a modified cross-channel structure of the mean velocity profile and implications on fate and transport of organic and inorganic substances. In the exterior Regions (0 and 3), the Reynolds stress is always zero since the cross-phase of the perturbation velocities are always in quadrature. This is consistent with results from Dodd and Thornton (1990) and Özkan-Haller and Kirby (1999) who attributed the Reynolds stress equaling zero to the periodicity in the longshore direction.

Instabilities of the mean flow have long been thought to provide an efficient mechanism for mixing momentum across the shore or channel (Bowen and Holman, 1989), and several nearshore studies found that mixing magnitudes are indeed large in the presence of instabilities (Dodd and Thornton, 1990; Church et al., 1992; Putrevu and Svendsen, 1992), consistent with the analytical results shown here. Furthermore, studies have found that mixing due to instabilities can be even stronger than other mechanisms of mixing such as turbulence or mixing due to eddy viscosity terms (Özkan-Haller and Kirby, 1999). Interestingly, Özkan-Haller and Kirby (1999) noted that the cross-shore location of the maximum velocity did not change as a result of the

presence of instabilities and the resulting momentum mixing. This suggests that the mixing of momentum across the channel in opposite directions in Regions 1 and 2 leads to a smoothed velocity profile; the mixing is balanced either by a restoring force or is equally opposite in Regions 1 and 2 in order for the location of the peak velocity to remain the same. When the shear is symmetric ($\delta = 0.5$) the mixing in Regions 1 and 2 is of equal magnitude and working in opposite direction balancing the forcing and smoothing the velocity profile. However, when the shear is not symmetric (e.g. $\delta = 0.2$), the mixing magnitude is stronger on one side of the maximum velocity (V_m) and moving the peak velocity location towards the boundary with higher current shear. Strong mixing in the region with strong shear (i.e. Region 1) would need to be balanced by the potential vorticity, $\frac{V_x}{h}$, restoring force. As the location of the peak velocity is forced towards the shoal due to mixing and leads to stronger shear, potential vorticity acts to force the peak velocity back counteracting the mixing. The potential vorticity profile is inversely proportional to the Reynolds shear stress and the two forces balance one another to conserve potential vorticity.

This analytical analysis does not include an eddy viscosity term in the momentum equations (1), however Özkan-Haller and Kirby (1999) found the eddy viscosity term to be much smaller than mixing caused by the Reynolds shear stress. Based on Özkan-Haller and Kirby (1999), it is expected that the inclusion of eddy viscosity would dampen high-frequency oscillations as well as the growth rate of the FGM leading to less energetic motions further smoothing the initial cross-channel velocity structure. In nonlinear numerical models that include eddy viscosity, it is found that the width of the current increases in the presence of instabilities (Dodd et al., 2000). This suggests that the inclusion of eddy viscosity and nonlinearities would further modify the cross-inlet velocity structure, potentially allowing for mixing up onto the shelves in the lateral Regions.

2.6   Conclusions

A tertiary solution was analytically found for the frequencies and wavenumbers of linear shear instabilities of a steady tidal current flowing through a bounded channel that includes the presence or absence of lateral shelves with variable widths and depths.   The radian frequencies and wavenumbers associated with the fastest growing modes are a function of the maximum velocity, cross-inlet velocity structure, inlet geometry including the shelf width and depth, and friction: $\sigma = f(k, V_m, \delta , x_0, \lambda, h, \alpha_0, \alpha_1, \alpha_2, \alpha_3, \gamma_1, \gamma_2)$.   The solution is general in that the various parameters can be modified to simulate prior analytical work over simplified nearshore bathymetry.   The fastest growing shear instability modes have characteristic wavenumbers $O(10^2$ m), periods $O(10^2 - 10^3$ s), growth rates $O(10^{-3} - 10^{-2}$ s$^{-1})$, and phase speeds ($\sim V_m/3$), consistent with prior findings in the nearshore environment (Bowen and Holman, 1989; Dodd et al., 1992; Özkan-Haller and Kirby, 1999), perhaps not surprising considering the size of flow and current shear are very similar.   The instabilities are progressive and non-dispersive as seen by the nearly linear relationship between the real radian frequencies and wavenumbers. The fastest growth rates and largest range of unstable wavenumbers occur when the shear is strong, bathymetry is flat, shelves are wide, and flow is inviscid.   Strong shear is the dominant forcing for the instabilities, while friction acts to suppress the growth rates and limit the range of unstable wavenumber modes. As the growth rate increases as a result of varying the inlet geometry and/or the shear magnitude, the wavenumber associated with the fastest growing mode also increases (i.e. shorter wavelengths).

The strongest mixing represented by the cross-channel Reynolds shear stress occurs under the same conditions that support the fastest growth rates and largest range of unstable wavenumbers (i.e. strong shear, flat bathymetry, wide shelves, inviscid flow).   The mixing of momentum across the channel under non-zero Reynolds stress due to shear instabilities modifies

the cross-inlet velocity profile, supports a transfer of energy from the mean flow to the perturbed flow, and likely significantly impacts estuarine dynamics, including the fate and transport of organic and inorganic matter.

CHAPTER III

3 OBSERVATIONS OF INSTABILITIES OF TIDAL CURRENTS IN THE HAMPTON-SEABROOK INLET

3.1 Abstract

Strong cross-channel shear of tidal currents flowing through a bounded inlet can lead to instabilities in the flow, causing a meandering of the mean along-channel current and potentially the spinoff of large eddies. The resulting variability of the currents and vorticity may affect navigation, the transport of dissolved and particulate organic and inorganic matter, tidal energy resource assessments, and cause lateral mixing of momentum across the inlet. To estimate the wavenumbers of shear instabilities within the Hampton/Seabrook Inlet, NH, a spatially-lagged array spanning 389 m consisting of seven sensors measuring tri-directional currents and pressure were deployed along the ~3 m (NAVD88) depth contour for one week during the spring tide in May 2021. Using iterative maximum likelihood estimators, wavenumber-frequency spectra are estimated during 3-4 hour periods with approximately steady currents on both the flood and ebb tides. Dominant wavenumbers ($\pm$ 0.002 - 0.02 m^{-1}) of the low frequency motions (0.0006 - 0.01 s^{-1}) with corresponding wavelengths ($\pm$ 314.2 – 3141.6 m) and periods (628.3 – 10472 s) are resolved and consistent with motions determined from a barotropic linear stability analysis. The instabilities are directed into the inlet on flood tides and out of the inlet on the ebbs, consistent with the expected propagation of unstable modes. The normalized velocity-to-pressure variance ratio at each station shows that the infragravity band is dominated by rigid-lid-like motions ($R \gg 1$) during both the flood and ebb tide. The lack of breaking wave group modulations within the inlet

and the presence of the seaward propagating instabilities on the ebb flow indicate that the presence of the instabilities can be attributed to the shear of the tidal current.

3.2 Introduction

Simple barotropic linear stability analysis suggests that strong cross-channel shear of tidal currents flowing through a bounded inlet can lead to instabilities in the flow causing a horizontal meandering of the mean along-channel current and potentially the spinoff of large eddies (Chapter II). Unstable currents may be strong enough to affect small boat safety and navigation, and the transport of dissolved and particulate organic and inorganic matter, and cause lateral mixing of momentum across the inlet similar to other shallow environments such as the surf zone of natural beaches (Özkan-Haller and Kirby, 1999; Dodd et al., 2000). The presence of instabilities that result in strong variations in the mean flow over time scales of O(0.5 to 5 min) will affect tidal energy assessment initiatives as hydrokinetic energy depends on the velocities to the third power (Lalander et al., 2013; Gunawan et al., 2014, 2017).

The scales of motion in tidal inlets are similar to those observed in the nearshore with the mean velocity of order of magnitude, O, (1 m/s), width of the mean current of O(100 - 300 m), and a similar cross-channel horizontal velocity shear structure. The depths of O(0 – 10 m) are similar, however the bathymetric profiles differ in that the nearshore typically has a planar or barred profile while inlets typically have a centralized deep channel with shoals on either side of the flow. The forcing and boundary conditions differ between the tidal flow and the nearshore. The tidal current is bounded on either side of the channel with a pressure gradient driving the flow. The nearshore has an open seaward extending boundary with incident gravity waves driving a longshore current and wave breaking occurring in the surf zone. Given similar scales of motion with slightly varying

inlet geometry and boundary conditions, it is expected for the temporal and spatial scales of the unstable motions in the nearshore and inlet environments to be of the same order of magnitude.

The presence of shear instabilities in the nearshore was first observed by Oltman-Shay et al. (1989) in the 1986 SUPERDUCK field experiment conducted on a barred beach profile at Duck, NC. These low frequency (infragravity band, $0.001 < f < 0.01$ Hz) unstable motions had wavelengths too short to be low mode gravity waves (leaky and edge waves) and with negligible surface elevations consistent with the theoretical linear stability analysis of Bowen and Holman (1989). Nearshore shear instabilities are characterized by having alongshore wavelengths of $O(10^2$ m), periods of $O(10^2$ s), and phase speeds dependent on the magnitude of the mean current and of $O(0.5$ m/s) (Oltman-Shay et al., 1989). Oltman-Shay et al. (1989) observed the instabilities to be non-dispersive and progressive, propagating in the same direction as the mean longshore current. The shear instabilities are supported by the background potential vorticity field provided by the cross-shore shear of the longshore current (Bowen and Holman, 1989; Oltman-Shay et al., 1989; Özkan-Haller and Kirby, 1999).

Lagged arrays of current meters were used during SUPERDUCK to observe the wavenumber-frequency spectra using Iterative Maximum Likelihood Estimators (IMLEs). Similar methods were used previously (e.g., Huntley et al., 1981; Oltman-Shay and Guza, 1987; Howd et al., 1992; Noyes et al., 2002; and others) to investigate low frequency edge waves on both near-planar and barred beach profiles. IMLEs are necessary to estimate wavenumbers of low frequency waves since the total length of the array is less than the typical wavelengths of the long infragravity band wave motions (Huntley et al., 1981; Oltman-Shay and Guza, 1987; Oltman-Shay et al., 1989).

Strong tidal current shear of similar magnitude to surf zone longshore currents have been observed locally in Hampton/Seabrook Inlet using University of New Hampshire's (UNH) vessel mounted acoustic Doppler current profilers (ADCPs) along repeated cross-inlet transects (McKenna, 2013). The normalized total infragravity velocity to pressure variance ratio, R, (Lippmann et al., 1999) obtained with a fixed bottom-mounted ADCP by McKenna (2013) shows that the infragravity band is dominated by rigid-lid like motions (R >> 1) consistent with linear theory. Analytical linear stability analysis described in Chapter II predicts instability modes should occur given the cross-inlet structure of the mean along-inlet current and inlet geometry as in the Hampton-Seabrook Inlet.

In this paper, field observations obtained from a lagged seven-element along-inlet coherent array of tri-directional current meters and pressure sensors are used to estimate infragravity and wavenumber-frequency spectra on both flood and ebb tidal stages. If instabilities of the mean tidal flow are produced, it is expected that a linear dispersion of energy will be present in the wavenumber-frequency spectra and the direction of instability propagation will follow the mean current direction, consistent with linear stability theory. The results are compared to the predicted unstable wavenumbers and initial growth rates of the fastest growing modes produced in a theoretical linear instability analysis discussed in Chapter II.

3.3 Field Site and Environmental Conditions

The Hampton/Seabrook Inlet (HSI) is a shallow tidally dominated sandy inlet along the southern New Hampshire coastline within the Gulf of Maine. The inlet is oriented approximately WSW to ESE and is bounded by jetties to both the north and south with overtopping occurring on high tide over the southern jetty (Figure 3.1). There is little tidal dissipation along the relatively shallow (< 10 m), short (~1 km long), and narrow (~350 m between jetties) channel that connects the ocean

39

to Hampton Harbor and the surrounding salt marshes (Cook and Lippmann, 2017; Lippmann et al., 2021).

Figure 3.1. (Left) The Hampton/Seabrook Inlet (HSI) bathymetry data collected prior to the ADCP deployment and the depths relative to several datums are marked with the various white lines. The current meter array deployment stations (black dots with station labels 1-7) and ADCP tow transects (red lines with labels 1 – 4) are also shown. (Right) A Google Earth image of the inlet during low tide with the ADCP stations shown as white dots. The jetties on the north and south side of the inlet, the bridge, and rock between stations 5 and 6 are visible.

The semidiurnal tides have a mean tidal range of 2.6 m with monthly variation between 2 – 4 m that provides the main hydrodynamic forcing driving circulation throughout the estuary. There is very little freshwater flow from the Blackwater and Hampton Rivers, and the estuary is considered well-mixed with little stratification (Jones, 2000; Lippmann et al., 2021). Tidal currents are primarily ebb-dominated, except during neap tides (Lippmann et al., 2021; Figure 3.11). Although strong winds can alter the circulation, the residual subtidal flow is weak (Jones, 2000; Lippmann et al., 2013). Incident surface gravity waves attenuate near the mouth of HSI due to refraction and breaking, especially along the southern side of the inlet (Lippmann et al., 2021).

During the duration of the array deployment (05/25/2021 – 06/01/2021), tidal elevation data were obtained from the Northeastern Regional Association of Coastal Ocean Observing

Systems (NERACOOS) tide gauge located within Hampton Harbor (https://mariners.neracoos.org/platform/Hampton%20Harbor) and tide predictions from NOAA's Center for Operational Oceanographic Products and Services (CO-OPS) in Hampton Harbor (Station ID 8429489) (Figure 3.2 and Figure 3.3). Hourly wind data were obtained from the NWS/NDBC Coastal-Marine Automated (C-MAN) Station located at the Isle of Shoals Lighthouse, NH (NDBC Station ID IOSN3) (Figure 3.2 and Figure 3.3). The data were recorded by wind measuring equipment located at a height of 19.2 m above site station. The station is approximately 17 km NE of the inlet (Figure 3.2). Offshore incident waves were observed with a Datawell Directional Waverider buoy located on Jeffrey's Ledge (NDBC station ID: 44098) located roughly 53 km offshore (Figure 3.2). The deployment occurred over the spring tide (4 m tidal range, Figure 3.3) in order to capture the maximum current magnitudes (and have the largest cross-inlet shear). Winds were initially variable and then became strong (i.e. gusts reaching nearly 20 m/s) and sustained for two days out of the northeast before becoming light and variable again (Figure 3.3). The Nor'easter led to large offshore significant wave heights reaching nearly 4 m with periods 7 – 10 s propagating from approximately 90°T N (nearly aligned with the inlet orientation) as observed at the offshore Jeffrey's Ledge buoy (Figure 3.3). However, the incident gravity waves were strongly attenuated due to refraction and breaking near the inlet mouth and were significantly reduced along the array deployed within HSI. Specifically, station 2 in the inlet observed a maximum significant wave height of 0.54 m, roughly two orders of magnitude smaller compared to the offshore conditions reaching a maximum of 3.57 m (Figure 3.3). The smaller gravity waves measured along the array were tidally modulated with the larger (smaller) waves occurring on high (low) tide, respectively, and did not break along the array except at the two most seaward sensors at low tide.
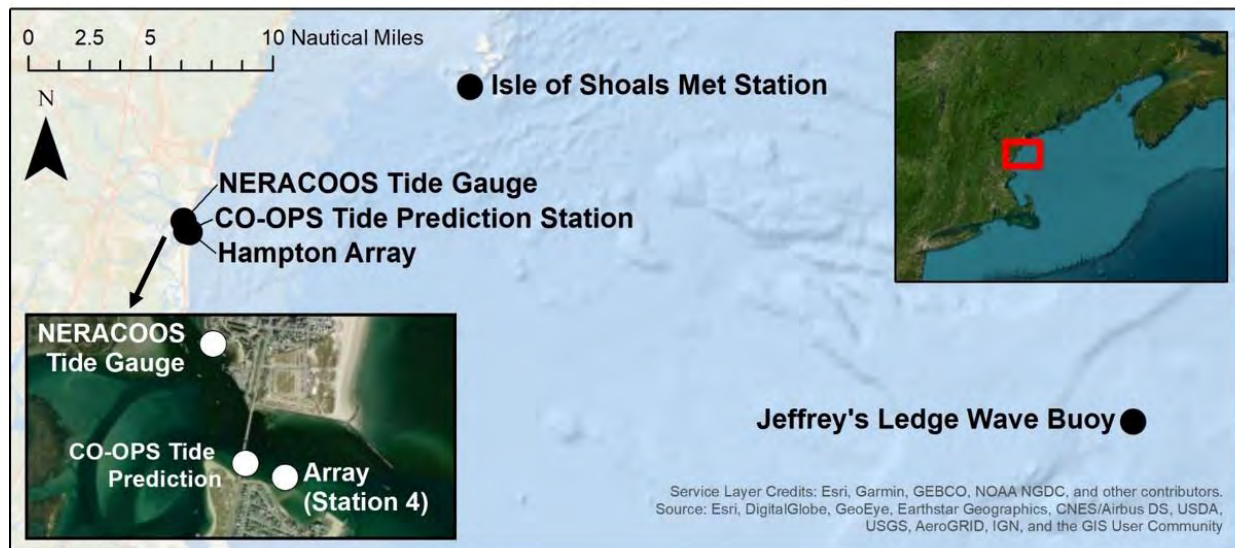
Figure 3.2. Station locations, including the ancillary data stations such as NDBC Jeffrey's Ledge Wave Buoy and the Isle of Shoals meteorological station. (Top right insert) The red box indicates the study location relative to the northeast U.S. coast and Gulf of Maine. (Bottom right insert) A zoomed in view of Hampton/Seabrook Inlet showing the NERACOOS tide gauge, CO-OPS tide prediction station, and general array location represented by station 4.

Sediment transport within the inlet and Hampton harbor has previously been found to be dominated by migrating sand waves within the inlet (McKenna, 2013). Interannual changes to the bathymetry can be large, but do not occur rapidly (von Krusenstiern, 2021). A bathymetric survey prior to the array deployment compared with a second survey after the recovery of sensors showed minimal change to the bathymetry along the contour where the current meters were deployed.
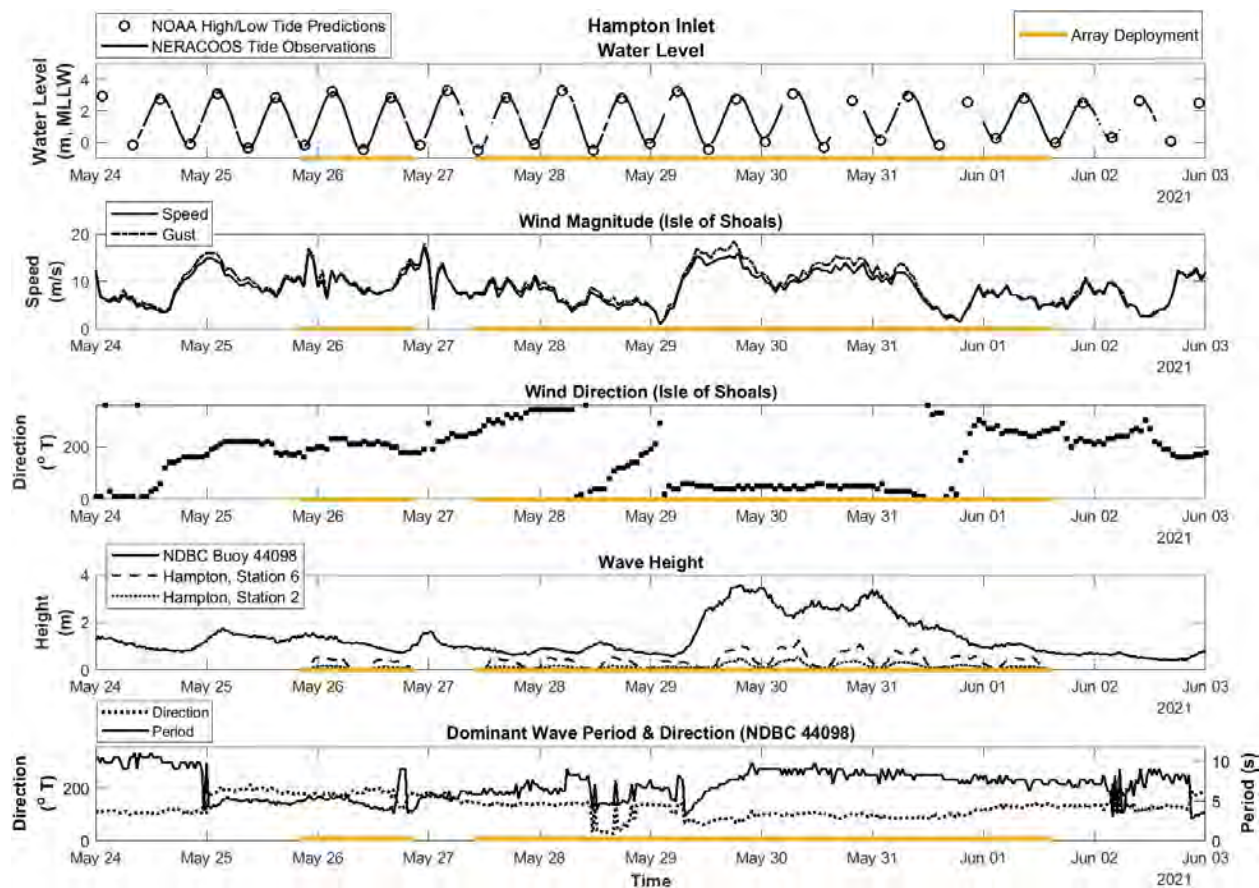
Figure 3.3. Ancillary data including (top) NOAA CO-OPS tide predictions and NERACOOS water level from the Hampton tide gauge, (second) Isle of Shoals wind magnitude, (third) Isle of Shoals wind direction, (fourth) NDBC Jeffrey's Ledge buoy significant wave height and significant wave height calculated from the array pressure sensors at station 6 and 2, (bottom) and NDBC Jeffrey's Ledge buoy dominant wave period and direction. The yellow bars indicate when the ADCP array was deployed.

3.4 Methods

3.4.1 Bathymetric Surveys

A multibeam bathymetric survey was completed on May 13 – 14, 2021, one week prior to the array deployment. A subaerial topographic survey was conducted during low tide on May 13 using a push-cart equipped with a differential GPS referenced to a stationary, local base station established adjacent to the inlet. During high tide on May 14, the multibeam survey was conducted using the

UNH Zego boat survey system, a maneuverable catamaran equipped with a 240 kHz multibeam echosounder (Imagenex Delta T) and a GPS aided Inertial Measurement Unit (Applanix POS MV 320) for highly accurate positions. The bathymetric data from the high tide survey and the topographic data from the low tide survey were merged and referenced to the NAVD88 datum (Figure 3.1). The bathymetric surveys were used to determine the exact placement of the current meter array alongside the channel. Following the recovery of the ADCP array, a second bathymetric survey was conducted on June 2, 2021 using the same systems and compared with the bathymetry data collected prior to the deployment to determine the (small) net change to the topography over the course of the experiment.

3.4.2 Cross-Inlet Current Surveys

Cross-inlet current surveys were conducted using the UNH Zego boat equipped with a downward-looking ADCP (Teledyne RDI Workhorse) with bottom tracking. The ADCP was calibrated prior to collecting velocity data, which was quality controlled to remove any erroneous spikes and depth averaged to further reduce the noise. Data was collected along four cross-inlet transect lines on May 28, 2021 to better understand the vertical variability and cross-channel velocity structure and shear during the array deployment (Figure 3.4 - Figure 3.6).
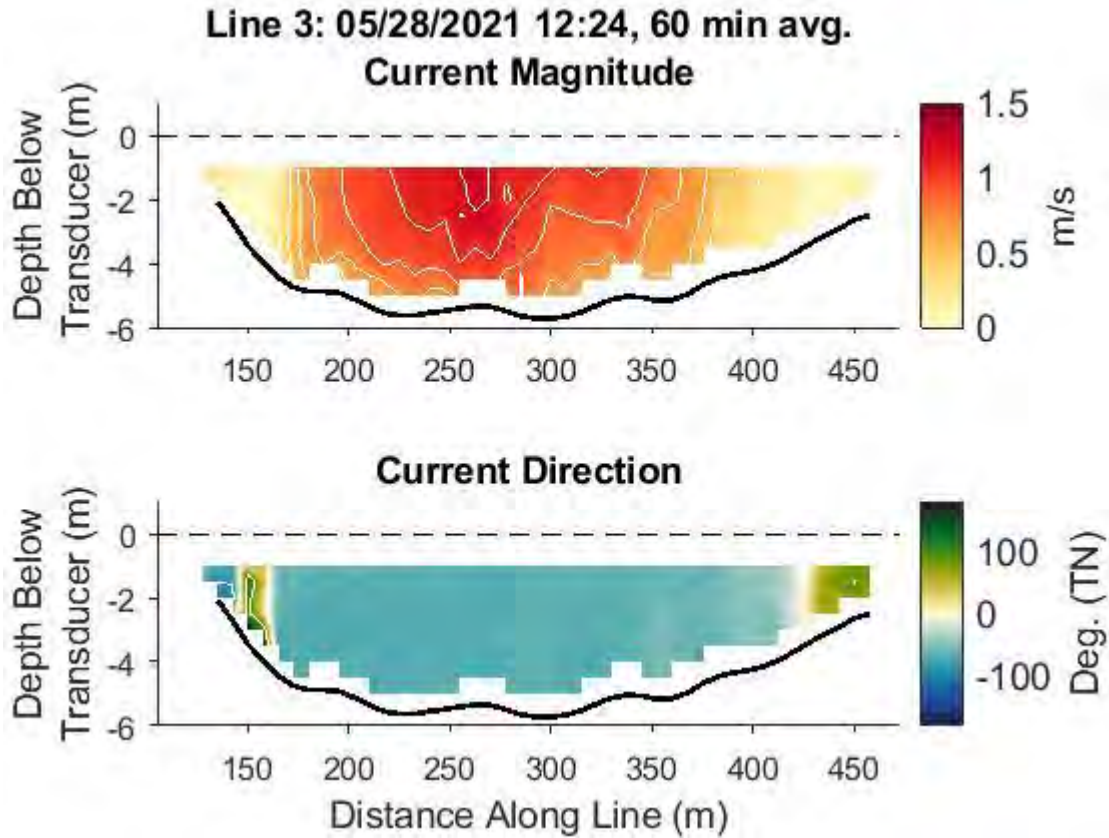
Figure 3.4. Current magnitude (top) and direction (bottom) observed across the third transect line (labeled in Figure 1) during a flooding tidal stage on May 28, 2021.
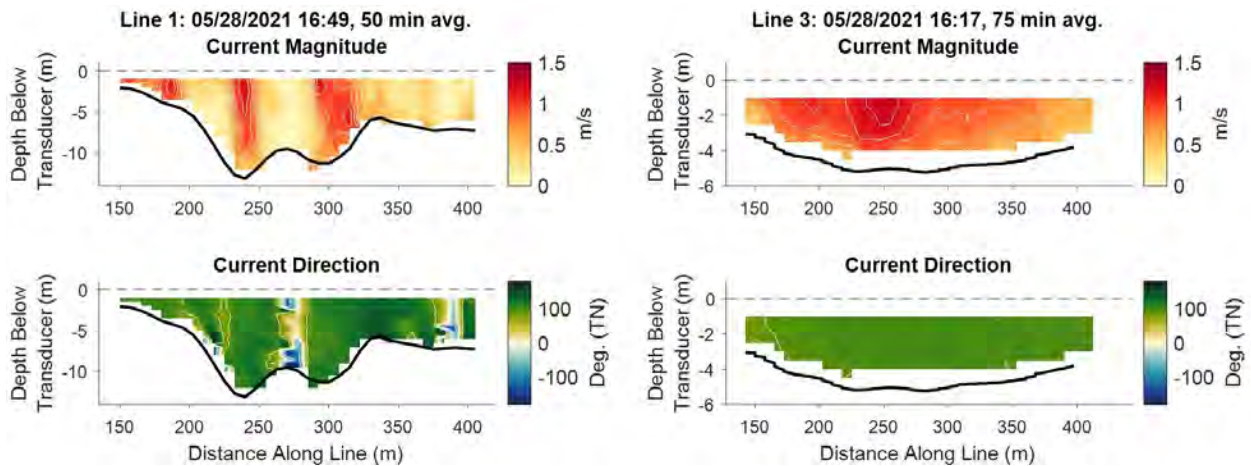
Figure 3.5. Current magnitude (top) and direction (bottom) observed across the first transect line (left) and third transect line (right) during an ebb tidal stage on May 28, 2021.
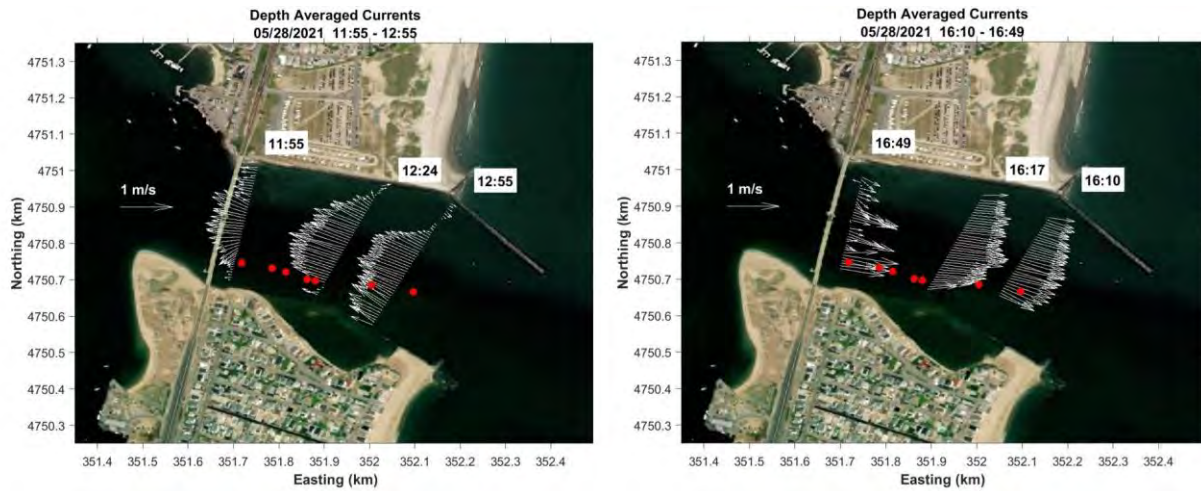
Figure 3.6. Depth averaged currents collected along three transect lines on May 28, 2021 using the UNH Zego Boat equipped with a bottom tracking ADCP. The red dots indicate the current meter array stations. Flood currents collected between 11:55 to 12:55 (left) and ebb currents collected between 16:10 to 16:49 (right).

3.4.3 Current Meter Array Deployment

In HSI, the currents are driven almost entirely by the mixed semidiurnal tides. Daily changes to the flow characteristics are small and we expect the behavior of the instabilities to occur on spring/neap tidal cycles. Therefore, in order to optimize the likelihood of observing strong instabilities, the currents were measured continuously over the spring tides when the tidal currents are strongest and the cross-inlet shear is maximum. The sensors were initially deployed on May 25, 2021, were briefly recovered on May 26 to check the configurations and data, and then re-deployed on May 27 before finally being recovered on June 1, 2021.

The unequally spaced lagged array of sensors were deployed on pipes jetted into the seabed on the south side of the inlet approximately along the 3 m depth contour as far into the channel as allowed to avoid interference with the navigational channel (Figure 3.1). The array was comprised of seven current meters, including acoustic Doppler current profilers (ADCPs), acoustic Doppler

velocimeters (ADVs), and modular acoustic velocity sensors (MAVS), that vary in frequency and vertical profiling range (Table 3.1); each was equipped with a pressure sensor.

Table 3.1. Sensors deployed in the array, station locations and sampling parameters. The sensor types include acoustic Doppler velocimeters (ADVs) and acoustic Doppler current profilers (ADCPs). The Nortek Aquapro at station 5 was configured to be in high-resolution (HR) mode. The station depth is relative to NAVD88.

Station	Sensor Type	Sensor Make/Model	Sensor Location	Station Depth (m)	Sampling Frequency (Hz)	Blanking Distance (m)	Bin Size (m)	Profiling Range (m)
1	ADV	Nortek Vector	42.89478, -70.81610	-2.805	1			
2	ADCP	Nortek Signature 1000 kHz (A)	42.89466, -70.81527	-2.917	1	0.2	0.25	7.5
3	ADCP	Nortek Signature 1000 kHz (B)	42.89457, -70.81490	-3.192	1	0.2	0.25	7.5
4	ADV	Sontek Argonaut	42.89440, -70.81432	-3.113	10			
5	ADCP (HR)	Nortek Aquapro 2000 kHz	42.89437, -70.81410	-3.060	1	0.096	0.03	0.84
6	ADV	Nobska MAVS-4	42.89428, -70.81257	-2.944	1			
7	ADV	Nobska MAVS-3	42.89412, -70.81144	-2.449	1			

The total length of the array (389.3 m) was chosen in an attempt to optimize the length of the array with minimum lag spacing of ~20 m and to fit within the inlet. The unequally spaced lagged array allows for more unique lags between sensors (or the sum of the sensor separations between all stations) leading to a higher resolution of the cross-spectra as a function of lag space (Davis and Regier, 1977). In comparison, having redundant lags in an equally spaced array leads to lower resolution spectra, however it also lowers the noise and uncertainty in the estimates due to multiple estimates for a given lag that can be averaged (Davis and Regier, 1977). The minimum lag spacing (dx) was 18.5 m, limiting the Nyquist wavenumber to $k = 0.027$ m^{-1}. These methods align with guidance from prior field studies of low frequency motions in the nearshore (Oltman-Shay et al., 1989).

The current meters are referred to by station number, 1 – 7, with the sensor furthest seaward to the east being station 7 (Figure 3.1; Table 3.1). The sensors were sampled at 1 Hz with the exception of the Sontek ADV (station 4), which pinged rapidly can only could be configured to record an average of samples once every 10 seconds. The Nortek Aquadopp Profiler (or AquaPro; station 5) was set to high-resolution mode with small bin sizes (0.03 m) profiling 0.84 m range with blanking distance of 0.096 m and the velocities were corrected for phase ambiguities. Both Nortek Signature ADCPs (stations 2 and 3) profiled 7.5 m range with 0.25 m size bins and blanking distance of 0.2 m. The sensors were placed in such a way as to measure the flow at a similar depth above the bottom. The profiling instruments were deployed near the seabed and the ADVs and MAVS as far down in the water column as possible.

Several sensor issues occurred. The MAVS-3 (station 7) did not record data prior to May 26, 2021. The battery in the Nortek Vector ADV (station 1) died the evening of May 28 and recorded only four (out of seven) days of data. Finally, in order to prevent the sensors from being buried in the sand, the Signature (station 2) and AquaPro (station 5) were slightly raised vertically on May 28 and 29th, respectively, with elevation changes noted. The MAVS-4 and MAVS-3 (station 6 and 7, respectively) were not included during the storm between May 26 17:00 and 29th 10:00 due to high frequency noise in the velocity data resulting from breaking waves causing vibrations of the sensors.

3.4.4 Data Analysis

Two assumptions of the flow are made: stationarity during the sampling period and homogeneity along the array (Huntley et al., 1981). Here, a "run" is defined as an analysis period that typically spans 3 – 4 hours during the flood or ebb tide when the mean flow magnitude is quasi-steady.

For each analysis run, data from all sensors included in the array were quality controlled in the same manner. This involves accounting for side-lobe interference from ADCP surface return signals (stations 2, 3, and 5) by discarding the top 6% of the vertical profile below the water level, which is determined from the angle of the beam relative to vertical. The pressure signal was adjusted to account for the sensor height above the seafloor, the ADCPs (stations 2, 3, and 5) were depth averaged to reduce the noise and align the bins with similar sampling depths of the ADVs and MAVS, and the 1 s data was averaged to 10 s to reduce the noise. Time series velocity data were then detrended by regressing against a quadratic to remove low frequency changes to the mean current due to the rising or falling tide similar to methods for analysis of surf zone instabilities (Oltman-Shay et al., 1989). Spurious data points greater than $\pm$ 3 standard deviations from the mean were removed. Magnetic declination was accounted for in all sensors to place the flows in geographical coordinates.

Due to various sensor issues (described in Section 3.4.3) and/or coherency concerns with the stations located closer to sea (stations 6 and 7), several analysis runs neglect stations 1, 6, and/or 7 limiting the total length of the array to as small as 100 m. Despite the shortening of the array, appropriate wavenumber analysis was adequately performed.

When calculating spectra, velocity data were windowed using a Hanning taper, which has smooth edges and good slide lobe suppression, and ensemble averaged using 8 ensembles with no overlap resulting in 16 degrees of freedom (DOF). The normalized total velocity to pressure variance ratio, $R = \dfrac{\frac{\langle u^2 \rangle + \langle v^2 \rangle}{\langle p^2 \rangle}}{\frac{g}{h}}$, defined by Lippmann et al. (1999) was then calculated for each run and over the full array deployment time period. R can be used to estimate the fraction of gravity waves versus velocity instabilities that make up the infragravity frequency band; when R >> 1, the

infragravity band is dominant with velocity fluctuations consistent with rigid-lid motions and when $R \leq 1$, gravity waves are present and dominate in the infragravity band. The fraction of instability variance, $\alpha = 1 - \frac{1}{R}$, as defined Lippmann et al. (1999) was also calculated for the entire deployment period using the mean R.

For a spatially lagged, linear array that is short relative to the wavelengths of interest, the iterative maximum likelihood estimator (IMLE) developed by Pawka (1982, 1983) can be used to estimate the wavenumber-frequency spectrum of the long wavelength, low frequency motions (Pawka, 1983; Oltman-Shay and Guza, 1984, 1987; Oltman-Shay et al., 1989; Howd et al., 1992). The IMLE depends on sensor lag spacing, wavenumbers, the inverse of the cross-spectral matrix, and tuning parameters that dictate the rate of convergence of the estimated to the true cross-spectral matrix (Pawka, 1983; Oltman-Shay and Guza, 1984). Following Oltman-Shay and Guza (1984), a Kaiser-Bessel cosine-taper data window with 50% overlap was applied prior to calculating the cross-spectral matrix and the IMLE beta and gamma parameters were set to 1 and 20, respectively. The sum of square error of the estimated cross-spectral matrix was not significantly minimized when increasing the number of iterations above 20. Since computational power was not a concern, 50 iterations were used (as in Oltman-Shay and Guza, 1984). For all calculations, the IMLE wavenumber bin width was set to 0.001 m^{-1}.

3.4.5 Comparison to Linear Instability Theory

Estimated wavenumber-frequency spectra are compared with the linear analytical solutions for the fastest growing unstable modes using the dispersion relationship found in Chapter II. The analytical cross-inlet geometry and velocity profile parameters were set to similar magnitudes observed in HSI. The inlet is split into four regions across the channel allowing for varying cross-inlet bathymetry, velocity, and shear structure (Figure 3.7).
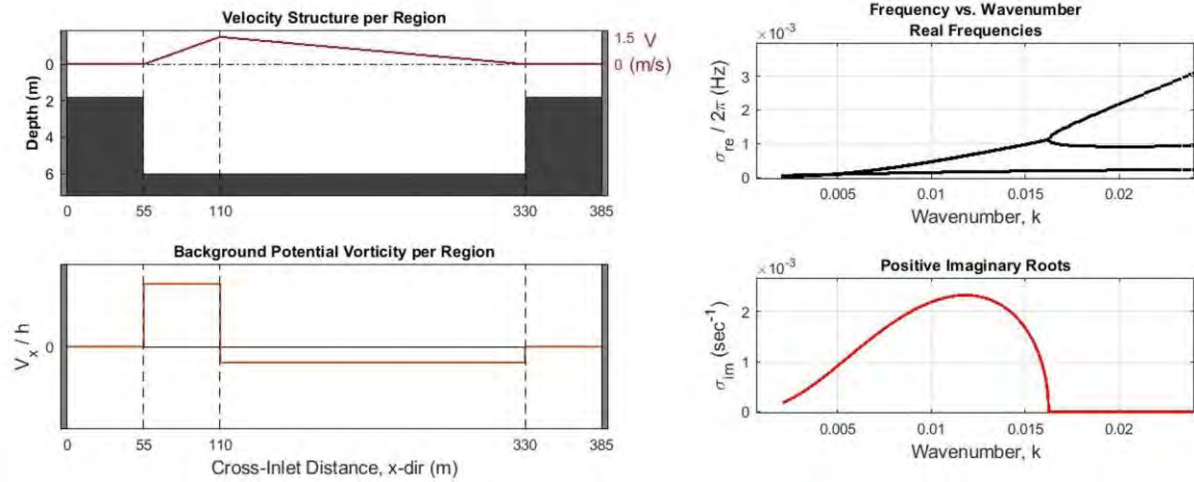
Figure 3.7. (Top left) Cross-inlet velocity structure and bathymetry broken down into four regions (denoted by black dotted lines) that depict HSI. (Bottom left) The background potential vorticity across the inlet. (Top right). The real frequencies and wavenumbers solved in the linear analytical cubic dispersion equation. (Bottom right). The positive imaginary frequencies and wavenumbers solved in the linear analytical cubic dispersion equation.

HSI geometry and velocity parameters are estimated based on the bathymetric and cross-inlet ADCP surveys (Figure 3.4 - Figure 3.6). The width of the non-zero current is 275 m and lateral shelves are 55 m wide (Figure 3.7). The total depth is 6 m in the channel in the interior regions and the lateral shelf depth is ~2 m representing the mid-tide range. The maximum current, V_m, is 1.5 m/s and occurs closer to the southern boundary allowing for an asymmetric shear structure (Figure 3.7). Although the friction coefficient was set to zero for simplicity, friction is expected to suppress the growth rates and reduce the range of wavelengths with unstable modes Chapter II. For a range of wavelengths (100 – 3000 m), the corresponding real and imaginary frequencies of the initial growth rates are solved using the cubic dispersion equation (Chapter II; Appendix C: Cubic Solution).

51

3.5 Results

Results from two runs each spanning 3 - 4 hours during the max ebb (Run 20) and max flood (Run 30) when the currents are considered quasi-steady are discussed here. Run 20 spans May 28, 2021 14:50 – 17:55 and includes stations 1 – 5 limiting the array length to 170.8 m with a minimum lag spacing of 18.5 m. Run 30 spans May 29, 2021 23:00 – May 30, 2021 02:45 and includes stations 2 – 5 limiting the total array length to 101 m with a minimum lag spacing of 18.5 m. The offshore incident gravity waves were small during Run 20 and large during Run 30 (Figure 3.3); however, wave breaking was confined to the outermost southern shore of the inlet and significantly attenuates prior to reaching the array.

3.5.1 Current Velocity

The UNH Zego boat cross-inlet ADCP transects were used to observe the vertical and horizontal spatial variability in the currents on May 28, 2021 flood and ebb tides. HSI is well mixed but there is a substantial mean flow bottom boundary layer owing to the rough bottom caused by mega-ripples and sand waves within the inlet (McKenna, 2013) and apparent in the cross-inlet mean flood current profile shown in Figure 3.4. On the ebb flows, the bridge piles interfere with the flow and create high frequency downstream eddies from vortex shedding. The disruption of the flow is strong near the bridge (Figure 3.5, left panels), but rapidly decays and by transect 3 (Figure 3.1) was not evident in the cross-inlet current profiles (Figure 3.5, right panels), consistent with similar observing by McKenna (2013). The direction of the flow throughout the array was nearly uniform over depth, and so the currents were depth integrated to observe the cross-inlet horizontal variability (Figure 3.6). On both the flood and ebb tidal stages, there is strong horizontal shear in the mean tidal currents (Figure 3.4 - Figure 3.6). The shear is strongest near the edges of the

channel where the bathymetry shoals along both the northern and southern boundaries of the inlet. The array was intentionally deployed in this area of strong shear on the southern side of the navigational channel approximately along the 3 m depth (relative to NAVD88) contour. The fastest velocities occur in the center of the channel where the depth is greatest (approx. 6 m relative to NAVD88). There is some recirculation of the flow along the northern side of the inlet, evident in Figure 3.4 and Figure 3.6, but not expected to influence the instabilities produced by the sheared tidal currents.

The quality controlled, quadratically detrended pressure and velocity from station 3 are shown for Run 20 on an ebb tidal stage in Figure 3.8 and for Run 30 on a flood tidal stage in Figure 3.9. The mean current magnitude across stations 1 – 5 in Run 20 is 0.767 m/s with a maximum current magnitude of 1.2 m/s and the mean across stations 2 – 5 in Run 30 is 0.226 m/s with the max speed reaching 0.7 m/s. The maximum current is ~1.5 m/s and occurs near the channel away from the array (Figure 3.4 - Figure 3.6). Oscillations on the order of several minutes in the velocity (u, v) are seen in both runs (Figure 3.8 and Figure 3.9), suggestive of the presence of current instabilities. It is worth noting that the runs occur at the maximum flood and ebb currents, which occur on the rising and lowering tide since HSI has a standing tidal wave pattern, leading to a change in the volume of water over the course of the run within the inlet.
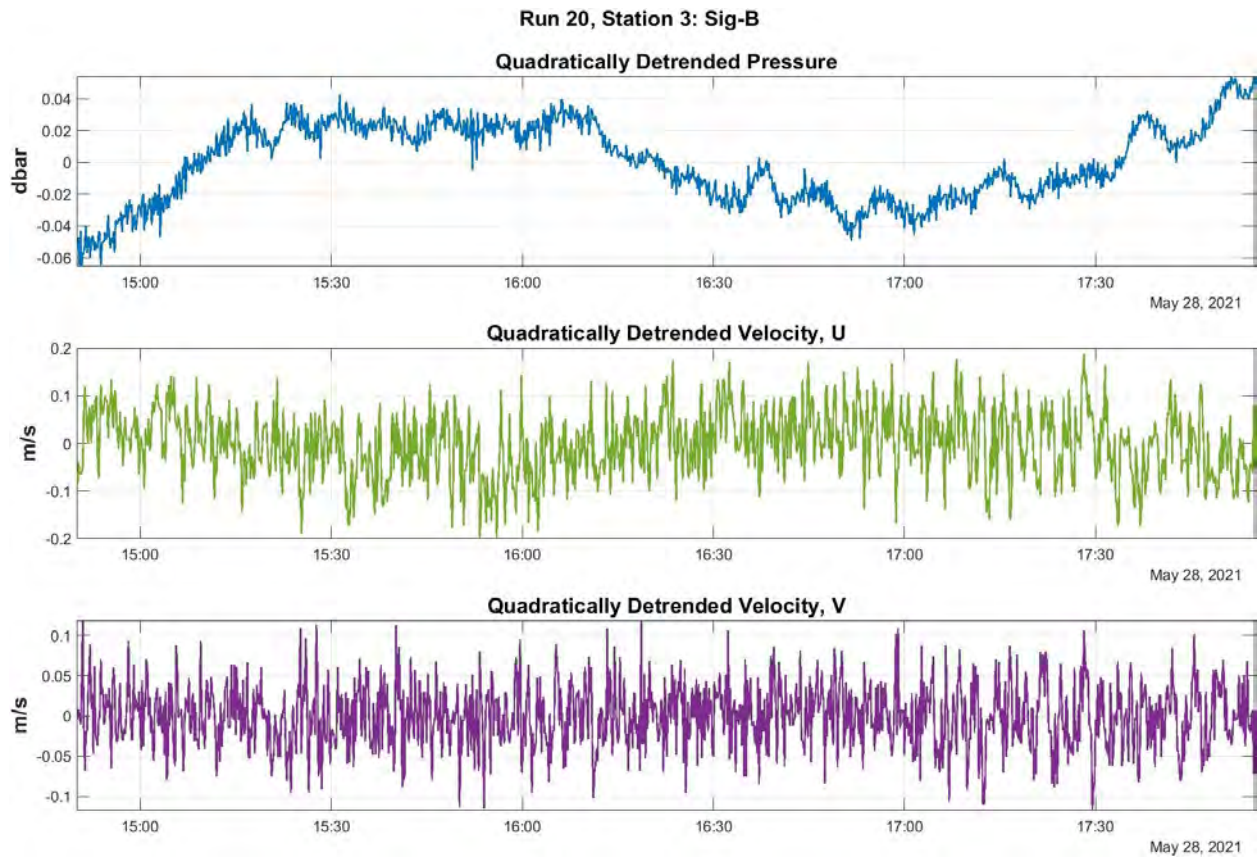
Figure 3.8. Station 3 (Signature-B ADCP) Run 20 quadratically detrended pressure (top row), u velocity (middle row), and v velocity (bottom row). Run 20 occurred during an ebb tide.
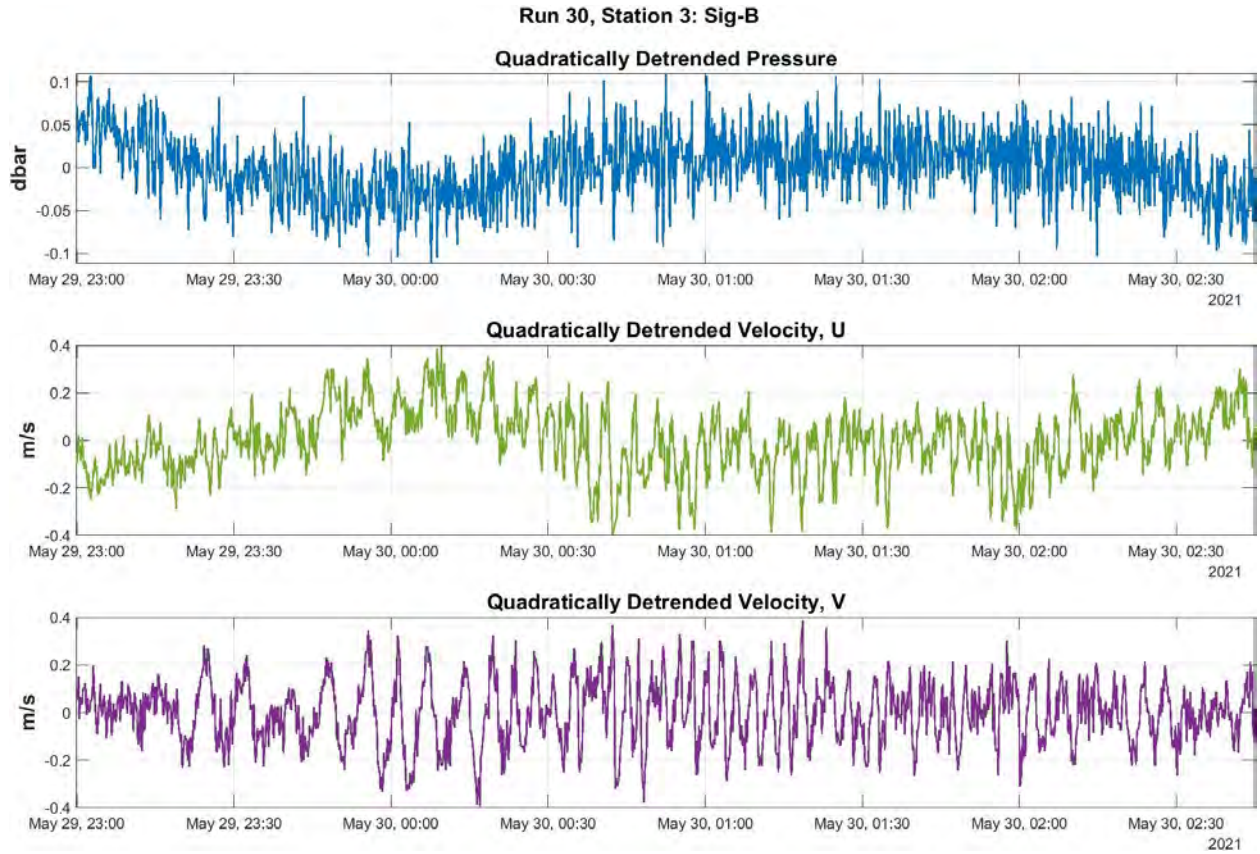
Figure 3.9. Station 3 (Signature-B ADCP) Run 30 quadratically detrended pressure (top row), u velocity (middle row), and v velocity (bottom row). Run 30 occurred during a flood tide.

3.5.2 Spectra, Velocity to Pressure Variance Ratios, and Instability Variance

The pressure and velocity (u, v) spectra along with the normalized velocity to pressure variance ratio, R, (Lippmann et al., 1999) for both Run 20 and 30 observed at station 3 are shown in Figure 3.10. There is high energy evident in velocity spectra over the infragravity frequency band (10^{-3} – 10^{-2} Hz) and the energy decreases at higher frequencies. The pressure spectra is elevated during Run 30, likely associated with the larger offshore incident gravity waves during the storm that may generate low frequency gravity waves. R values are high (>>1) throughout the infragravity frequency band during both Run 20 and Run 30 (Figure 3.10) indicating the flow is dominated by rigid-lid-like motions consistent with instabilities.
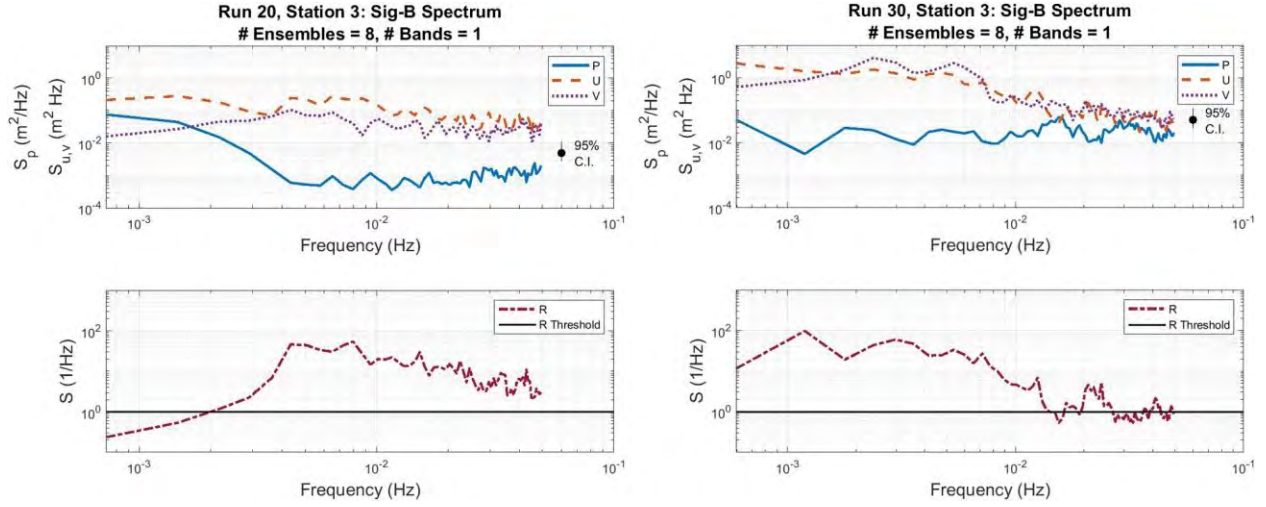
Figure 3.10. Station 3 (Signature-B ADCP) Run 20 (left) and Run 30 (right) spectrum of (upper plots) pressure (blue straight line), u velocity (orange dashed line), v velocity (purple dotted line), and (lower plots) velocity to pressure variance ratio, R (burgundy dashed-dot line) with the R threshold (black solid line). The 95% confidence interval is shown on the upper plots.

Time series of 30 min-averaged water levels and current speed from station 3 for the entire sampling period are shown in Figure 3.11. Also shown in Figure 3.11 are the 30-minute estimated R values averaged over the infragravity band for each station, and the mean over all stations. Using the mean R, the fraction of instability variance, α, was calculated and shown in Figure 3.11. During both flood and ebb flows, R values are much larger than 1 indicating the presence of rigid lid type motions. When R values are large (>>1), the fraction of instability variance, α, is close to 1 indicating the variance of the mean flow is primarily attributed to unstable motions. R values return to ~1 during weak flows as the tides change and the fraction of instability variance drops close to or below 0. R and α values are nearly the same for all tides, and do not show any variation associated with offshore wave conditions suggesting that the instabilities are driven by the tidal flows.

56
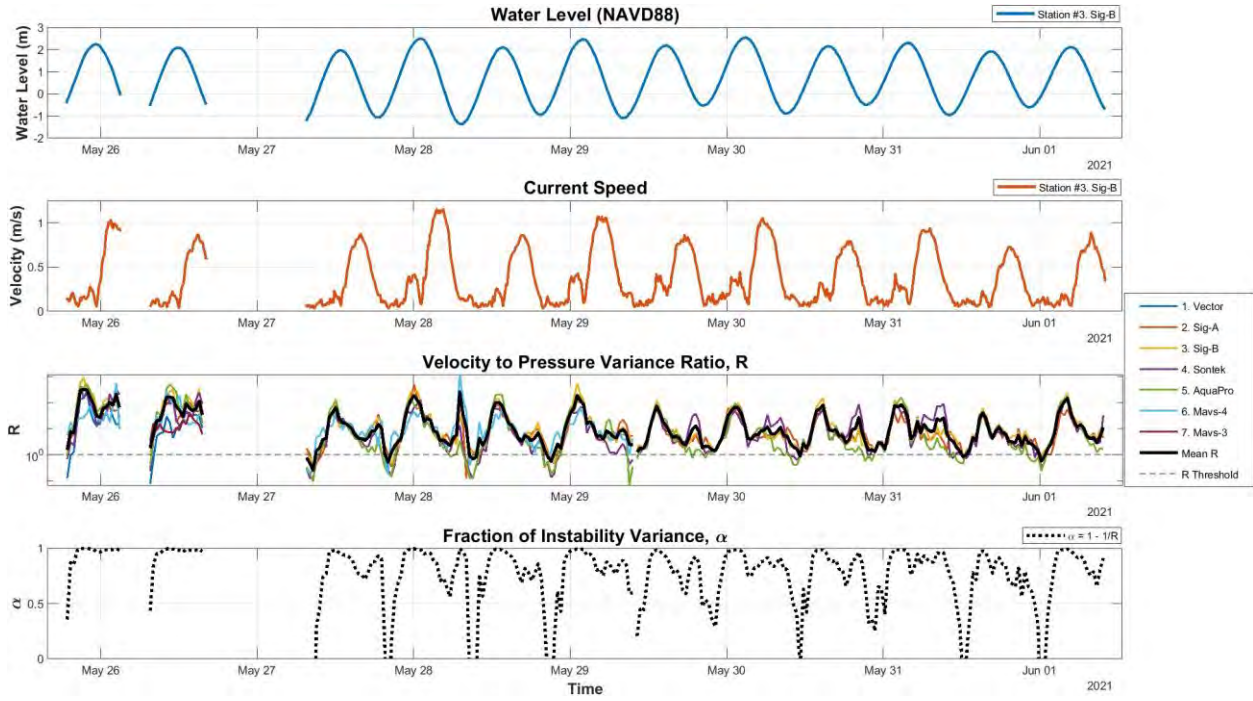
Figure 3.11. (Top) Thirty-minute mean water level relative to NAVD88 calculated from the pressure sensor on Station 3 (Signature-B ADCP). (Second row) Ten-minute mean current observed at Station 3 (Sig-B). (Third row) Velocity to Pressure Variance Ratio, R, for all ADCP stations over the deployment and the average R across the stations (solid black line) relative to the R threshold (black dotted line). (Bottom) The fraction of variance explained by the instabilities is represented using alpha = 1 – 1/R. The mean R was used in the alpha calculation.

3.5.3 Wavenumber-Frequency Spectra

Figure 3.12 and Figure 3.13 show the wavenumber-frequency spectra for Runs 20 and 30, respectively. The spectra computed with only the u and v components of the velocity are shown for each on the left and right, respectively. Concentrations of energy fall along nearly linear dispersion lines at infragravity frequencies. For both Runs 20 and 30, dominant wavenumbers (+/- 0.002 - 0.02 m^{-1}) of the low frequency motions (0.0006 - 0.01 s^{-1}) are resolved. Specifically in Run 20, the maximum energy in the wavenumber-frequency spectra of velocity spans 0.0007 – 0.01 Hz and 0.002 – 0.015 m^{-1}. In Run 30, the maximum energy in the wavenumber-frequency spectra of velocity spans 0.0006 – 0.008 Hz and -0.002 to -0.02 m^{-1}. The wavenumber for the

instabilities are too short to be gravity waves; the dispersion curves for the low mode edge waves are shown for comparison. The positive and negative wavenumbers of Run 20 and 30, respectively, indicate that the shear instabilities propagate in the same direction as the mean flow during both the ebb and flood tidal stages similar to instabilities of mean alongshore currents in the surf zone.
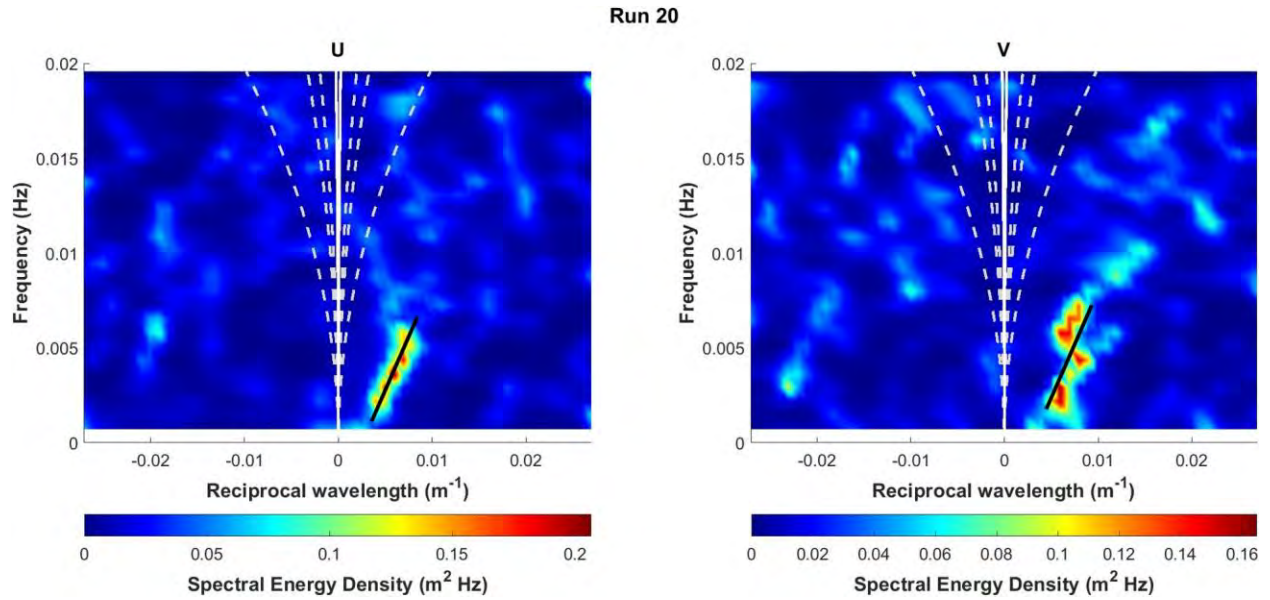
Figure 3.12. Wavenumber-Frequency spectra of the velocities, u (left) and v (right) for Run 20 on the ebb tidal stage on May 28, 2021. The white dotted lines show the modes of edge wave dispersion. The black line shows the slope of the shear instability dispersion curve, from which the speed of the shear instabilities can be estimated.

The propagation speed of the instabilities is determined from the slope of the linear relationship between frequency and wavenumber (Figure 3.12 and Figure 3.13). It is expected that if the maximum mean current in the center of the channel varies between 1.0 – 1.5 m/s (based on the cross-inlet ADCP transects), the instabilities speed will likely range between 25% - 50% of the mean speed based on linear stability theory (Chapter II). Run 30 shear instability phase speed is approximately 0.41 m/s (Figure 3.13), which is approximately 30% - 40% of expected maximum current. For Run 20, the instability propagation speed is roughly 0.72 m/s (Figure 3.12), approximately 50 – 70% of the expected max current.
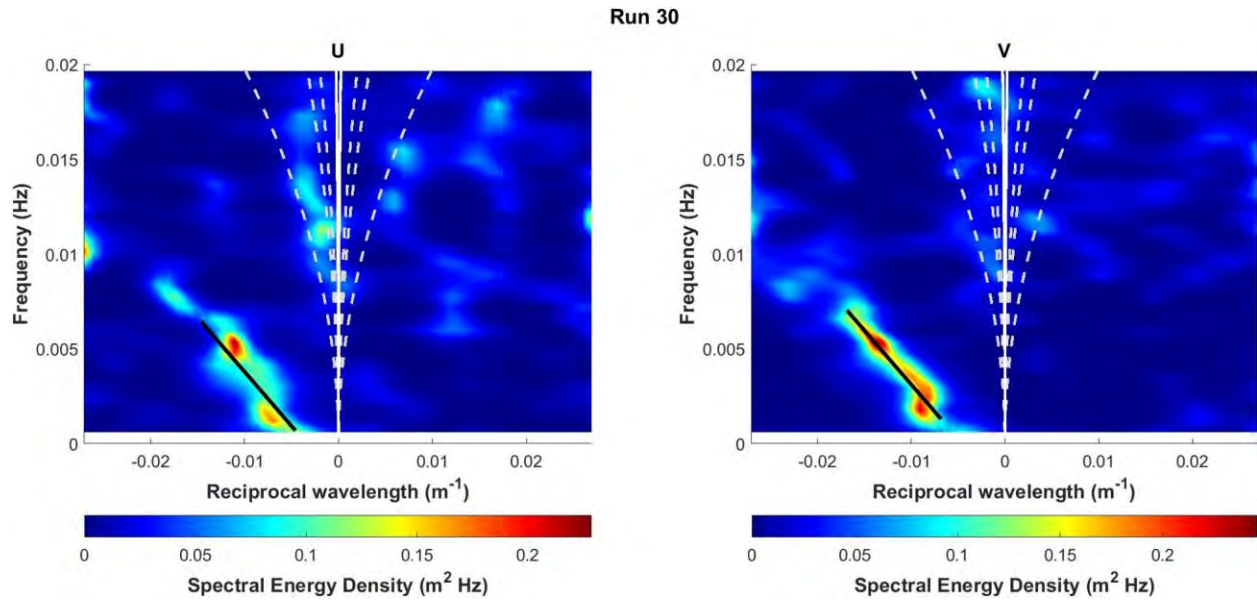
Figure 3.13. Wavenumber-Frequency spectra of the velocities, u (left) and v (right) for Run 30 on the flood tidal stage on May 29 - 30, 2021. The white dotted lines show the modes of edge wave dispersion. The black line shows the slope of the shear instability dispersion curve, from which the speed of the shear instabilities can be estimated.

Figure 3.14 shows the wavenumber-frequency spectra estimated from the pressure sensors across the array. Concentration of energy occurs along the lowest mode gravity wave dispersion curves, particularly in Run 30 where the offshore incident gravity waves were large. The energy falls slightly more towards negative wavenumbers for each Run indicating propagation of low mode edge waves into the inlet on both the ebb and flood tides. This is expected that incident gravity waves are generated offshore and consequently lead to low-frequency edge waves that propagate into the inlet, regardless of the tidal current direction. Concentrations of energy at high wavenumbers were not observed along the instability dispersion lines.

Wavenumber-frequency spectra from the other tidal cycles show similar results. Instabilities propagate in the direction of the flood or ebb tidal currents and do not show any sea

surface elevation signal. These results are consistent with R values in Figure 3.11 and linear instability theory.
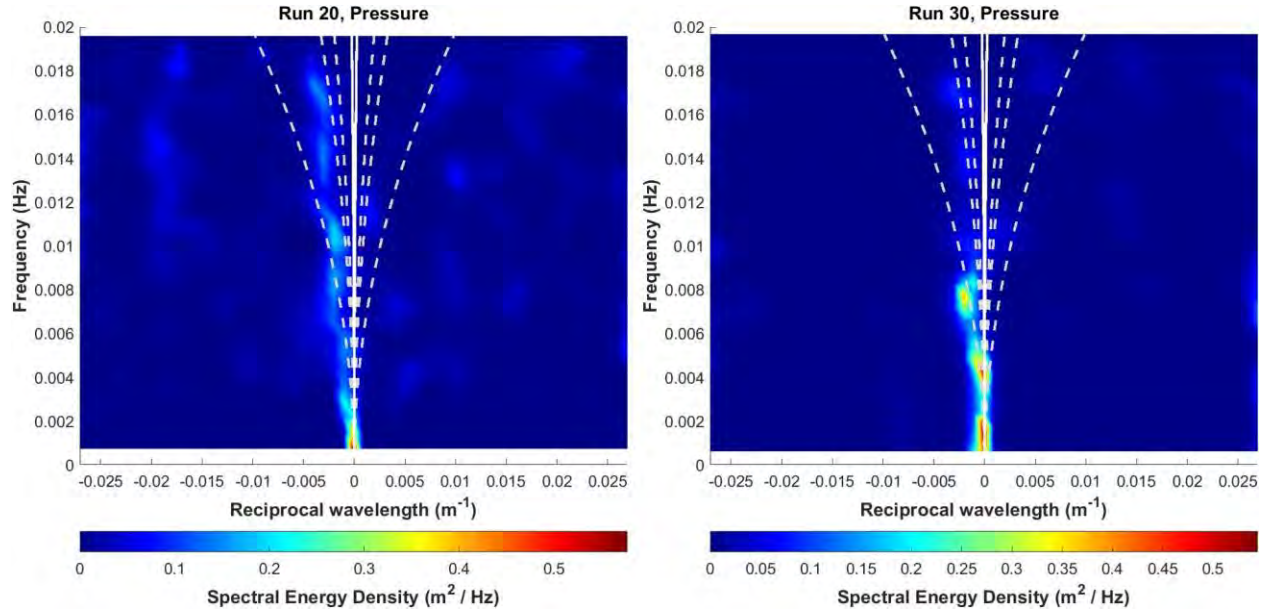
Figure 3.14. Wavenumber-Frequency spectra of the pressure for Run 20 (left) and Run 30 (right). The white dotted lines show the modes of edge wave dispersion.

3.5.4 Linear Instability Theory Comparison

The linear barotropic instability analysis solves the tertiary dispersion equation to predict the initial growth rates and associated wavelengths of the unstable modes (Chapter II). In order for an exponentially growing instability to develop, there must be an extremum in the background potential vorticity, $\frac{V_x}{h}$, and a positive imaginary root to the cubic dispersion equation (Bowen and Holman, 1989; Chapter II; Appendix C: Cubic Solution). Here, there are two extremums allowing for unstable modes to occur due to both the southern and/or northern shear (Figure 3.7; Baquerizo et al., 2001). Based on estimated HSI inlet geometry, bathymetry, and velocity structure, the linear barotropic instability analysis predicts the initial growth rates of instabilities with characteristic wavelengths $O(10^2 - 10^3 \text{ m})$ and frequencies $O(10^{-3} \text{ s}^{-1})$ (Figure 3.7). The range of unstable

60

wavelengths is 388 – 3000 m and the fastest growing unstable mode has a wavelength of 530 m, wavenumber of 0.0119 m^{-1}, frequency of 0.0023 s^{-1}, period of 1561.8 s, and phase speed of 0.34 m/s, which is ~23% of the 1.5 m/s maximum current.

3.6   Discussion

3.6.1   Observed Motions in HSI

Low frequency motions, O(10^{-3} – 10^{-2} s^{-1}) with dominant wavenumbers, O(10^{-3} – 10^{-2} m^{-1}) consistent with instabilities of the tidal flows were observed in the bounded Hampton/Seabrook tidal inlet on both the flood and ebb tides. These progressive, rigid-lid-like motions propagate in the direction of the mean tidal current and can lead to the meandering of the mean current and the spin-off of nonlinear eddies. The speed of propagation of the instabilities is 0.41 – 0.72 m/s, which is roughly 40 – 70% of the expected maximum mean tidal current flow in the center of the channel ranging between 1 – 1.5 m/s. Both the meandering of the flow and generation of eddies can cause horizontal mixing of momentum across the inlet that has implications to tidal energy resource assessments, the fate and transport of organic and inorganic matter, and small vessel safety and navigation.

The changing water levels during the max flood and ebb tidal current phase leads to a change in volume of water within in the inlet, the width of the flow, the cross-inlet velocity structure, and the relative location of the array to areas of the strongest shear. The oscillatory tidal signal can also be seen in the velocity to pressure variance ratio, R, over time (Figure 3.11). R peaks on flooding currents slightly before the high tides when the width of the flow is widest due to the higher water levels. When R values are large (>>1), the fraction of instability variance, α, is close to 1, indicating high energy in the infragravity band associated with rigid-lid-like motions

are consistent with instabilities. The secondary peak around low tides is associated with the instabilities present on the ebb tidal flows when there is a smaller volume of water in the inlet and the cross-inlet width of the flow is smaller.

3.6.2 Comparison to Nearshore Motions

The observed instability motions in the tidal inlet are consistent with observations of shear instabilities with similar characteristic wavelengths, frequencies, and speeds generated from the shear of the longshore current or rip currents in the nearshore (Oltman-Shay et al., 1989; Haller and Dalrymple, 2001; Geiman and Kirby, 2013). The lack of breaking wave group modulations within the bounded tidal inlet and the presence of the seaward propagating instabilities on the ebb flow (Run 20) indicate that the presence of the instabilities can be attributed to the shear of the tidal current. Thus, the generation of the unstable motions observed in the tidal inlet are not dependent on incident gravity wave groups as it has been hypothesized in the nearshore (Shemer et al., 1991; Long and Özkan-Haller, 2009).

3.6.3 Vortical Motions due to Bluff Bodies

On ebb tides, the shedding of vortices from the bridge pilings could occur leading to von Karman vortex shedding (Liu et al., 2018). This is seen with the horizontal variability in current direction and speed along ADCP transect Line 1 near the bridge (Figure 3.5). However, this cross-inlet velocity structure does not persist and the water column becomes well mixed again by transect Line 3 (Figure 3.4 - Figure 3.6) and is found to be well mixed even closer to the bridge (approx. transect Line 2) based on data collected in 2011 (McKenna, 2013). Additionally, Ortega-Casanova (2017) found vortex shedding from a rectangular cylinder length-to-width aspect ratios less than 1 (i.e. square cylinder) occurs in a constricted channel leading to strong mixing while flow around

rectangular cylinders with aspect ratios greater than 1 remains steady. The Hampton Harbor bridge pilings are rectangular with aspect ratios greater than 1 with lengths longer than widths oriented with the channel flow, and therefore are not expected to lead to as much vortex shedding as other pilings of circular or lower aspect ratio rectangular dimensions.

On the flood tide, the orientation of the southern jetty along with a rock outcrop located between stations 5 and 6 may present a classic flow separation problem as described in Signell and Geyer (1991). This would lead to the generation of vortices that spin off towards the center of the channel and thus, away from the sensor array observing the oscillatory motions. The vortices shed from the bridge pilings and/or rocks are expected to be advected at the speed of the mean flow (Halse, 1997), whereas the shear instabilities observed in HSI have phase speeds at a fraction (0.3 – 0.7) of the mean flow aligning with linear instability theory.

The frequency of the vortices shed from either the bridge pilings or rock outcrop can be estimated:

$$f = S\frac{U}{L} \qquad\qquad 3.1$$

where S is the Strouhal number, U is the freestream velocity, and L is the characteristic length scale of the body impeding the flow. In the case of the bridge pilings, L is the length of the bridge pilings in the along-channel direction (~10 m), which spans the width of the Hampton/Seabrook bridge. In the case of the rock outcrop, L is the diameter of the outcrop (~35 m). Strouhal numbers can vary depending on the flow conditions (typically characterized by the Reynolds number) as well as the shape and aspect ratio of the bluff body (Okajima, 1982; Lloyd and Stansby, 1997; Ortega-Casanova, 2017). Based on prior work, S is estimated to be ~0.2 for the rectangular bridge pilings (Okajima, 1982; Ortega-Casanova, 2017) and ~0.35 for the circular rock outcrop (Lloyd and Stansby, 1997). Given a max freestream velocity of 1.5 m/s (as observed in HSI), the

frequencies of vortices shed from either the bridge pilings or off of the rock outcrop are estimated to be >0.01 s^{-1}, which are higher than the dominant low frequency motions observed (<0.01 s^{-1}) in the lagged array. Therefore, the shed vorticities from the pilings and rocks are distinguishable as having faster phase speeds with slightly higher frequencies than the scales of the shear instabilities of interest here.

3.6.4 Comparison to Linear Theory

Based on the HSI geometry (i.e. deep center channel (6 m) and shallower lateral side shelves (~2 m) and current magnitudes (i.e. maximum 1.5 m/s), the linear barotropic instability analysis predicts the presence of instabilities with characteristic wavelengths $O(10^2 - 10^3$ m) and initial growth rates $O(10^{-3}$ s$^{-1})$ of the fastest growing modes (Figure 3.7). This aligns with the observed dominant frequencies of motion $O(10^{-3} - 10^{-2})$ s^{-1} with associated wavenumbers $O(10^{-3} - 10^{-2})$ m^{-1}. The phase speed of instability propagation observed is $40 - 70\%$ of the expected maximum mean currents, which is faster than the theoretical prediction of 23% of the max current. The slightly faster observed instabilities relative to the predicted speeds may be due to faster currents observed than expected and the inlet geometry funneling the flow and/or the simplicity of the barotropic linear stability analysis that does not account for nonlinearities and simply predicts initial growth rates versus motions reaching finite amplitudes. Although the linear instability analysis is limited in complexity, the results align with the energy observed along the dispersion lines estimated using data collected in the spatially lagged current meter array.

3.7 Conclusions

The presence of shear instabilities of tidal currents were observed in the bounded Hampton/Seabrook tidal inlet using a spatially lagged array of current meters. Iterative maximum

likelihood estimators were used to estimate the wavenumber-frequency spectra of the motions that are typically longer than the total length of the array. The wavenumber-frequency spectra showed concentrations of energy along dispersion lines with wavenumbers too high to be low mode gravity waves. In addition, normalized velocity to pressure variance ratios, R, and fraction of instability variance, α, show that the infragravity frequency band is dominated by rigid-lid-like motions, consistent with instabilities of the mean flow. On the other hand, wavenumber-frequency spectra of pressure records were consistent with low mode gravity waves, i.e. edge and leaky waves, and energy did not fall along the shear dispersion lines, supporting the linear instability theory. Shear instabilities are progressive, propagate in the direction of the mean tidal current at a speed of roughly 40 – 70% of the expected maximum mean tidal current and are too slow to be considered gravity waves, similar to observations of shear instabilities of mean longshore currents in the nearshore.

Incident gravity wave breaking occurs primarily outside of the inlet due to shoaling and refraction and along the southern bank of the inlet due to the jetties with minimal breaking inside the inlet. Although incident waves may propagate inside the inlet, the shear instabilities propagated out of the inlet on the ebb tide following the mean flow indicating the forcing is not due to surface gravity wave breaking at wave group time scales.

Observations of the shear instabilities are consistent with a theoretical linear instability analysis of tidal currents in a bounded inlet. The fastest growing wave modes are predicted to have wavelengths $O(10^2 – 10^3$ m) with initial growth rates of $O(10^{-3}$ $s^{-1})$, consistent with the characteristic scales of unstable motions observed in the inlet with frequencies of $O(10^{-3} – 10^{-2}$ $s^{-1})$ and dominant wavenumbers of $O(10^{-3} – 10^{-2}$ $m^{-1})$.

The existence of shear instabilities leads to ecosystem and hydrodynamic implications that should be considered. Tidal energy resource assessments depend on velocity to the third power and shear instabilities modulate the mean flow, affecting the velocity estimate. The meandering of the mean flow along with the spin-off of vortices leads to horizontal mixing of momentum across the inlet and can also affect the fate and transport of organic and inorganic matter.

CHAPTER IV

4 OBSERVATIONS AND MODELING OF INTENSIFIED TIDAL CURRENTS OVER A LATERAL SHELF IN A NARROW ESTUARINE CHANNEL

4.1 Abstract

The intensification of tidal currents over a lateral shelf in a narrow estuarine channel is investigated. Observations of mean currents along cross-river transects in the Piscataqua River within the Great Bay Estuary obtained from a vessel-mounted downward-looking acoustic Doppler Current profiler (ADCP) show that currents are strongest in the deeper channel leading up to the shelf and intensify over the shallow shelf at Henderson Point, both on the flood and ebb phases of the tidal flow. Numerical simulations using the Regional Ocean Modeling System (ROMS) with constant forcing and linearized bottom friction reproduce the general behavior of the flow. Similar to prior work examining the intensification of rip currents in the nearshore (Bowen, 1969), the potential vorticity balance is used to help explain and understand the physical dynamics. Results show that along-channel flow is intensified under high Reynolds number conditions where the inertial forces dominate over the frictional and viscous forces. The intensification of tidal currents over shallow regions of a bounded channel leads to spatial variability in cross-channel current velocity structure that modifies the lateral shear in mean flow, and can have implications on navigation, especially in constricted channels with limited maneuverability, tidal energy resource assessments, and the fate and transport of organic and inorganic matter.

4.2 Introduction

Tidally induced pressure gradients in sea level drive mean estuarine tidal currents that can have horizontal spatial variability across a bounded channel or inlet. This spatial variability can lead to a sheared cross-channel structure in along-channel velocity that is partially dependent on the inlet geometry and bathymetry. The mean velocity (i.e. time averaged flow over at least one hour and up to four hours) can be variable along the channel, leading to areas of velocity intensification (up to approx. 13% increase relative to the max speed) causing implications for vessel navigation, especially in constricted channels with limited maneuverability. The velocity intensification and spatial variability of the mean flow can significantly impact tidal current energy resource assessments, which depend on the flow magnitude to the third power (Lalander et al., 2013). The horizontal spatial variability of the mean estuarine flow can also be important for mixing and transport between inland bays, freshwater systems, and the coastal ocean (Bowden, 1965; Simpson et al., 1990; Geyer and MacCready, 2014).

Tidal current observations were collected in the Piscataqua River (Figure 4.1) in May 2015 during a spring tide, using a vessel-mounted acoustic Doppler current profiler (ADCP) equipped with bottom tracking. Cross-channel ADCP transects were collected during both flood and ebb tides along three transect lines spanning Henderson Point to Sullivan Point (Figure 4.2 and Figure 4.3). Both the depth-averaged (Figure 4.2) and depth varying (Figure 4.3) along-channel currents show strong lateral shear along all three transect lines and an intensification of velocity over the shallow lateral shelf off Henderson Point during both the flood and ebb currents. Topographic channeling by the bathymetric contours and the subsequent bottom friction is expected to lead to stronger currents in the deeper channel rather than on the shelf (Parker, 2007). For simplified topography of planar sloping beach in the nearshore (where Coriolis is neglected), Bowen (1969)

examined horizontal depth-averaged circulation and showed that strengthening of the seaward

currents (rip currents) occurred under increasing Reynolds numbers. Bowen's (1969) numerical

solutions of the circulation were found from the potential vorticity equation including nonlinear

advective terms (relative vorticity), dissipative terms in the form of either horizontal eddy viscosity

or a linear bottom friction, and constant radiation stress gradients (forcing terms) from breaking

incident surface gravity waves.

Herein, we investigate the forcing mechanisms driving the intensification of tidal currents

over the shallow areas at Henderson Point using the potential vorticity balance and conservation

of volume principles. For the estuarine case we are considering, the curl of the surface wind stress

is neglected, surface gravity wave forcing is zero, the Coriolis force, f, is ignored since the depth

and length scales of the estuarine channel, D, are much less than the Rossby radius of deformation,

$L_R = (gD)^{1/2}/f$, and the primary forcing of the currents is due to the tidally induced pressure

gradient. The forcing mechanism and resulting intensification of along-channel currents is

examined analytically through a non-dimensional analysis and numerically using a hydrodynamic

model that solves the 3-dimensional momentum equations.

Intensification and strong cross-channel shear in along-channel velocity may lead to

horizontal mixing of momentum across the channel. The strength of the horizontal mixing is

determined by the cross-channel gradient in Reynold's shear stress, S_{xy}. A nonzero Reynolds stress

can indicate the presence of unstable horizontal motions generated from a perturbation in the shear

of the mean current and the consequential transfer of energy from the mean flow to the perturbed

flow (Dodd and Thornton, 1990; Appendix E: Unstable Motions in the Piscataqua River). It is

expected that the (possibly asymmetric) mixing of momentum will act to smooth the cross-channel

velocity structure and modify the shear in along-channel flow.

The goal of this study is to gain a better understanding of the forcing and implications of the intensification of estuarine tidal current velocity and the resulting horizontal spatial variability of the mean flow through a narrow, bounded inlet or channel and the consequential mixing of momentum. Numerical experiments are conducted that approximate natural field conditions in the Piscataqua River by solving the 3-dimensional nonlinear momentum equations to qualitatively assess the forcing conditions that produce the observed spatial structure of the mean along-channel tidal currents. The depth averaged velocity is analyzed after the model has spun up and the mean currents are quasi-steady. Non-dimensional analysis is used to solve for the Reynolds number that describes the strength of the inertial terms relative to the viscous forces, and the model input parameters are modified to simulate runs under both high and low Reynolds numbers. The detailed methods are discussed below followed by a discussion and concluding remarks.
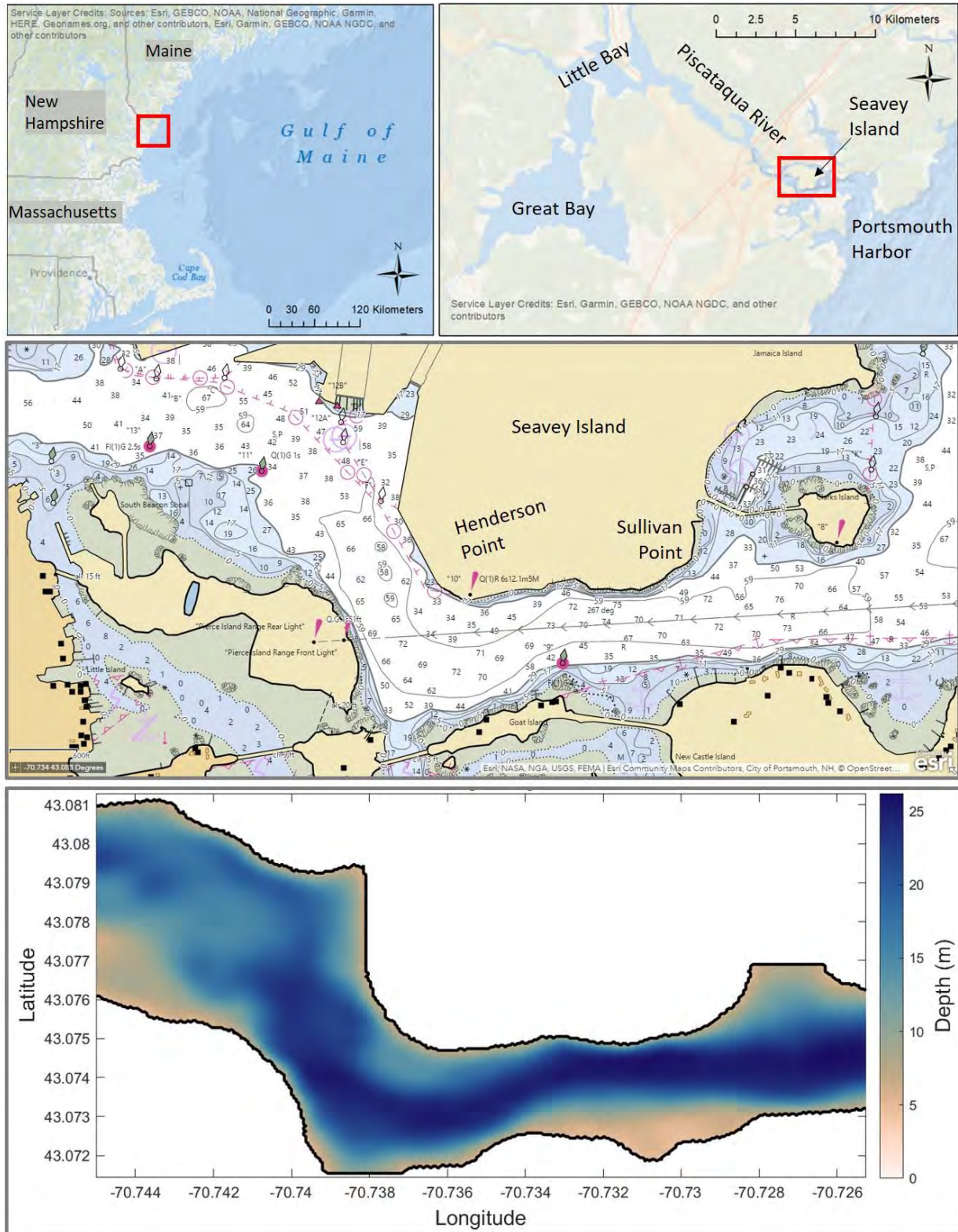
Figure 4.1. (Top left) Study area shown in the red box along the New England coast and Gulf of Maine. (Top right). Great Bay Estuary with the study area shown in the red box. (Middle) NOAA nautical chart (feet, MLLW) of the study area. (Bottom) Bathymetry (m) used in ROMS.
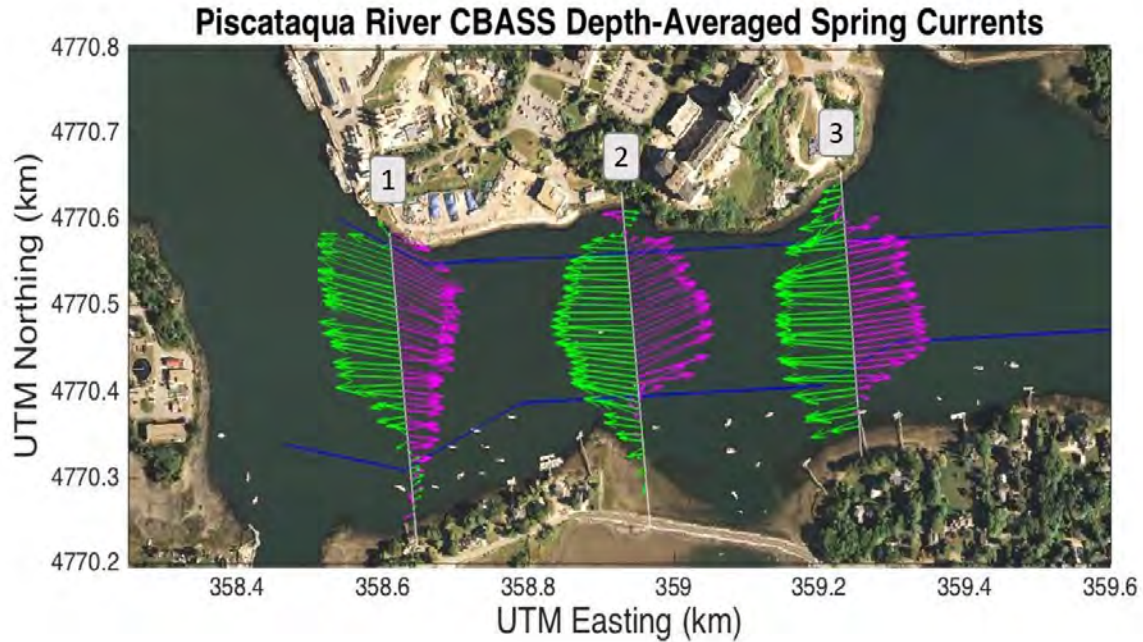
Figure 4.2. Depth-averaged flood (green) and ebb (purple) tidal currents observed from cross-river ADCP transects on May 2015 during spring tide. Transect lines are labeled from west to east: 1 (off Henderson Point), 2, and 3 (off Sullivan Point).
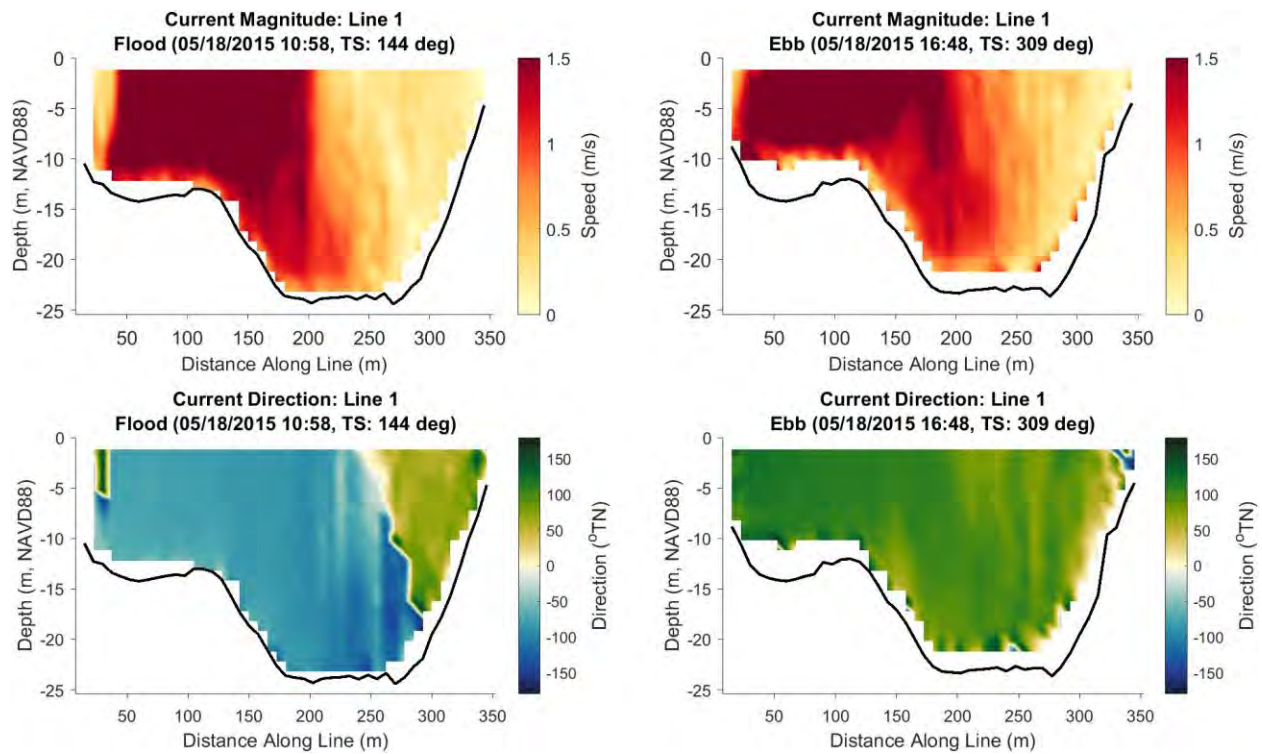
Figure 4.3. Current magnitude (top plots) and direction (bottom plots) along transect line 1 during flood (left column) and ebb (right column) tidal stages observed from cross-river ADCP transects on May 18, 2015.

4.3 Study Site: Piscataqua River

The study site focuses on the flow south of Seavey Island, home of the Portsmouth Naval Shipyard, in the lower Piscataqua River that connects the Great Bay Estuary in New Hampshire to the Gulf of Maine (Figure 4.1). Water depths are about 25 m in the center of the channel, and shallow abruptly to approximately 12 m at Henderson Point over a shallow ledge. The tide range (between lower-low water, LLW, and higher-high water, HHW) varies between 2 – 4 m based on the neap – spring cycle, respectively, and maximum flood and ebb currents can exceed 2 m/s, especially during spring tides (Swift and Brown, 1983; Cook and Lippmann, 2017). Freshwater river discharge is typically less than 2% of the tidal prism while meteorological subtidal and wind-induced flows are of second order relative to the dominant M_2 tidal forcing, leading to small density gradients and a well-mixed estuary (Swift and Brown, 1983; Trowbridge, 2007; Wosnik et al., 2014; Cook and Lippmann, 2017).

The primary force balance in the estuary is between the frictional bottom stress and the pressure gradient force (Swift and Brown, 1983; Ertürk et al., 2002). The tidal wave in the lower Piscataqua River near the mouth shows partially progressive characteristics and then transitions to standing wave behavior further upriver (Cook and Lippmann, 2017). The lower Piscataqua River is found to be highly dissipative with 40% of the M_2 tidal amplitude decaying over a 12 km area (Swift and Brown, 1983; Ertürk et al., 2002; Cook and Lippmann, 2017; Cook et al., 2019). A detailed description of the flow throughout the entire Great Bay Estuary can be found in Cook (2019). The Froude number, $Fr = \frac{U}{\sqrt{gH}}$, (ratio of inertial to gravity forces) is less than 1 in both the deeper channel (~25 m) and over the shallower shelf (~12 m) where the depths are large relative to mean velocities (1 – 2 m/s), indicating that the flow is subcritical.

4.4 Methods

In the following, we describe the observations of along-channel currents that show an intensification over the shallow shelf near Henderson Point. We then describe the shallow water (depth-averaged) equations of motion and show theoretically the importance of the inertia of the flow and frictional terms (through the Reynolds number) in the vorticity balance. We then describe the hydrodynamic model that solves the 3-dimensional fully nonlinear model for the study site topography with constant (steady) forcing for flood and ebb tidal currents. An analysis of a lagged linear array horizontal velocity component time series to characterize the unsteady motions that can lead to cross-channel S_{xy} gradients is included in Appendix E: Unstable Motions in the Piscataqua River.

4.4.1 Cross-Channel ADCP Transects

Observations of the ebb and flood tidal currents were obtained from cross-channel transects on 18 May 2015 during the spring tide using the Coastal Bathymetry Survey System (CBASS; Lippmann and Smith, 2009) equipped with a downward facing Teledyne RDI 600 kHz Workhorse acoustic Doppler current profiler (ADCP) with bottom tracking capability (McKenna, 2013; Gagnon, 2018). The ADCP was calibrated prior to deployment and collected data in 0.5 m size bins vertically throughout the water column. Data were quality controlled by discarding data near the bottom due to sidelobe interference and filtering spurious data more than three standard deviations from the mean. Several vessel passes along each transect were averaged together over a 24-minute duration for the flood case and 14-minute duration for the ebb case. The 3-dimensional currents were averaged vertically over two depth bins and binned spatially into 15 m wide overlapping sections. Comparisons between CBASS-derived mean flow and direction with bottom mounted

(fixed) upward-looking ADCP data show that current magnitudes and directions are highly correlated (R^2 values of 0.97 and 0.96, respectively) and have RMS errors of 4.5 cm/s and 17°, respectively (McKenna, 2013). The observations are qualitatively compared to the numerical model output along similarly located cross-channel transects.

4.4.2 Analytical Equations of Motion

The shallow water (depth-averaged) horizontal momentum equations under the assumptions that the flow is non-divergent and incompressible, Coriolis is neglected, surface wind stress is ignored, there is no incident gravity wave motion, and including both linearized bottom friction and horizontal eddy viscosity terms, are given by

$$\frac{\partial u}{\partial t} + u\frac{\partial u}{\partial x} + v\frac{\partial u}{\partial y} = -g\frac{\partial \eta}{\partial x} - \frac{\lambda}{h}u + A_H\left(\frac{\partial^2 u}{\partial x^2} + \frac{\partial^2 u}{\partial y^2}\right)$$

$$\frac{\partial v}{\partial t} + u\frac{\partial v}{\partial x} + v\frac{\partial v}{\partial y} = -g\frac{\partial \eta}{\partial y} - \frac{\lambda}{h}v + A_H\left(\frac{\partial^2 v}{\partial x^2} + \frac{\partial^2 v}{\partial y^2}\right)$$

(4.1)

where η is sea surface elevation, λ is the bottom drag coefficient, A_H is the constant eddy viscosity, g is gravity, t is time, and h is the water depth. The continuity equation is given by

$$\frac{\partial}{\partial x}(uh) + \frac{\partial}{\partial y}(vh) = 0$$

(4.2)

The horizontal cross-channel (y-directed) and along-channel (x-directed) velocities, v and u, respectively, can be represented in terms of a mass transport stream function, ψ, such that

$$uh = -\frac{\partial \psi}{\partial y}, \quad vh = \frac{\partial \psi}{\partial x}$$

(4.3)

After cross-differentiating and subtracting the u and v momentum equations (4.1), the sea surface elevation terms are eliminated. Inserting (4.3), using (4.2), and rearranging terms results in the potential vorticity equation

75

$$\frac{D}{Dt}\left(\frac{\xi}{h}\right) = -\xi\frac{\lambda}{h^2} - \frac{\psi_y}{h^2}\left(\frac{\lambda}{h}\right)_y - \frac{\psi_x}{h^2}\left(\frac{\lambda}{h}\right)_x + \frac{A_H}{h}\nabla^2\xi \qquad (4.4)$$

where $\xi = \frac{\partial v}{\partial x} - \frac{\partial u}{\partial y}$ is the relative vorticity and the subscripts represent derivatives. For steady

(mean) currents, (4.4) can be rewritten as

$$-\frac{\psi_y}{h}\left(\frac{\xi}{h}\right)_x + \frac{\psi_x}{h}\left(\frac{\xi}{h}\right)_y = -\xi\frac{\lambda}{h^2} - \frac{\psi_y}{h^2}\left(\frac{\lambda}{h}\right)_y - \frac{\psi_x}{h^2}\left(\frac{\lambda}{h}\right)_x + \frac{A_H}{h}\nabla^2\xi \qquad (4.5)$$

Equation (4.5) is similar to Bowen (1969) without wave forcing terms and eliminating either λ or

A_H term. Equation (4.5) are nondimensionalized using characteristic horizontal length (L), velocity

(U), and depth (H) scales

$$x = x'L \qquad\qquad v = v'U$$

$$y = y'L \qquad\qquad \xi = \xi'\frac{U}{L}$$

$$h = h'H \qquad\qquad \psi = \psi'ULH$$

which yields the non-dimensional, nonlinear potential vorticity equation

$$-\frac{U}{L}\frac{1}{h'}\frac{\partial\psi'}{\partial y'}\frac{\partial\xi'}{\partial x'h'} + \frac{U}{L}\frac{1}{h'}\frac{\partial\psi'}{\partial x'}\frac{\partial\xi'}{\partial y'h'} =$$
$$-\frac{\lambda}{H}\frac{\xi'}{(h')^2} - \frac{\lambda}{H}\frac{1}{(h')^2}\frac{\partial\psi'}{\partial y'}\frac{\partial}{\partial y'h'} - \frac{\lambda}{H}\frac{1}{(h')^2}\frac{\partial\psi'}{\partial x'}\frac{\partial}{\partial x'h'} + \frac{A_H}{L^2}\frac{1}{h'}\left(\frac{\partial^2\xi'}{\partial(x')^2} + \frac{\partial^2\xi'}{\partial(y')^2}\right) \qquad (4.6)$$

The Reynolds number shows the strength of the inertial terms (left-hand-side) relative to the

viscous terms (right-hand-side), and is given by

$$Re = \frac{ULH}{\lambda L^2 + A_H H} \qquad (4.7)$$

This form for Re is the same as in Bowen (1969) if $H = L$ and the λ term is ignored. While keeping

U, H, L, and A_H the same for each hydrodynamic model run (described next), the Reynolds number

can be varied through changes in the bottom drag coefficient, λ. The eddy viscosity coefficient,

A_H, was set as small as possible while maintaining numerical stability and is used for turbulence

closure schemes and in parameterizing subgrid-scales of horizontal mixing and was not used in varying the Reynolds number conditions (i.e. remained constant).

4.4.3 Numerical Hydrodynamic Model Configuration

The nonlinear Navier Stokes momentum equations are solved using the Regional Ocean Model System (ROMS), which uses the hydrostatic and Boussinesq approximations on the Arakawa C-grid in the horizontal with a terrain following vertical structure (sigma coordinates; Haidvogel et al., 2008; Hedström, 2018). The 3-dimensional momentum equations were solved over a 4 hour model run time using a 0.5 second baroclinic time step and a 20 second barotropic step. Coriolis is assumed negligible and not included ($f = 0$). Relevant ROMS model parameters are listed in Table 4.1.

Table 4.1. ROMS Model Parameters.

Parameter	Description	Value
DX, DY	Horizontal grid resolution	5 m
N	Number of vertical layers	10
DT	Baroclinic time step	0.5 s
NDTFAST	Barotropic time step	20
VISC2	Horizontal viscosity coefficient	0.1 m^2/s
RDRG	Linear bottom drag coefficient	10^{-4} m/s – 10^{-2} m/s
VTRANSFORM	Vertical s-coordinate transformation equation	2
VSTRETCHING	Vertical s-coordinate stretching function	4
THETA_S	Vertical s-coordinate surface stretching parameter	2
THETA_B	Vertical s-coordinate bottom stretching parameter	4
GAMMA2	Slipperiness condition variable	-1 (no slip)
VOLCONS(EAST, WEST)	Conservation of volume	True

The model uses smoothed bathymetry of the Piscataqua River collected from several sources that were compiled and interpolated to create a digital elevation model referenced to mean sea level (MSL) as described in Cook et al., (2019). The elevation data was extracted and input into the Easygrid routine (available at https://www.myroms.org/wiki/easygrid) to create the high-resolution, ROMS-compatible model grid. A 2 m depth offset was applied to the total depth throughout the domain to allow for model stability, which is roughly 16.7% depth increase over the shelf. There are ten vertical levels and the horizontal grid resolution is 5 m making up a 1600 m by 1090 m long domain (319 by 217 grid cells) in the x- and y-directions, respectively (Figure 4.4).
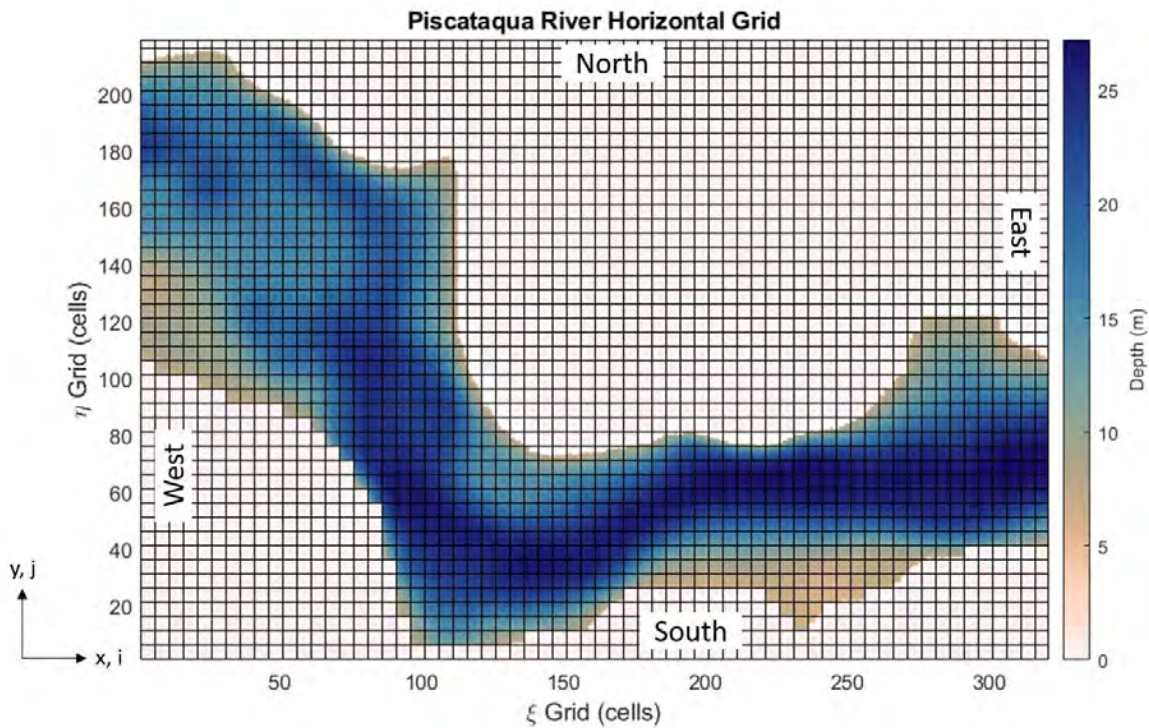
Figure 4.4. ROMS horizontal grid of the Piscataqua River south of Seavey Island. Displayed gridlines are every 25 meters, decimated by a factor of five from the actual model grid for display purposes. The grid is not rotated, so the cardinal directions correspond to the grid boundaries.

The surface wind stress is set to 0 m/s. The bottom stress is parameterized using a spatially uniform bottom drag coefficient, λ, which ranged between 10^{-4} m/s and 10^{-2} m/s and is applied linearly to the velocity (Table 4.2). The drag coefficient is consistent with Swift and Brown's (1983) bottom drag coefficient, C_F, estimates ranging 0.015 to 0.054 based on observations in the estuary using the quadratic drag law, $C_F = \frac{\tau_b}{\rho U^2}$. Cook et al. (2019) modeled the Great Bay Estuary where bottom friction logarithmically depended on the bottom roughness coefficient, Z_{ob} = 0.02 m, and the results showed that a single dissipation value yields reasonable results despite varying seafloor characteristics throughout the estuary. The choice of drag coefficient here is also consistent with the range of estimates of bed shear stress coefficients in other tidal estuaries, 0.001 – 0.01, (Ludwick, 1975; Winterwerp and Wang, 2013), as well as in the nearshore environment, 0.001 – 0.009 (Thornton and Guza, 1986; Whitford and Thornton, 1996; Özkan-Haller and Kirby, 1999).

Table 4.2. Model run configurations. The Reynolds Number is calculated using the characteristic velocity (U) of 1 m/s, depth (H) of 12 m and length scale (L) of 200 m, which is the approximate depth and along-channel length of the lateral shelf off Henderson Point. The eddy viscosity coefficient (A_H) is 0.1 m^2/s for all model runs. The mean and maximum current are calculated over the entire domain over the last hour of the model run.

	Run A	Run B	Run C	Run D
Current stage	Ebb	Ebb	Flood	Flood
Friction (RDRG, λ)	1e-4	1e-2	1e-4	1e-2
Reynolds number, R_e	462	6	462	6
Mean current speed	0.53 m/s	0.52 m/s	0.52 m/s	0.44 m/s
Max current speed	1.86 m/s	1.64 m/s	1.66 m/s	1.57 m/s

The horizontal viscosity depends on the harmonic mixing coefficient (A_H used in expressions above and called VISC2 in ROMS), which is set to 0.1 m^2/s (Table 4.1). This allows for nonlinear unstable motions to be resolved while the model remains numerically stable. A third order upstream advection scheme is used to solve for horizontal advection of three-dimensional

momentum. A fourth order centered vertical advection scheme is used to solve for vertical advection of momentum. A $k - \varepsilon$ generic length scale (GLS) turbulence closure scheme (Warner et al., 2005) in conjunction with the Kantha and Clayson (1994) stability function are used to parameterize the vertical turbulent mixing of momentum and tracers. Mixing of momentum and tracers occurs along terrain-following sigma surfaces.

The lateral boundary conditions are open on the eastern and western boundary and closed on the northern and southern boundary with a no-slip lateral condition (Figure 5). After linearly ramping up from rest over a one hour period, quasi-steady currents are imposed with clamped east-west velocities, u (baroclinic flow) and $\bar{u}$ (barotropic flow, where the overbar indicates depth-averaged), on either the western boundary to simulate ebbing currents or on the eastern boundary to simulate flooding currents (Figure 4.5). The cross-channel velocity structure has a sheared profile reaching a maximum of 1.0 m/s near the deeper area of the channel and linearly decreasing to 0 m/s near the shallow bounding sides (i.e. northern and southern boundaries). The maximum current velocity was chosen based on Cook and Lippmann (2017) numerical results that showed maximum depth averaged currents ranging between $1 - 2$ m/s in the estuary, consistent with observations in the area. The results were not sensitive to the cross-channel velocity structure chosen for inflow conditions and the profile used is based off of expected conditions given the bathymetry and channel geometry. The outgoing flow boundary (i.e. eastern boundary with ebbing currents or western boundary with flooding currents) is set to allow disturbances in the free surface and velocities (both barotropic and baroclinic) to radiate out of the domain at the speed of gravity waves. The total volume is conserved.
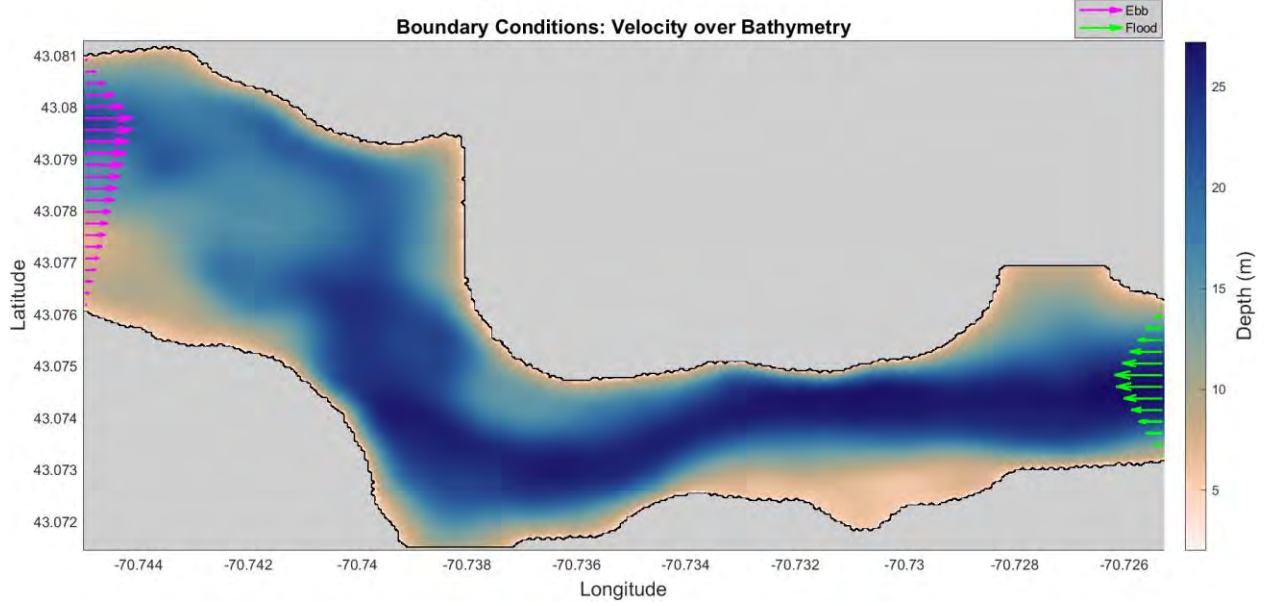
Figure 4.5. Boundary conditions. The magenta velocity vectors along the western boundary are used for ebb flow model runs and the eastern boundary is set to the radiation condition. The green velocity vectors along the eastern boundary are used for flood flow model runs and the western boundary is set to the radiation condition. The maximum velocity for both the ebb and flood case is set to 1 m/s near the deep area of the channel and linearly decreases to 0 m/s near the shallows on either side to the north and south. The northern and southern boundaries are closed for all runs.

4.4.4 Model Output Analysis

The velocities are averaged over the last hour at which time the currents are considered to have adjusted to bathymetric and inlet geometric features. The potential vorticity, $\pi_s = \frac{v_x - u_y}{h}$, is calculated using the time and depth averaged velocities and the derivatives in the x- and y- directions (subscripts) are calculated between neighboring grid cells every 10 m. The stream function is calculated by integrating the time and depth averaged velocities, $\psi = \int (\bar{u}h \, dy - \bar{v}h \, dx)$.

The time-averaged (indicated by the larger overbar) Reynolds shear stress of the depth-averaged turbulence velocities, u', v', (i.e. the residuals after removing the mean flow over the last hour of the model run) is calculated by

81

$$S_{xy} = \overline{\int_0^y u'\,v'\,dy} \qquad (4.8)$$

and shows the relative magnitude of mixing of along-channel (x-direction) momentum across the channel (y-direction) resulting from the unstable flow and subsequent transferring of energy from the mean flow to the turbulent flow. This mixing occurs at scales associated with the instabilities of the mean current and includes the subgrid-scale mixing parameterized by the eddy viscosity coefficient (A_H). The Reynolds shear stress was calculated along similar transects (T1, T2, and T3) as those occupied in 2015 (Figure 4.6).
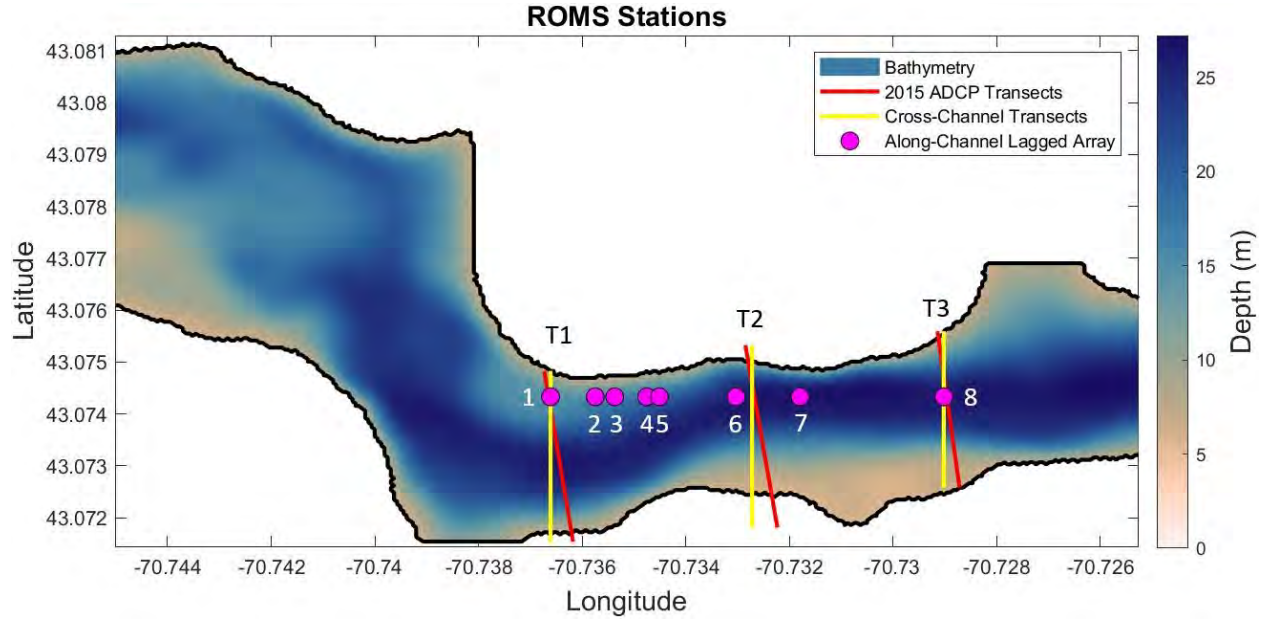
Figure 4.6. The yellow lines represent the ROMS cross-channel transects in latitude (y-direction) and named T1 (west), T2 (middle), and T3 (east). These three transects are in similar locations to the 2015 ADCP transects (red lines). The magenta dots represent the along-channel spatially lagged ROMS array (used in the analysis described in Appendix E), where stations 1 (west) and 8 (east) are also stations in T1 and T3, respectively.

4.5 Results

4.5.1 Ebbing Currents

The mean ebb velocity for both model Runs A (Re = 462, λ = 10^{-4}) and B (Re = 6, λ = 10^{-2}) have an intensification of velocity over the lateral shelf off of Henderson Point (Table 4.2; Figure 4.7 and Figure 4.8) and slower velocity in the adjacent deeper channel (Figure 4.2 and Figure 4.3). The high Reynolds number (low friction) condition (Run A) shows faster speeds than the low Reynolds number (high friction) condition (Run B) over the shelf by approximately 0.2 m/s corresponding to a 13% increase in the maximum speed (Figure 4.8). This intensification of velocity over the shelf is also seen by the convergence of streamlines in the high Reynolds number (low friction) condition (Run A) relative to the low Reynolds number (high friction) condition (Run B; Figure 4.9). These results are qualitatively similar in character to Bowen's (1969) results for their nearshore circulation study.
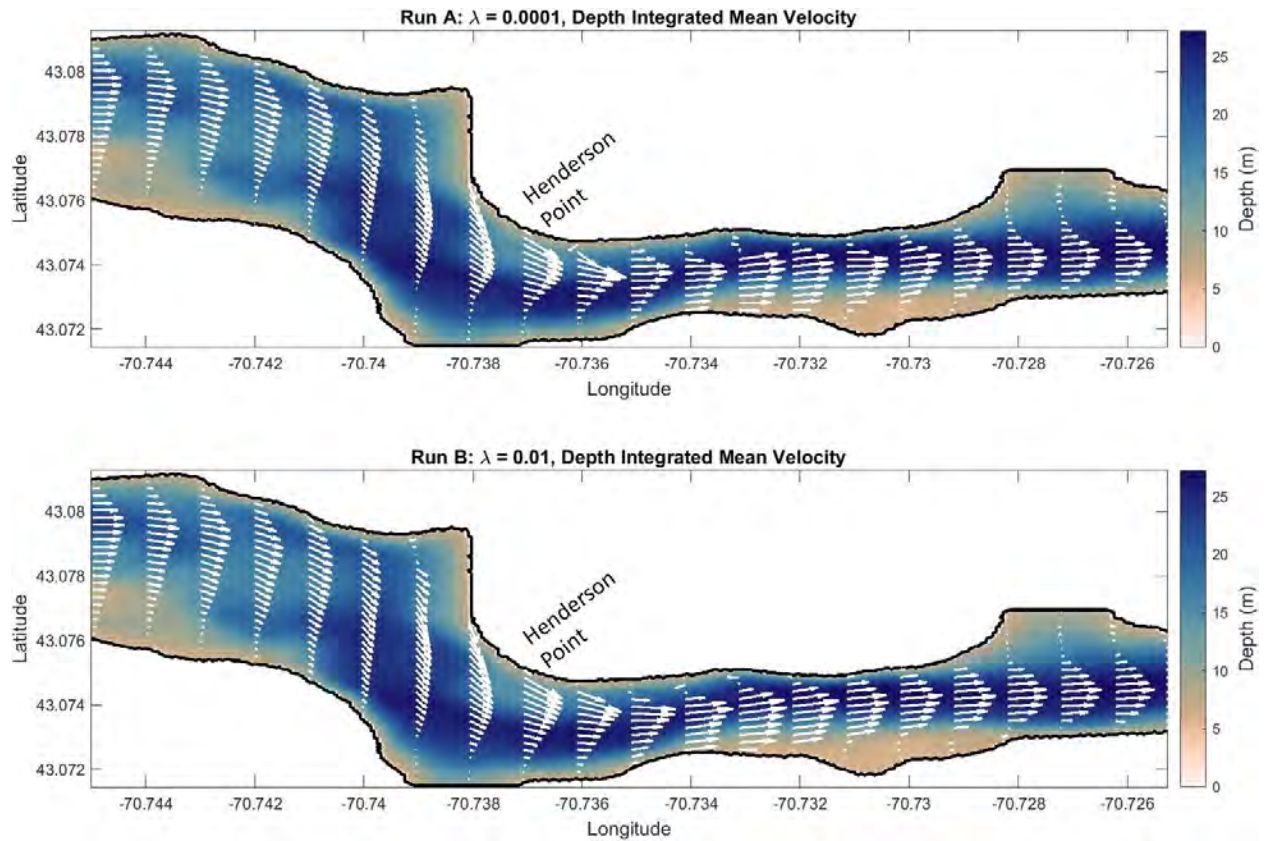
Figure 4.7. Depth integrated mean velocity over bathymetry for ebbing current Runs A (top) and B (bottom). Vectors are scaled to 1.5 m/s. The mean is calculated over the last hour of the model run.

On the ebb flow, there is a circulation cell south of Seavey Island centered near transect line 2 (Figure 4.2) between Henderson and Sullivan Points opposing the mean flow direction for both low and high Reynolds number cases (Figure 4.7), which is similarly observed by the 2015 ADCP transects (Figure 4.2). This circulation cell is not present in the numerical results (Figure 11) or in observations collected during flood currents (Figure 4.2).
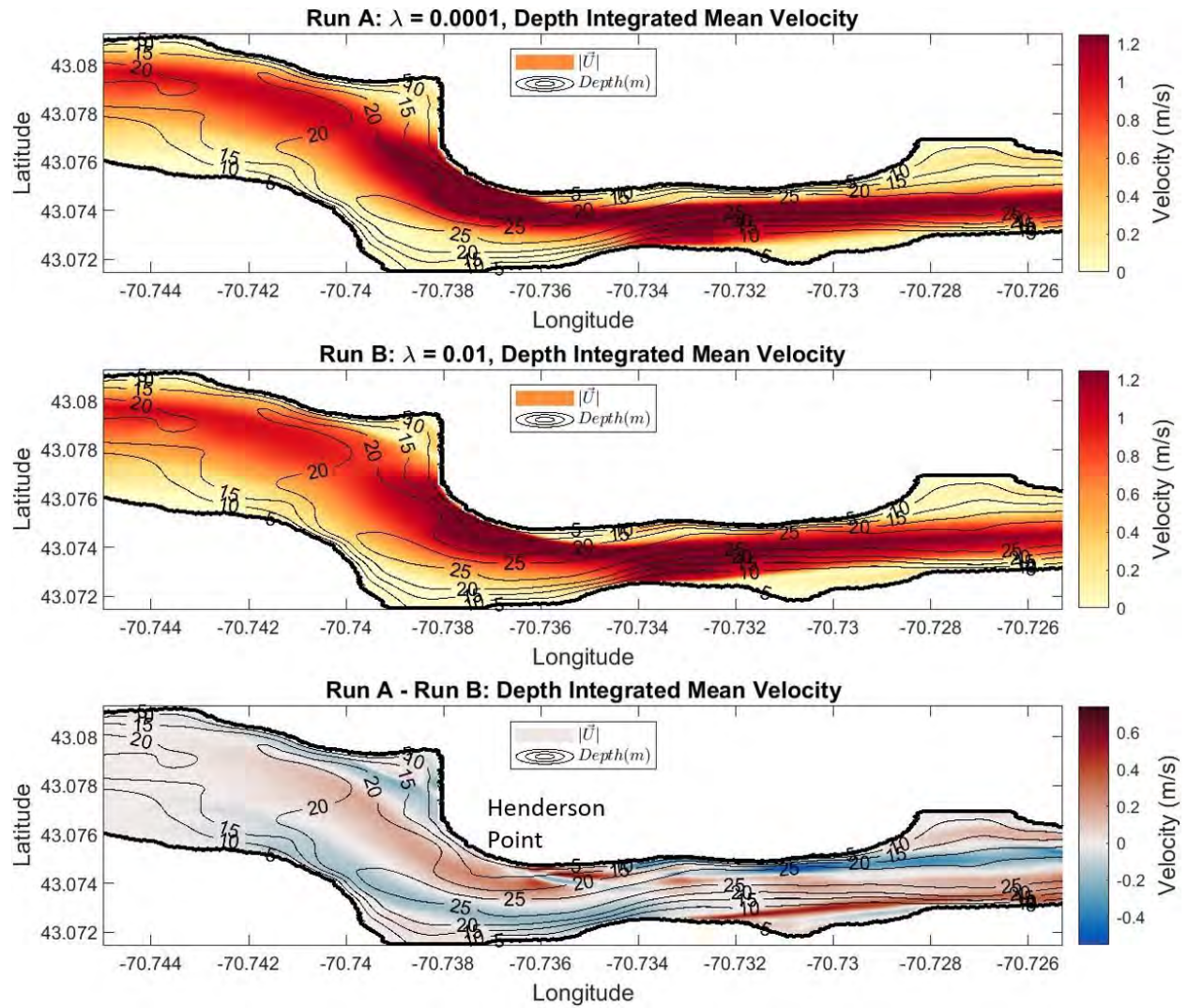
Figure 4.8. Depth integrated mean ebb current magnitude for Runs A (top) and B (middle) and the difference between the two (bottom). Depth contours are shown as black lines and labeled. The mean is calculated over the last hour of the model run.
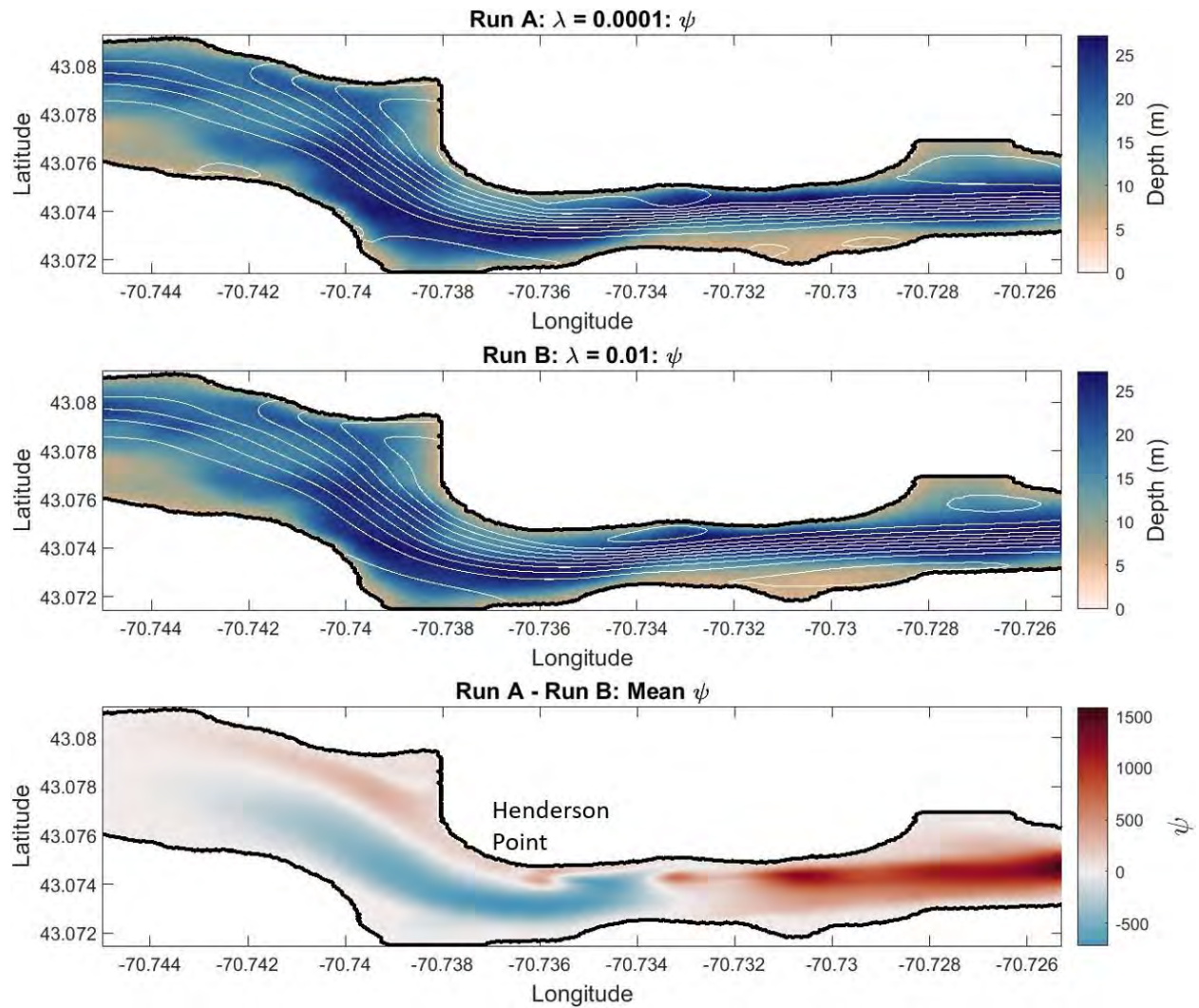
Figure 4.9. The stream function (white lines) over bathymetry for ebbing current Runs A (top) and B (middle) and the difference between the two runs (bottom). The stream function is calculated using the depth-averaged, mean velocities over the last hour of the model run.

The low Reynolds number condition (Run B) with ebbing current shows steadier mean flow than the high Reynolds number condition (Run A) due to the high friction dampening the unstable motions downriver, as seen in the potential vorticity with less spin-off of vorticity in the form of eddies (Figure 4.10). The gradient in the potential vorticity over the shelf off Henderson Point is sharper in the low Reynolds number condition (Run B) than the high Reynolds number condition (Figure 4.10).
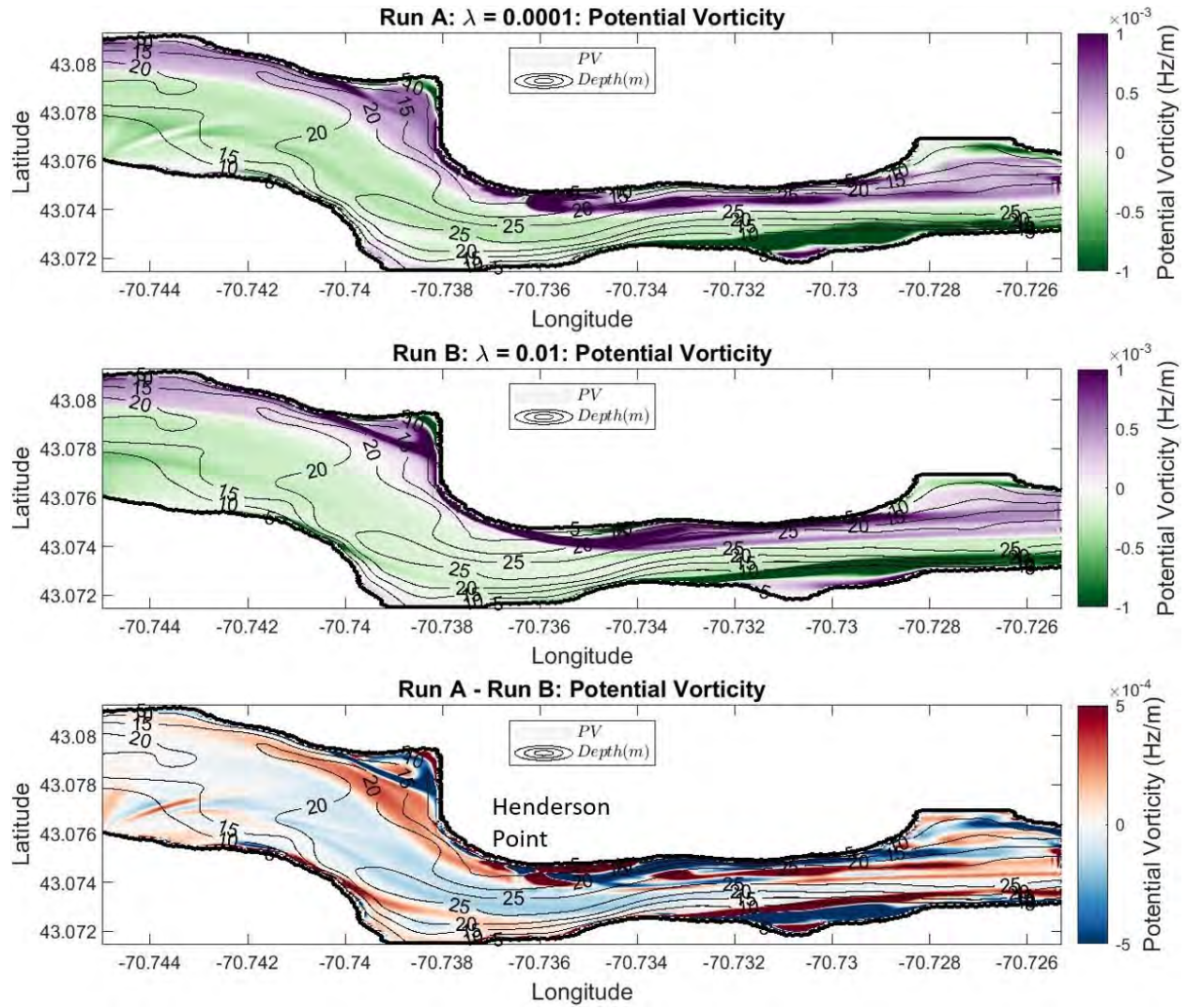
Figure 4.10. The potential vorticity for ebbing current Runs A (top) and B (middle) and the difference between the two (bottom). Depth contours are shown as black lines and labeled. The potential vorticity is calculated using the depth-averaged mean velocities over the last hour of the model run.

4.5.2 Flooding Currents

Similar to the ebb flow case ADCP observations, the mean velocity on the flood current intensifies over the lateral shelf off of Henderson Point in both the high and low Reynolds number conditions, Run C ($Re = 462$, $\lambda = 10^{-4}$) and Run D ($Re = 6$, $\lambda = 10^{-2}$), respectively (Figure 4.11 and Figure 4.12). Over the shelf, the velocity increases by approximately 0.1 m/s in the high Reynolds run corresponding to an ~8% increase in the maximum speed, which is smaller than the velocity

87

difference experienced in the ebb flow case. Similar to the ebb flow case and Bowen (1969), the streamlines also converge under high Reynolds number conditions (Figure 4.13) with flooding currents.
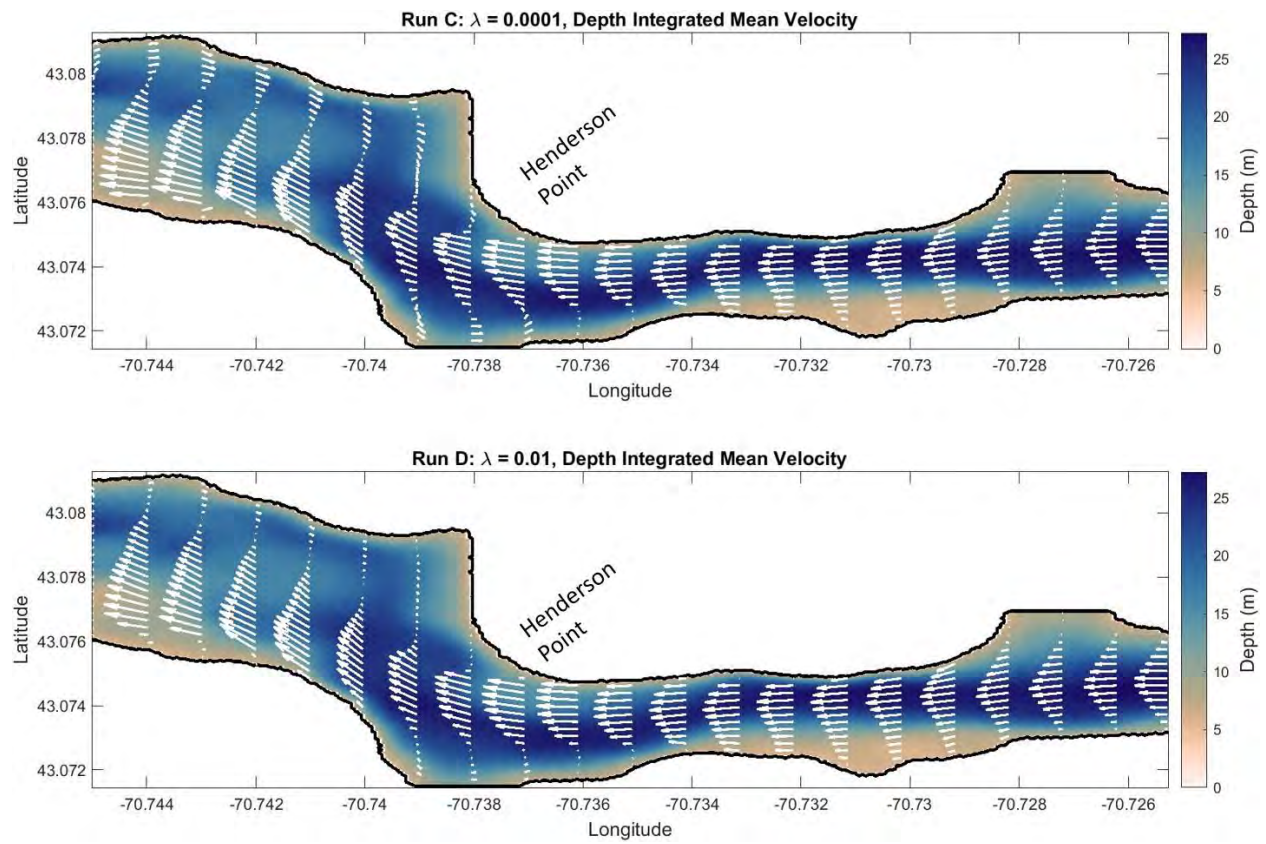
Figure 4.11. Depth integrated mean velocity over bathymetry for flooding current Runs C (top) and D (bottom). Vectors are scaled to 1.5 m/s. The mean is calculated over the last hour of the model run.
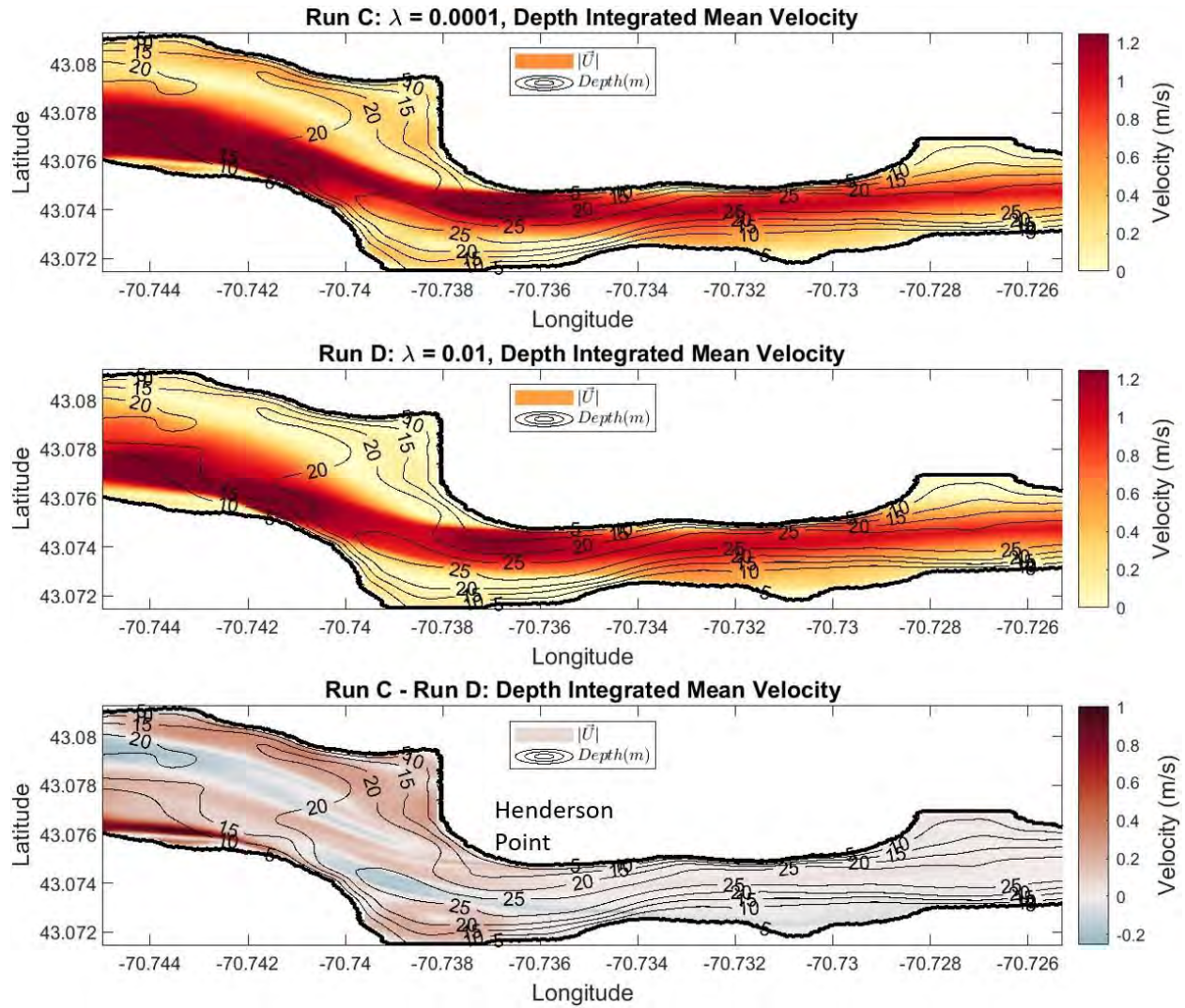
Figure 4.12. Depth integrated mean flood current magnitude for Runs C (top) and D (middle) and the difference between the two (bottom). Depth contours are shown as black lines and labeled. The mean is calculated over the last hour of the model run.

Overall, the flood flow results in slower mean velocities throughout the domain than the ebb flow for all Reynolds number cases (Table 4.2). This is likely due to the difference in area along the inflow and outflow boundaries leading to changes in velocity necessary to conserve volume. The flood case has an expansion of area on the outflow (western boundary) relative to the inflow (eastern boundary) leading to slower velocities and the ebb case has a constriction of outflow (eastern boundary) relative to the inflow (western boundary) leading to faster velocities.
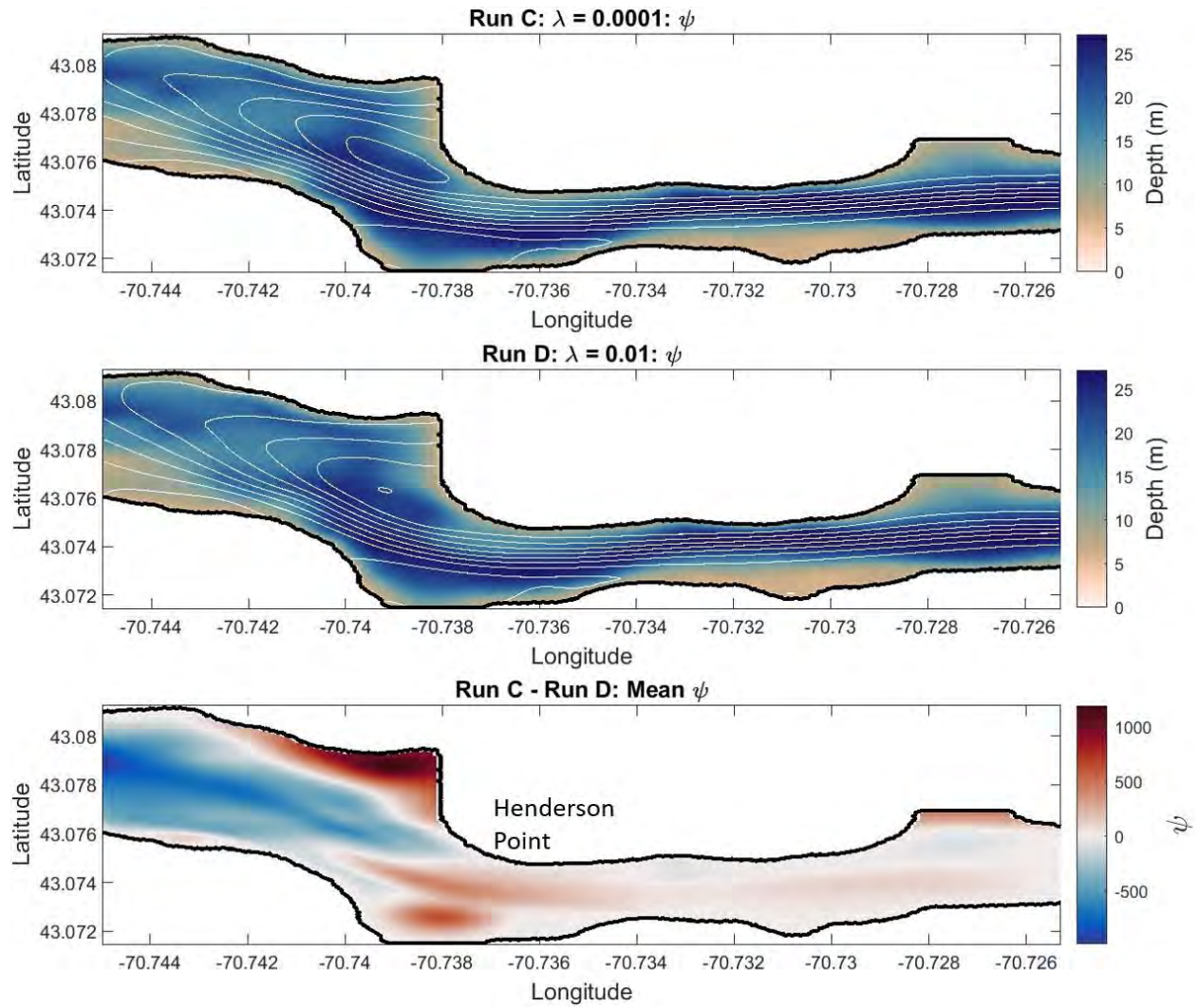
Figure 4.13. The stream function (white lines) over bathymetry for flooding current Runs C (top) and D (middle) and the difference between the two (bottom). The stream function is calculated using the depth-averaged, mean velocities over the last hour of the model run.

As the currents move beyond transect line T1 and the shelf off of Henderson Point, it is worth noting that the currents also intensify over the shallow area near the western boundary of the domain versus following the bathymetry contours and having stronger flow in the adjacent deeper channel (Figure 4.11), which is not observed on the ebb flow. Also seen in this area is a large recirculation cell only present on the flood with stronger return flow in the high Reynolds number condition (Run C) with weaker bottom frictional dampening (Figure 4.11).
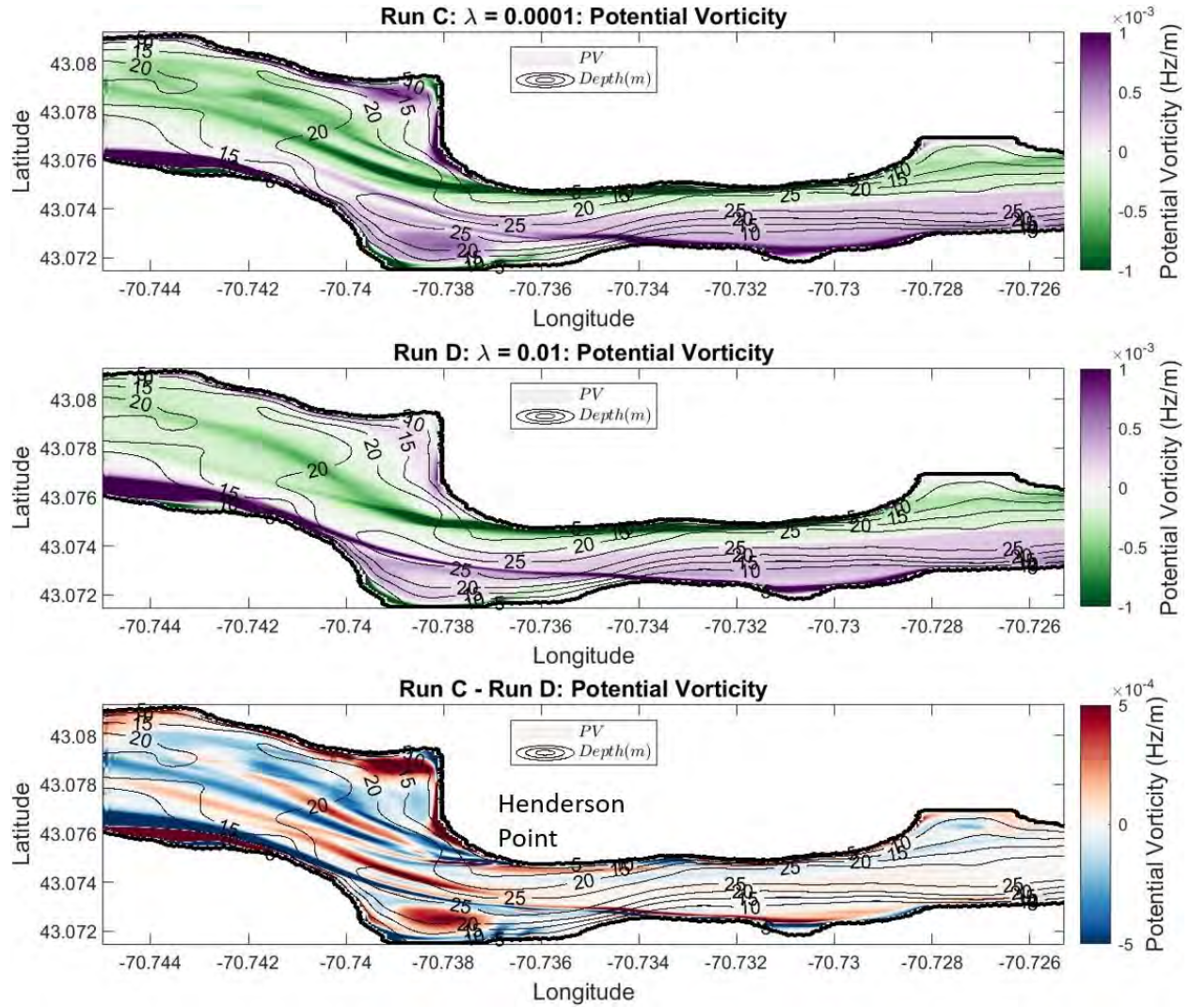
Figure 4.14. Potential vorticity for Runs C (top) and D (middle) with flooding flow and the difference between the two (bottom). Depth contours are shown as black lines and labeled. The potential vorticity is calculated using the depth-averaged, mean velocities over the last hour of the model run.

4.5.3 Cross-Channel Transects

For both the high and low Reynolds number cases and during ebbing and flooding flow, there is strong cross-channel shear in the along-channel velocity across all three transects (Figure 4.15), consistent with the ADCP observations (Figure 4.2). The model (Figure 4.16 and Figure 4.19) well reproduces both the depth-integrated (Figure 4.2) and depth-varying (Figure 4.3) currents observed along the transects. The model accurately shows faster currents near the surface but are slightly

attenuated near the bottom due to bottom friction. There is strong shear on either side of the channel at the ends of the three transects due to the no-slip condition and the associated lateral sidewall friction. Transects T2 and T3 show strong currents in the deeper channel for both flooding and ebbing flow and in the high and low Reynolds number conditions. Transect T1 is notable in that the flow is fastest over the shelf at Henderson Point relative to the adjacent deep channel, evident in both the depth averaged and 3-dimensional currents (Figure 4.15 - Figure 4.21).
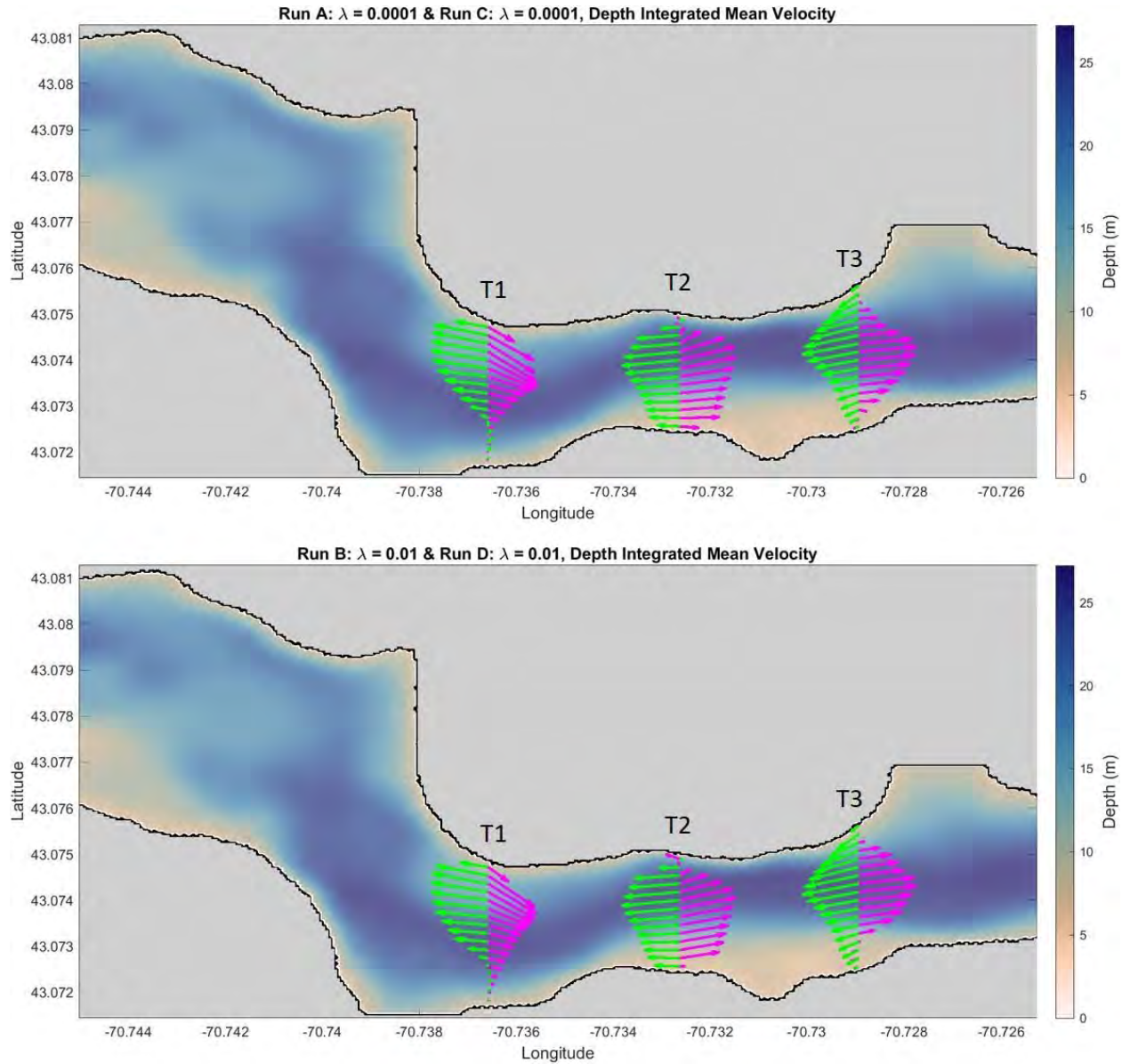
Figure 4.15. Depth averaged mean velocity across three transect lines (T1 – T3) for runs A and C (top) and B and D (bottom). The mean is calculated over the last hour of the model run.

4.5.4 Reynolds Shear Stress

The horizontal mixing of momentum is represented by the cross-channel Reynolds shear stress, S_{xy}, calculated across each transect line for the high Reynolds number condition on both the ebb (Run A; Figure 4.16 - Figure 4.18) and flood (Run C; Figure 4.19 - Figure 4.21). When S_{xy} is zero,

there is no mixing of momentum because the horizontal velocity components are in quadrature (i.e., out of phase by 90°). When S_{xy} is non-zero and there is a gradient in the Reynolds shear stress, momentum is transferred via horizontal mixing. The mixing increases in areas of strong horizontal current shear. The sign of the Reynolds shear stress is dependent on the sign of the gradient in the mean velocity cross-channel profile (Dodd and Thornton, 1990; Church et al., 1992) and indicates the direction of mixing of the along-channel flow laterally across the channel.

The highest S_{xy} occurs along transect line T1 for both the flood and ebb cases and specifically over the lateral shelf at Henderson Point (Figure 4.16 and Figure 4.19). S_{xy} is approximately two orders of magnitude smaller on the flood (Run C) compared to the ebb (Run A) along all three transects, likely due to the slower and steadier velocities seen on the flood. For ebbing currents (Run A), S_{xy} is negative along transect line T1 and T2 and positive along transect line T3 (Figure 4.16 - Figure 4.18) indicating that the direction of lateral momentum mixing changes when moving down river in the direction of the ebbing currents. For flooding currents (Run C), S_{xy} is negative over the lateral shelf at Henderson Point along transect line T1, however moving across the channel southwards, is near zero and then becomes slightly positive (Figure 4.19). S_{xy} is strongest and negative near the northern end of the channel along transect T2 with flooding currents, however changes sign twice becoming positive near mid-channel and negative again near the southern end of the channel, indicating that changes in direction of mixing occur across the channel (Figure 4.20). S_{xy} is positive and strongest in the shallow areas towards the northern and southern ends of transect line T3 for flooding currents (Figure 4.21). The change in sign of S_{xy} from positive along transect T3 to predominately negative along transect T1 indicates a change in direction of mixing as the flooding currents move upriver.
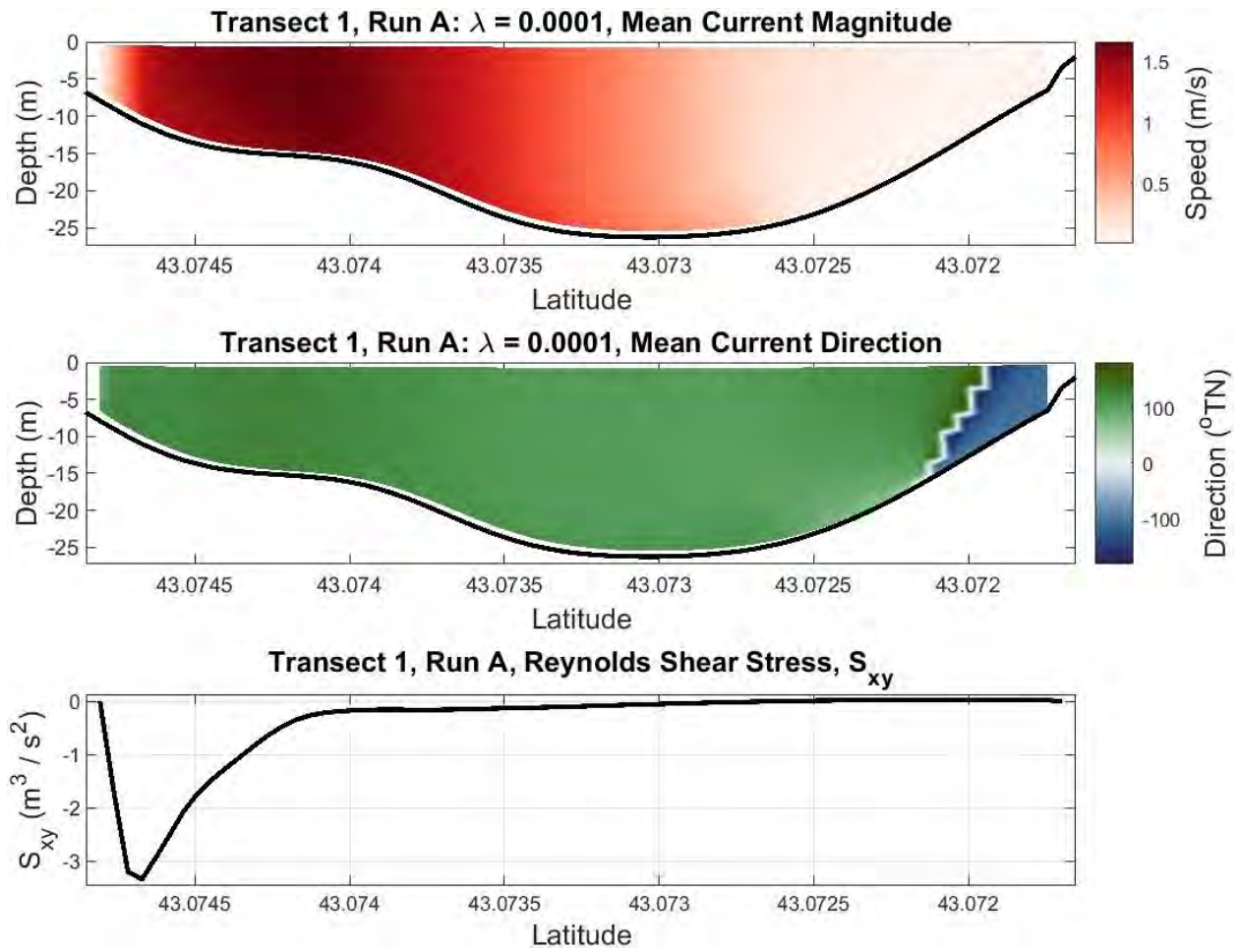
Figure 4.16. Run A (ebbing flow). Transect line T1. Mean current magnitude (top) and direction (middle) over the last hour of the model run. (Bottom) Reynolds shear stress, S_{xy}, using time averaged (last hour of the model run) depth-averaged (indicated by the overbar) unsteady horizontal velocities ($\overline{u}', \overline{v}'$).
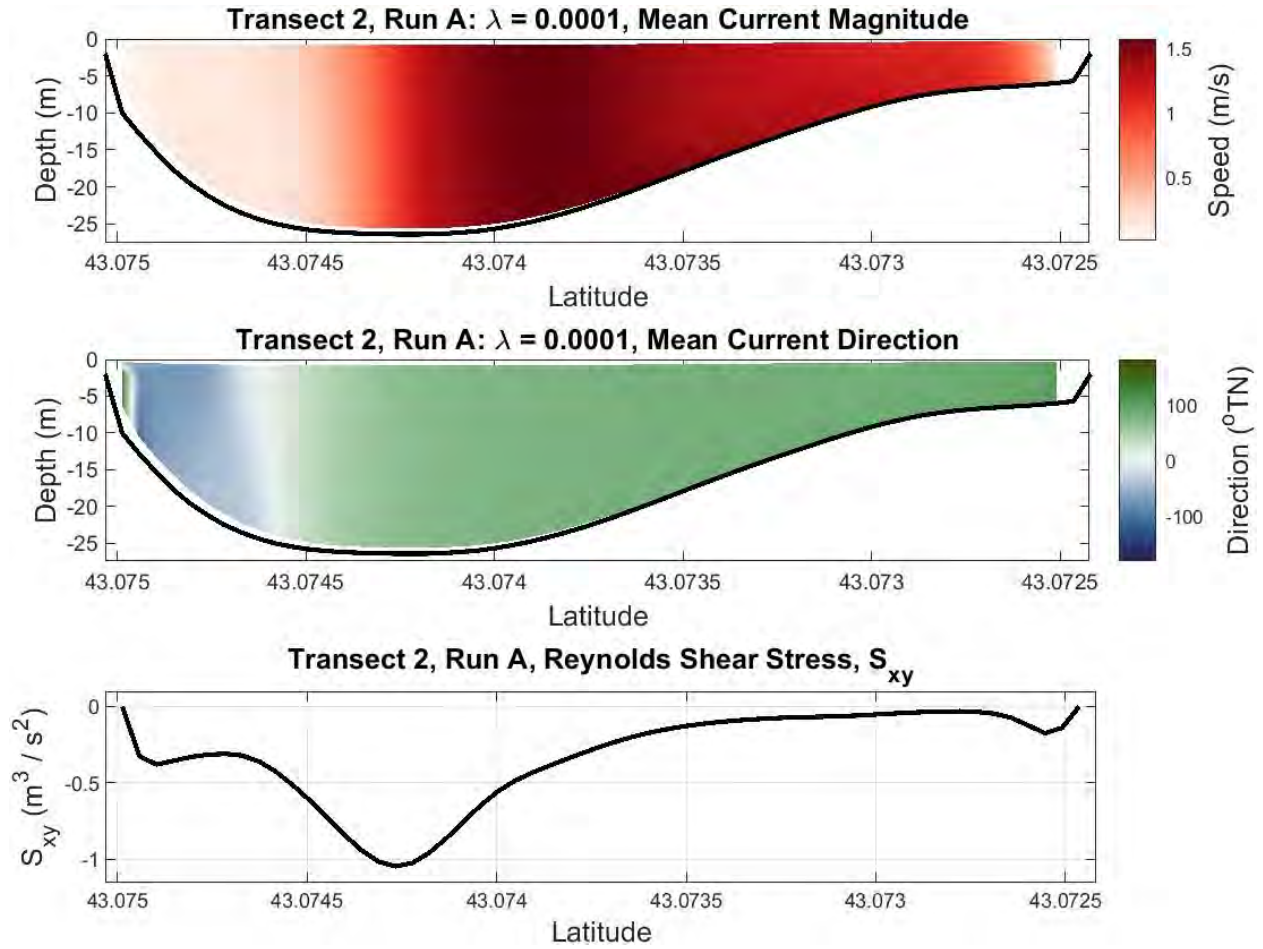
Figure 4.17. Run A (ebbing flow). Transect line T2. Mean current magnitude (top) and direction (middle) over the last hour of the model run. (Bottom) Reynolds shear stress, S_{xy}, using time averaged (last hour of the model run) depth-averaged (indicated by the overbar) unsteady horizontal velocities ($\overline{u}', \overline{v}'$).
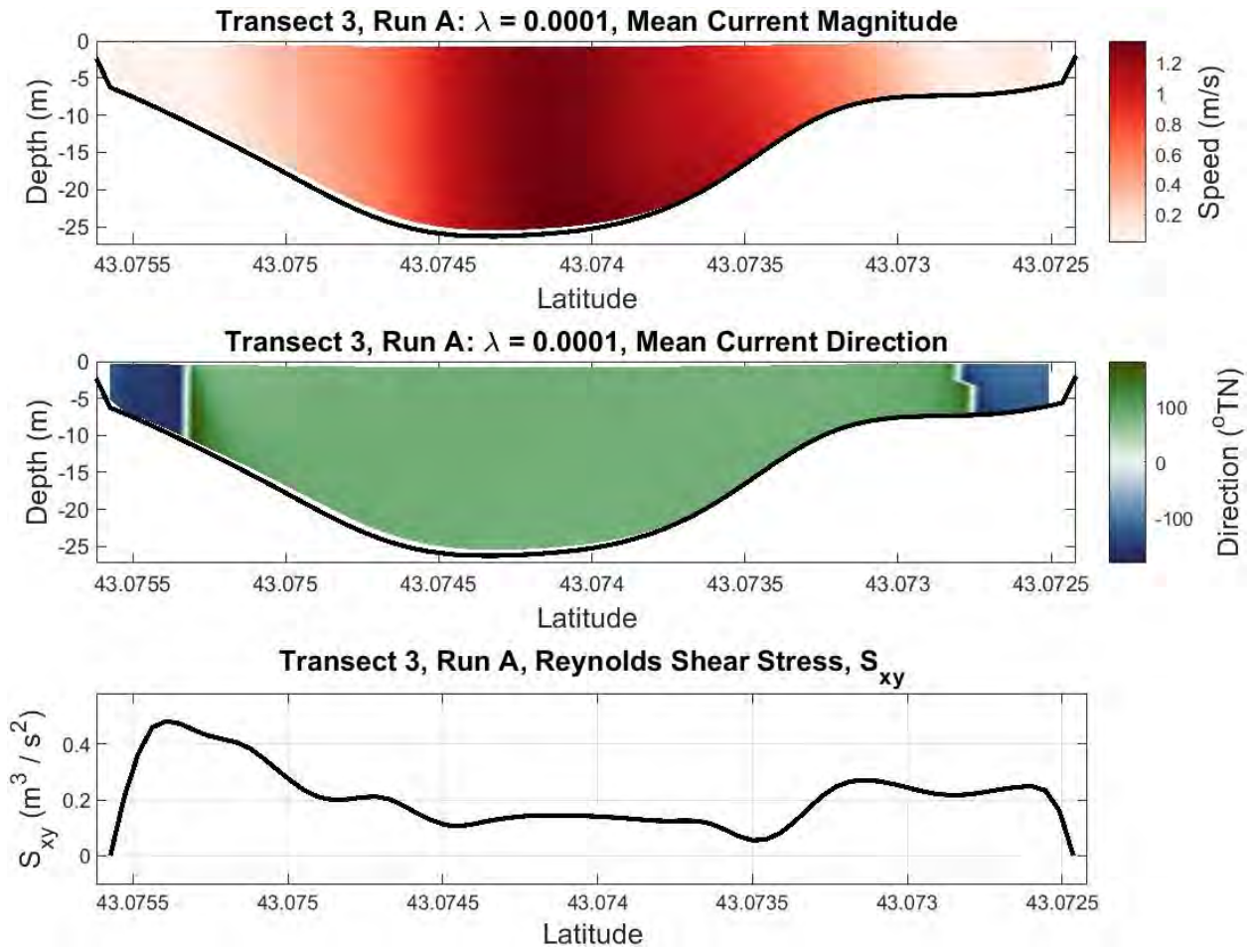
Figure 4.18. Run A (ebbing flow). Transect line T3. Mean current magnitude (top) and direction (middle) over the last hour of the model run. (Bottom) Reynolds shear stress, S_{xy}, using time averaged (last hour of the model run) depth-averaged (indicated by the overbar) unsteady horizontal velocities ($\overline{u}', \overline{v}'$).
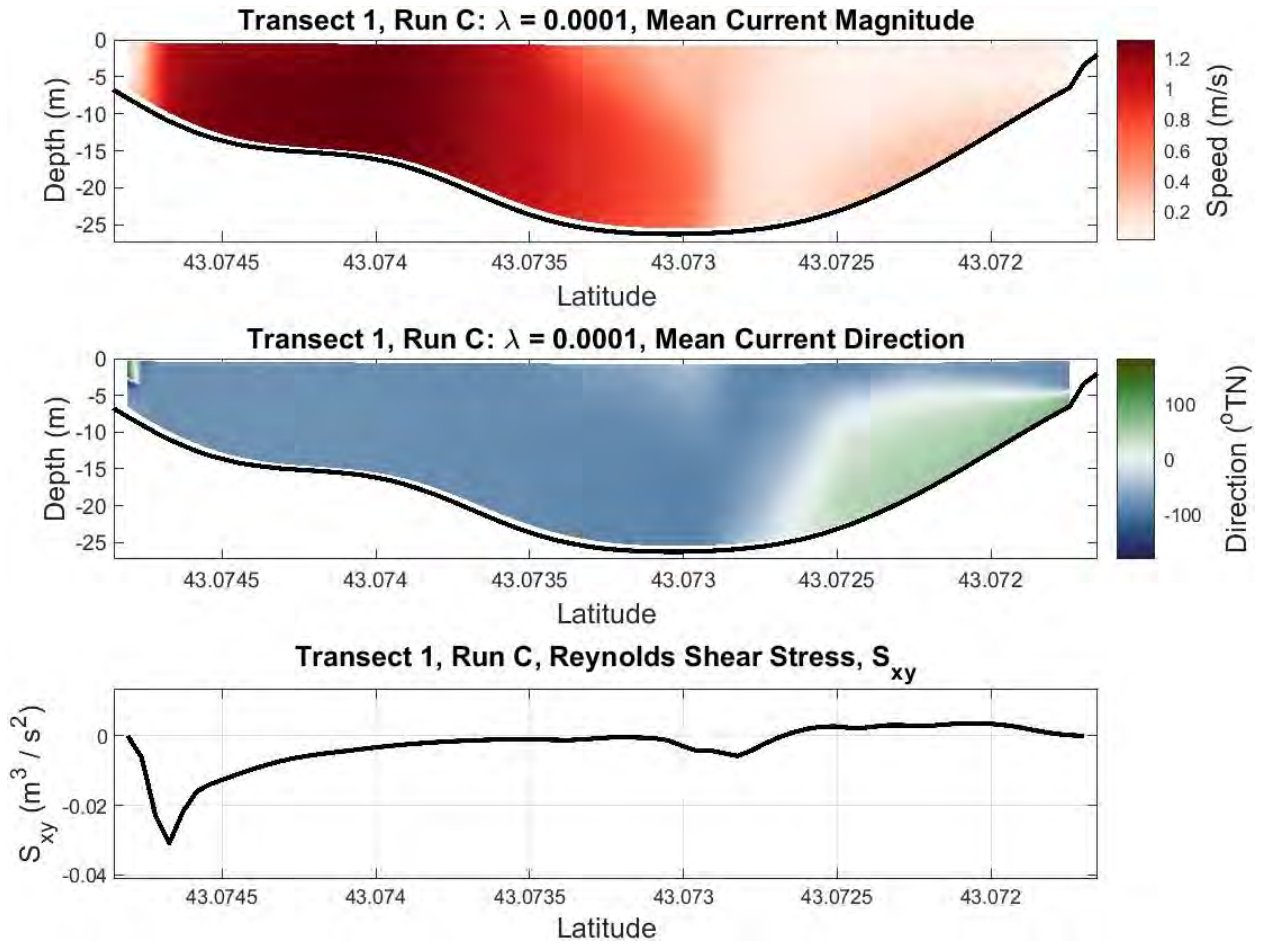
Figure 4.19. Run C (flooding flow). Transect line T1. Mean current magnitude (top) and direction (middle) over the last hour of the model run. (Bottom) Reynolds shear stress, S_{xy}, using time averaged (last hour of the model run) depth-averaged (indicated by the overbar) unsteady horizontal turbulence velocities ($\overline{u}', \overline{v}'$).
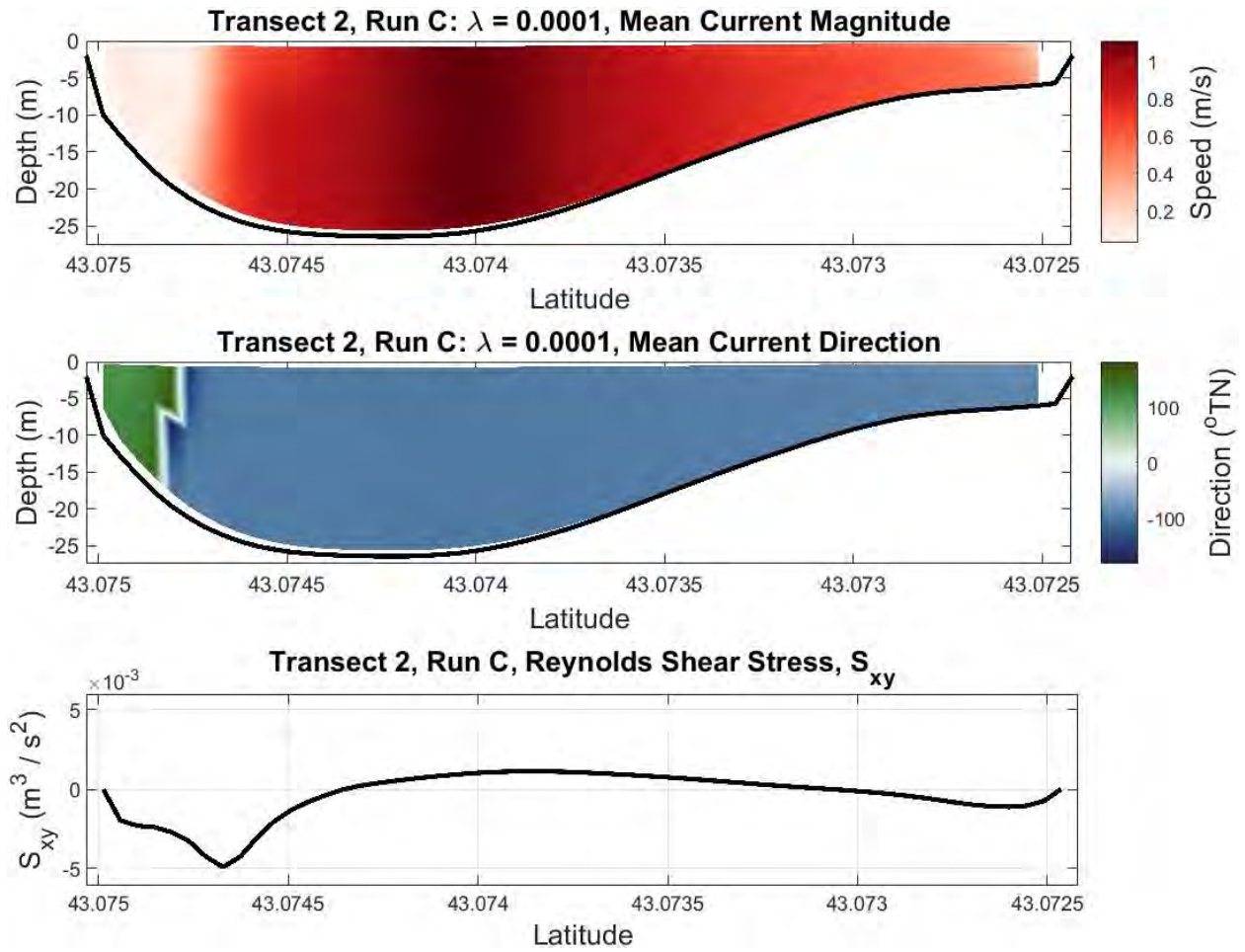
Figure 4.20. Run C (flooding flow). Transect line T2. Mean current magnitude (top) and direction (middle) over the last hour of the model run. (Bottom) Reynolds shear stress, S_{xy}, using time averaged (last hour of the model run) depth-averaged (indicated by the overbar) unsteady horizontal velocities ($\overline{u}', \overline{v}'$).
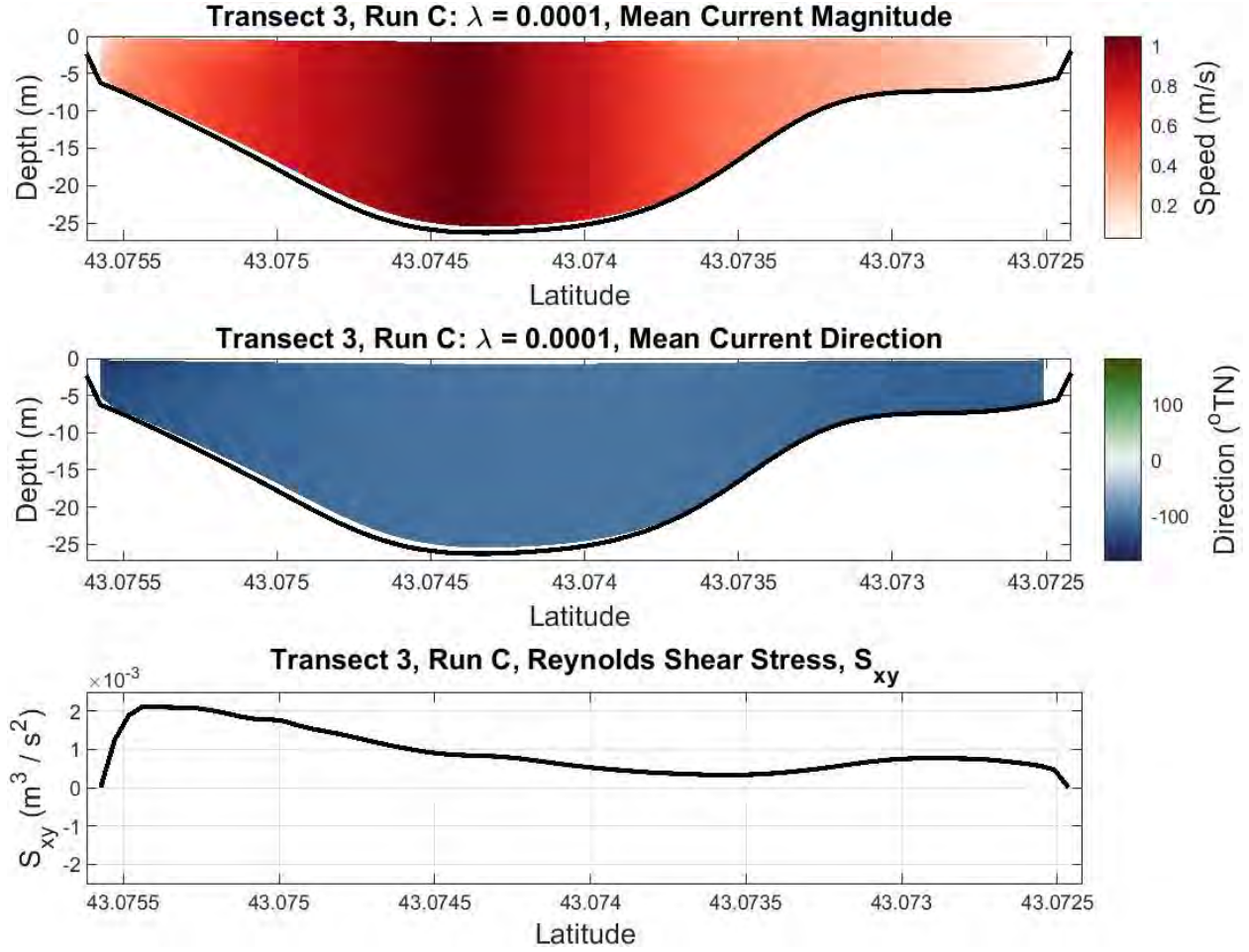
Figure 4.21. Run C (flooding flow). Transect line T3. Mean current magnitude (top) and direction (middle) over the last hour of the model run. (Bottom) Reynolds shear stress, S_{xy}, using time averaged (last hour of the model run) depth-averaged (indicated by the overbar) unsteady horizontal velocities ($\overline{u}', \overline{v}'$).

4.6 Discussion

Here, we investigate the forcing mechanisms driving an intensification of the mean tidal current through a narrow estuarine channel over a lateral shelf off Henderson Point in the Piscataqua River observed by cross-channel ADCP transects. Although it is expected that faster currents flow through the deeper channel where the dampening effect from bottom friction is weaker, the velocity is observed to be strongest on the shallow shelf during both the ebb and flood currents. Numerical simulations using ROMS were conducted to better understand the flow dynamics and

100

forcing mechanisms driving the velocity intensification over the shelf. The numerical results qualitatively well reproduced the observations of both the depth averaged and vertically varying horizontal currents observed along three cross-channel transect lines south of Seavey Island.

The velocity intensification in the tidal current through the bounded channel is analogous to rip currents in the nearshore studied by Bowen (1969). Numerical solutions in Bowen (1969) show that under high Reynolds number conditions a narrowing of streamlines and strengthening of the seaward flow (rip currents) occurs. Similar to Bowen (1969), we ignore the Coriolis force and investigate the potential vorticity balance where the relative vorticity dominates and the flow is inertial. Our results are consistent with Bowen (1969) in that under high Reynolds number conditions (low bottom friction and eddy viscosity), streamlines cross bathymetric contours and converge leading to intensification of velocities over the lateral shelf at Henderson Point during both ebb and flood currents. Under low Reynolds number conditions, the bottom friction dampens the flow.

The potential vorticity balance is used to better understand the fluid dynamics and forcing mechanisms. The strong shear in along-channel velocity drives a strong cross-channel gradient in potential vorticity throughout the channel, and especially over the shelf at Henderson Point, with both flood and ebb currents (Figure 4.10 and Figure 4.14). The positive (negative) potential vorticity seen over the shelf on the ebb (flood) flow leads to cyclonic (anticyclonic) vorticity that contribute to circulation up onto the shelf. Although the potential vorticity is not conserved here due to the inclusion of bottom friction and eddy viscosity, those terms are considered small relative to the inertial terms under high Reynolds number conditions. This is seen by comparing the inertial time scale of motion, $\frac{L}{U}$, with the frictional spin down time, $\frac{H}{\lambda}$, assuming the eddy viscosity term is negligible, so that $\frac{A_H}{L^2} \ll \frac{H}{\lambda}$. To maintain numerical stability, A_H was set to 0.1 m^2/s, however the

eddy viscosity coefficient may be smaller (e.g. ~0.01 m^2/s) in realistic estuarine conditions. Using characteristic scales of motion over the Henderson shelf that were similarly used in calculating the Reynolds number, the inertial time scale (200 s or approx. 3 min) is much faster than the time it would take bottom friction to spin down the currents (1.2x10^5 s or > 33 hr) in high Reynolds number conditions ($\lambda = 10^{-4}$) or even in moderate friction conditions ($\lambda = 10^{-3}$; >3 hr). Therefore, we can assume the potential vorticity is approximately conserved, $\frac{D}{Dt}\left(\frac{\xi}{h}\right) \approx 0$, in which case the relative vorticity must weaken when the depth shoals over Henderson Point.

While the potential vorticity is approximately conserved and contributes to changes in the horizontal shear structure, the volume is also conserved and plays a role in the velocity intensification observed over the shelf. Since the flow is predominately inertial, supported by the low Froude number (<1) and large Reynolds number, the velocity will increase over the shallow shelf at Henderson Point to conserve volume.

On the flood tide, the currents also intensify over the shallow area near the western boundary of the domain versus following the bathymetry contours and having stronger flow in the adjacent deeper channel (Figure 4.11). This is consistent with similar forcing mechanisms as those causing the intensification of velocity over the shelf at Henderson Point and therefore, may suggest the forcing may be more generally applied in other inlets and channels with comparable bathymetric and topographic features with similar scales of motion leading to velocity intensifications. However, there are no observations available to verify the model results and therefore will not be further discussed. It is worth noting the intensification was not observed with ebbing currents, likely due to the proximity to the western inflow that has a clamped boundary condition and therefore, the flow may not have enough space to adjust to the bathymetry before reaching this shoal.

This velocity intensification over the shelf at Henderson Point leads to stronger cross-channel shear that can support unstable motions (Appendix E: Unstable Motions in the Piscataqua River). The unstable motions cause lateral mixing of momentum, the magnitude of which is calculated through the Reynolds shear stress, S_{xy}. Prior studies have found horizontal mixing of momentum to smooth the cross-channel velocity structure and diffuse the velocity gradients (Dodd and Thornton, 1990). The expected direction and magnitude of mixing of momentum is dependent on the velocity shear structure and inversely proportional to the potential vorticity gradient (Dodd and Thornton, 1990; Chapter II). Momentum is horizontally mixed across the channel from areas with fast velocities towards the areas of weaker velocities while transferring energy from the mean tidal current to the turbulent flow. The magnitude of mixing is strongest in areas of high current shear, as experienced over the shelf at Henderson Point during both the ebb and flood currents (Figure 4.16 and Figure 4.19).

Intensification of velocity (up to approx. 13% increase relative to the max speed) over the lateral shelf at Henderson Point and the consequential unstable motions that lead to horizontal mixing of momentum can have significant impacts on safe and economical navigation (Chen et al., 2013), tidal current energy resource assessments that depend on the velocity to the third power (Lalander et al., 2013), the fate and transport of organic and inorganic matter, and estuarine dynamics including salt transport.

4.7 Conclusions

Spatial variability of the tidal currents are analyzed numerically using ROMS to better understand the forcing mechanisms driving the cross-channel current structure over a lateral shelf at Henderson Point in the Piscataqua River. Results improve understanding of tidal current dynamics

and horizontal mixing of momentum in inlets and estuaries across narrow channels with variable bathymetry.

Our results are analogous to and consistent with Bowen (1969), in that an intensification of velocity (convergence of streamlines) over the lateral shelf at Henderson Point resulted from the potential vorticity balance including frictional terms during both quasi-steady (flood and ebb tidal) currents. When bottom friction and eddy viscosity are small, the flow is highly inertial (high Reynolds number conditions) leading to streamlines crossing bathymetric contours (horizontal cross-river circulation) and increased velocities over the shallow lateral shelf. Given the cross-channel structure of the velocity, the water is pushed up onto the shelf by the potential vorticity. Due to the shallower depth, the velocities increase due to conservation of volume, which leads to even stronger horizontal shear in the mean along-channel tidal currents.

The consequential unstable motions lead to horizontal mixing of momentum, the magnitude of which is calculated through the Reynolds shear stress, S_{xy}. The mixing is largest in the area with the strongest shear, which occurs over the lateral shelf at Henderson Point where currents are intensified. The mixing is expected to modify the cross-channel velocity structure and smooth out the gradients in shear of the mean along-channel tidal current. The velocity intensification over the shelf along with the unstable motions and mixing of momentum can have impacts on navigation, tidal current energy assessment, and estuarine dynamics, including the fate and transport of organic and inorganic substances.

CHAPTER 5

5   CONCLUSIONS

This research aims to better understand the spatial and temporal variability of tidal currents, primarily the high frequency variability about the mean, flowing through narrow inlets and/or bounded estuarine channels. Chapter 2 is a theoretical analytical analysis of instabilities of tidal currents. Observations were collected in the Hampton-Seabrook Inlet and analyzed in Chapter 3 to determine the presence of unstable motions. Chapter 4 uses a numerical hydrodynamic, 3-dimensional model to study the flow and analyze the velocity intensification over a lateral shelf in the Piscataqua River.

Chapter 2 describes the general dispersion equation of barotropic instabilities of tidal currents analytically solved over simple bathymetry through idealized and variable channel geometries. The solution is third-order and depends on the wavenumber, maximum current magnitude, horizontal shear of the current, cross-inlet geometry and bathymetry, and a linear friction coefficient. The cross-channel velocity, bathymetry, and geometry can be altered to approximate typical natural inlet geometries allowing for a range of scenarios to be examined. The resulting dominant wavelengths are $O(10^2$ m), periods are $O(10^2$ - 10^3 s), and growth rates of the fastest growing unstable modes are $O(10^{-3}$ - 10^{-2} s^{-1}) with phase speeds approximately one third of the maximum velocity, consistent with instabilities of longshore currents studied in the nearshore (Bowen and Holman, 1989; Dodd and Thornton, 1990).

This work expands upon Bowen and Holman (1989) solution for nearshore longshore currents in that the bathymetry is variable (piecewise linear) and includes the presence or absence of lateral shelves, the flow is bounded on either side, there are two extremums in the potential vorticity (one of the requirements for the growth of unstable modes), and a linear bottom friction

is included. Bottom friction suppresses the unstable motions leading to slower initial growth rates and a reduced range of unstable wavenumbers. Faster growing modes with a larger range of unstable wavenumbers and stronger horizontal mixing (represented by the cross-channel Reynolds shear stress) occur under stronger shear conditions and cross-channel bathymetry with wide, deep shelves. Horizontal mixing acts to smooth the initial velocity cross-channel structure and stronger mixing by the instabilities occurs in the areas of higher lateral current shear. These results suggest that tidal currents in inlets will produce unstable modes that can mix momentum laterally, impacting transport of particulate and dissolved organic and inorganic matter through the inlet.

In Chapter 3, observations were collected in the Hampton-Seabrook Inlet to determine the presence of instabilities of tidal currents consistent with the general solution found in Chapter 2. To estimate the wavenumbers of shear instabilities, a spatially-lagged array consisting of seven sensors measuring tri-directional currents and pressure were deployed for one week during the spring tide in May 2021. Using iterative maximum likelihood estimators, wavenumber-frequency spectra are estimated during 3-4 hour time periods with approximately steady currents on both the flood and ebb tides. Dominant wavenumbers ($\pm$ 0.002 - 0.02 m^{-1}) of the low frequency motions (0.0006 - 0.01 s^{-1}) with corresponding wavelengths ($\pm$ 314.2 – 3141.6 m) and periods (628.3 – 10472 s) are resolved and consistent with motions determined from the barotropic linear stability analysis described in Chapter 2. The instabilities are directed into the inlet on flood tides and out of the inlet on the ebbs, consistent with the expected generation and propagation of unstable modes produced by the cross-channel shear. The normalized velocity-to-pressure variance ratio at each station shows that the infragravity band is dominated by rigid-lid-like motions ($R \gg 1$) during both the flood and ebb tide. The lack of breaking wave group modulations within the inlet and the presence of the seaward propagating instabilities on the ebb flow indicate that the presence of the

instabilities can be attributed to the shear of the tidal current. These results are consistent with instabilities of longshore currents observed in the nearshore (Oltman-Shay et al., 1989) and the resulting high frequency variability of the currents can lead to the horizontal mixing of momentum across the inlet impacting estuarine dynamics.

An intensification of velocity over a lateral shelf off Henderson Point in the Piscataqua River was observed by cross-river transects of a downward-looking vessel-mounted ADCP in 2015 during both the flood and ebb on the spring tide. In Chapter 4, a numerical hydrodynamic model (ROMS) was used to model the flow and better understand the forcing mechanisms driving intensification of velocity over the shallow shelf versus in the deeper adjacent channel, where bottom friction is expected to have less of a dampening effect on the depth-averaged currents. Analogous to prior work examining the intensification of rip currents in the nearshore (Bowen, 1969), the potential vorticity balance is used to help explain and understand the physical dynamics. Results show that the along-channel flow is intensified (convergence of streamlines) over the later shelf under high Reynolds number conditions, where the inertial forces dominate over the frictional and viscous forces, during both quasi-steady flooding and ebbing currents. The potential vorticity is approximately conserved since the inertial time scales are much faster than the frictional spin down time. Given the cross-channel structure of the velocity, the water is circulated up onto the shelf by the potential vorticity. Due to the shallower depth, the velocities increase due to conservation of volume, which leads to even stronger horizontal shear in the mean along-channel tidal currents. The intensification of tidal currents over shallow regions of a bounded channel leads to spatial variability in cross-channel current velocity structure that can support unstable motions that cause horizontal mixing of momentum that act to smooth the lateral shear in mean flow.

This work aims to help researchers better understand the spatial and temporal high frequency variability of mean tidal currents flowing through narrow estuarine channels. This variability can lead to horizontal mixing of momentum across the channel and significantly impact estuarine dynamics.

5.1 Applications to NOAA

NOAA's National Ocean Service's (NOS) Center for Operational Products and Services (CO-OPS) routinely measures mean (calculated in 6 minute intervals) tidal currents along the U.S. coasts and estuaries, from which predictions of flood and ebb current magnitudes and phases over spring-neap tidal cycles are calculated. The users of these products include mariners, as well as scientists and engineers interested in numerical model development and verification. The location of current meter deployments within a given estuary as part of either NOAA's PORTS (Physical Oceanographic Real-Time System) or NCOP (National Currents Observation Program) surveys are determined from a variety of factors including proximity to the navigational channel, historical predictions of max current speeds, preexisting numerical model simulations of the area, and reconnaissance data of the site. Typically in NCOP surveys, sensors may be spaced widely apart (up to several miles) in order to span the estuary leaving large spatial gaps in the tidal current structure. Although these data are invaluable in representing expected tidal current velocities and phases experienced by mariners, they do not consider the high frequency variability in the flow relative to the 6-min mean, nor the horizontal spatial variability resulting from the cross-channel shear in the mean along-channel current since these sensors are typically profiling vertically through the water column at a single location. This work highlights the importance of understanding the temporal and spatial variability of mean currents and by using numerical models

and ADCP transects collected across channels, NOAA can better determine the optimal sensor locations for future PORTS and NCOP current meter stations in areas where the max tidal current is experienced.

Observations of tidal currents are critical in developing and validating hydrodynamic models enabling more accurate and reliable output and products. NOAA's NOS Coast Survey Development Lab (CSDL) and CO-OPS jointly develops, implements, and maintains several Operational Nowcast and Forecast Hydrodynamic Model Systems (OFS) throughout the coastal U.S. that provide nowcasts and short-term forecasts (up to 72 hr.) of a variety of oceanographic and meteorological products, including currents (Vincent et al., 2003). These models help fill spatial gaps in real-time tidal current observations, which are both expensive and can be difficult to maintain. Fine grid resolution is necessary to accurately resolve the spatial structure of the mean tidal current flow throughout the estuary, especially through narrow inlets where current shear is strong and navigation is hazardous. As NOAA's OFS models continue to increase resolution in inlets and estuaries, especially in model domains expanding further up rivers, ADCP transects across estuarine channels and temporary ADCP deployments will be critical in validating the models and ensuring accurate nowcast and forecasts of the mean current, especially in areas with high temporal and/or spatial variability.

5.2 Future Work

There are a variety of considerations for future work in investigating the temporal and spatial variability of mean tidal currents in estuaries and tidal inlets with narrow channels. In Chapter 2, the horizontal eddy viscosity coefficient was neglected in the analytical solution, which could be included in future analysis for completion. The inclusion of this term is expected to dampen the

growth rates causing less energetic, longer along-channel motions due to a decrease in the high-wavenumber oscillations, and slightly slower phase speeds based on results found by Falqués and Iranzo (1994) and Özkan-Haller and Kirby (1999).

In Chapter 3, the array deployments were limited by the federally maintained navigational channel and all current meters were deployed outside of the channel along the southern side of the inlet to help ensure safety of vessels and the equipment. However, in addition to the spatially lagged array along the southern side of the inlet, it would have been helpful to also have a cross-channel array and/or a spatially lagged array along the northern side of the inlet. The cross-channel array would provide insight into the spatial variability of the tidal currents while providing time series of velocity filling in temporal gaps between collecting data on ADCP transects. The spatially-lagged array along the northern side of the inlet would be used to observe instabilities due to the shear along the northern side and be compared with the scales of motion generated from the shear along the southern side of the inlet on both the flood and ebb tide. This would be especially beneficial if there is asymmetry in the location of the max currents across the channel between the flood and ebb tidal currents.

In Chapter 4, the model used clamped inflow conditions based on expected velocity structure at the boundaries. Ideally, the smaller domain model would be nested into a larger domain model and the forcing conditions would be based on the tidally induced pressure gradient resolved in the larger domain model. The model domain could also be expanded in order to analyze the shallow area near the western boundary where currents were observed to have intensified on the flood tide to determine if this is experienced on the ebb flow given ample space away from the inflow boundary for the currents to adjust to the bathymetry and topography.

REFERENCES

Baquerizo, A., Caballeria, M., Losada, M. A., & Falqués, A. (2001). Frontshear and backshear instabilities of the mean longshore current. *Journal of Geophysical Research: Oceans*, *106*(C8), 16997–17011. https://doi.org/10.1029/2001JC900004

Blanckaert, K., & De Vriend, H. J. (2004). Secondary flow in sharp open-channel bends. *Journal of Fluid Mechanics*, *498*, 353–380. https://doi.org/10.1017/S0022112003006979

Blondeaux, P., & Seminara, G. (1985). A unified bar–bend theory of river meanders. *Journal of Fluid Mechanics*, *157*, 449–470. https://doi.org/10.1017/S0022112085002440

Bourgault, D., Saucier, F. J., & Lin, C. A. (2001). Shear instability in the St. Lawrence Estuary, Canada: A comparison of fine-scale observations and estuarine circulation model results. *Journal of Geophysical Research: Oceans*, *106*(C5), 9393–9409. https://doi.org/10.1029/2000JC900165

Bowden, K. F. (1965). Horizontal mixing in the sea due to a shearing current. *Journal of Fluid Mechanics*, *21*(01), 83. https://doi.org/10.1017/S0022112065000058

Bowen, A. J. (1969). Rip currents: 1. Theoretical investigations. *Journal of Geophysical Research*, *74*(23), 5467–5478. https://doi.org/10.1029/JC074i023p05467

Bowen, A. J., & Holman, R. A. (1989). Shear instabilities of the mean longshore current: 1. Theory. *Journal of Geophysical Research*, *94*(C12), 18023. https://doi.org/10.1029/JC094iC12p18023

Callander, R. A. (1969). Instability and river channels. *Journal of Fluid Mechanics*, *36*(03), 465. https://doi.org/10.1017/S0022112069001765

Chen, C., Shiotani, S., & Sasa, K. (2013). Numerical ship navigation based on weather and ocean simulation. *Ocean Engineering*, *69*, 44–53. https://doi.org/10.1016/j.oceaneng.2013.05.019

Church, J. C., Thornton, E. B., & Oltman-Shay, J. (1992). *Mixing by Shear Instabilities of the Longshore Current*. Coastal Engineering.

Cook, S., & Lippmann, T. (2017). Tidal Energy Dissipation in Three Tidal Estuarine Environments. *Coastal Dynamics*, *267*, 11.

Davis, R. E., & Regier, L. A. (1977). Methods for estimating directional wave spectra from multi-element arrays. *Journal of Marine Research*, *35*(03–02), 26.

Dodd, N., & Falqués, A. (1996). A note on spatial modes in longshore current shear instabilities. *Journal of Geophysical Research: Oceans*, *101*(C10), 22715–22726. https://doi.org/10.1029/96JC01986

Dodd, N., Iranzo, V., & Reniers, A. (2000). Shear instabilities of wave-driven alongshore currents. *Reviews of Geophysics*, *38*(4), 437–463. https://doi.org/10.1029/1999RG000067

Dodd, N., Oltman-Shay, J., & Thornton, E. B. (1992). Shear Instabilities in the Longshore Current: A Comparison of Observation and Theory. *Journal of Physical Oceanography*, *22*, 62–82.

Dodd, N., & Thornton, E. B. (1990). Growth and Energetics of Shear Waves in the Nearshore. *Journal of Geophysical Research*, *95*(C9), 16075. https://doi.org/10.1029/JC095iC09p16075

Falqués, A., & Iranzo, V. (1994). Numerical simulation of vorticity waves in the nearshore. *Journal of Geophysical Research*, *99*(C1), 825. https://doi.org/10.1029/93JC02214

Gaster, M. (1962). A note on the relation between temporally-increasing and spatially-increasing disturbances in hydrodynamic stability. *Journal of Fluid Mechanics*, *14*(2), 222–224. https://doi.org/10.1017/S0022112062001184

Geiman, J. D., & Kirby, J. T. (2013). Unforced Oscillation of Rip-Current Vortex Cells. *Journal of Physical Oceanography*, *43*(3), 477–497. https://doi.org/10.1175/JPO-D-11-0164.1

Geyer, W. R., Lavery, A. C., Scully, M. E., & Trowbridge, J. H. (2010). Mixing by shear instability at high Reynolds number. *Geophysical Research Letters*, *37*(22), n/a-n/a. https://doi.org/10.1029/2010GL045272

Geyer, W. R., & MacCready, P. (2014). The Estuarine Circulation. *Annual Review of Fluid Mechanics*, *46*(1), 175–197. https://doi.org/10.1146/annurev-fluid-010313-141302

Geyer, W. R., & Smith, J. D. (1987). Shear Instability in a Highly Stratified Estuary. *Journal of Physical Oceanography*, *17*, 1668–1679.

Geyer, W. R., Trowbridge, J. H., & Bowen, M. M. (2000). The Dynamics of a Partially Mixed Estuary. *Journal of Physical Oceanography*, *30*(8), 2035–2048. https://doi.org/10.1175/1520-0485(2000)030<2035:TDOAPM>2.0.CO;2

Gunawan, B., Neary, V., & Colby, J. (2014). Tidal energy site resource assessment in the East River tidal strait, near Roosevelt Island, New York, New York. *Renewable Energy*, *71*, 509–517. http://dx.doi.org/10.1016/j.renene.2014.06.002

Gunawan, B., Neary, V., Mortensen, J., & Roberts, J. (2017). *Assessing and Testing Hydrokinetic Turbine Performance and Effects on Open Channel Hydrodynamics: An Irrigation Canal Case Study.* (SAND--2017-4925R, 1367421, 653168; p. SAND--2017-4925R, 1367421, 653168). U.S. Department of Energy. https://doi.org/10.2172/1367421

Haller, M. C., & Dalrymple, R. A. (2001). Rip current instabilities. *Journal of Fluid Mechanics*, *433*, 161–192. https://doi.org/10.1017/S0022112000003414

Halse, K. H. (1997). *On vortex shedding and prediction of vortex-induced vibrations of circular cylinders*. Norwegian University of Science and Technology.

Howd, P. A., Bowen, A. J., & Holman, R. A. (1992). Edge Waves in the Presence of Strong Longshore Currents. *Journal of Geophysical Research*, *97*(C7), 11357–11371. https://doi.org/10.1029/92JC00858

Huntley, D. A., Guza, R. T., & Thornton, E. B. (1981). Field Observations of Surf Beat: 1. Progressive Edge Waves. *Journal of Geophysical Research*, *86*(C7), 6451–6466.

Jones, S. H. (2000). *A Technical Characterization of Estuarine and Coastal New Hampshire* (294; PREP Reports & Publications, p. 280). University of New Hampshire.

Lalander, E., Grabbe, M., & Leijon, M. (2013). On the velocity distribution for hydro-kinetic energy conversion from tidal currents and rivers. *Journal of Renewable and Sustainable Energy*, *5*(2), 023115. https://doi.org/10.1063/1.4795398

Lanzoni, S., & Seminara, G. (2006). On the nature of meander instability. *Journal of Geophysical Research*, *111*(F4), F04006. https://doi.org/10.1029/2005JF000416

Lippmann, T. C., Herbers, T. H. C., & Thornton, E. B. (1999). Gravity and Shear Wave Contributions to Nearshore Infragravity Motions. *Journal of Physical Oceanography*, *29*(2), 231–239. https://doi.org/10.1175/1520-0485(1999)029<0231:GASWCT>2.0.CO;2

Lippmann, T. C., Irish, J., & Hunt, J. (2013). Observations of the Vertical Structure of Tidal Currents in Two Inlets. *Journal of Coastal Research*, *65*(sp2), 2029–2034. https://doi.org/10.2112/SI65-343.1

Lippmann, T. C., Simpson, A. E., Cook, S. E., & Kirshen, P. (2021). Effects of Sea Level Rise on Storm Surge Flooding and Current Speeds in New Hampshire Estuaries. *Journal of Waterway, Port, Coastal, and Ocean Engineering*, *147*(2), 04020054. https://doi.org/10.1061/(ASCE)WW.1943-5460.0000613

Liu, Z., Zhang, Y. J., Wang, H. V., Huang, H., Wang, Z., Ye, F., & Sisson, M. (2018). Impact of small-scale structures on estuarine circulation. *Ocean Dynamics*, *68*(4–5), 509–533. https://doi.org/10.1007/s10236-018-1148-6

Lloyd, P. M., & Stansby, P. K. (1997). Shallow-Water Flow around Model Conical Islands of Small Side Slope. II: Submerged. *Journal of Hydraulic Engineering*, *123*(12), 1068–1077.

Long, J. W., & Özkan-Haller, H. T. (2009). Low-frequency characteristics of wave group–forced vortices. *Journal of Geophysical Research: Oceans*, *114*(C8). https://doi.org/10.1029/2008JC004894

Ludwick, J. C. (1975). Variations in the boundary-drag coefficient in the tidal entrance to Chesapeake Bay, Virginia. *Marine Geology*, *19*(1), 19–28. https://doi.org/10.1016/0025-3227(75)90003-1

McKenna, L. (2013). *Patterns of Bedform Migration and Mean Tidal Currents in Hampton Harbor Inlet, New Hampshire, USA* [Masters Thesis]. University of New Hampshire.

Mied, R. P., Donato, T. F., & Friedrichs, C. T. (2006). Eddy generation in the tidal Potomac River. *Estuaries and Coasts*, *29*(6), 1067–1080. https://doi.org/10.1007/BF02781810

Nelson, J. M. (1990). The initial instability and finite-amplitude stability of alternate bars in straight channels. *Earth Science Reviews*, 19.

Niiler, P. P., & Mysak, L. A. (1971). Barotropic waves along an eastern continental shelf. *Geophysical Fluid Dynamics*, *2*(1), 273–288. https://doi.org/10.1080/03091927108236063

Noyes, T. J., Guza, R. T., Elgar, S., & Herbers, T. H. C. (2002). Comparison of Methods for Estimating Nearshore Shear Wave Variance. *Journal of Atmospheric and Oceanic Technology*, *19*(1), 136–143. https://doi.org/10.1175/1520-0426(2002)019<0136:COMFEN>2.0.CO;2

Okajima, A. (1982). Strouhal numbers of rectangular cylinders. *Journal of Fluid Mechanics*, *123*, 379–398. https://doi.org/10.1017/S0022112082003115

Oltman-Shay, J., & Guza, R. T. (1984). A Data-Adaptive Ocean Wave Directional-Spectrum Estimator for Pitch and Roll Type Measurements. *Journal of Physical Oceanography*, *14*.

Oltman-Shay, J., & Guza, R. T. (1987). Infragravity Edge Wave Observations on Two California Beaches. *Journal of Physical Oceanography*, *17*, 644–663.

Oltman-Shay, J., Howd, P. A., & Birkemeier, W. A. (1989). Shear instabilities of the mean longshore current: 2. Field observations. *Journal of Geophysical Research*, *94*(C12), 18031. https://doi.org/10.1029/JC094iC12p18031

Ortega-Casanova, J. (2017). On the onset of vortex shedding from 2D confined rectangular cylinders having different aspect ratios: Application to promote mixing fluids. *Chemical Engineering and Processing - Process Intensification*, *120*, 81–92. https://doi.org/10.1016/j.cep.2017.06.014

Özkan-Haller, H. T., & Kirby, J. T. (1999). Nonlinear evolution of shear instabilities of the longshore current: A comparison of observations and computations. *Journal of*

Geophysical Research: Oceans, *104*(C11), 25953–25984.

https://doi.org/10.1029/1999JC900104

Parker, B. (2007). *Tidal Analysis and Prediction* (NOAA Special Publication NOS CO-OPS 3).

National Oceanic and Atmospheric Administration's Center for Operational

Oceanographic Products and Services.

https://tidesandcurrents.noaa.gov/publications/Tidal_Analysis_and_Predictions.pdf

Parker, G., & Andrews, E. D. (1986). On the time development of meander bends. *Journal of*

Fluid Mechanics, *162*(1), 139. https://doi.org/10.1017/S0022112086001970

Pawka, S. S. (1982). *Wave Directional Characteristics on a Partially Sheltered Coast*.

University of California San Diego.

Pawka, S. S. (1983). Island shadows in wave directional spectra. *Journal of Geophysical*

Research, *88*(C4), 2579. https://doi.org/10.1029/JC088iC04p02579

Putrevu, U., & Svendsen, I. A. (1992). Shear instability of longshore currents: A numerical

study. *Journal of Geophysical Research*, *97*(C5), 7283.

https://doi.org/10.1029/91JC02988

Scarlatos, P. D. (1993). Tidal Energy Dissipation in Well-Mixed Estuaries. *Journal of Coastal*

Research, *9*(4), 7.

Seim, H. E., & Gregg, M. C. (1994). Detailed observations of a naturally occurring shear

instability. *Journal of Geophysical Research*, *99*(C5), 10049.

https://doi.org/10.1029/94JC00168

Seminara, G. (2010). Fluvial Sedimentary Patterns. *Annual Review of Fluid Mechanics*, *42*(1),

43–66. https://doi.org/10.1146/annurev-fluid-121108-145612

Shemer, L., Dodd, N., & Thornton, E. B. (1991). Slow-time modulation of finite-depth nonlinear

    water waves: Relation to longshore current oscillations. *Journal of Geophysical*

    Research, *96*(C4), 7105. https://doi.org/10.1029/91JC00061

Signell, R. P., & Geyer, W. R. (1991). Transient eddy formation around headlands. *Journal of*

    Geophysical Research: Oceans, *96*(C2), 2561–2575. https://doi.org/10.1029/90JC02029

Simpson, J. H., Brown, J., Matthews, J., & Allen, G. (1990). Tidal Straining, Density Currents,

    and Stirring in the Control of Estuarine Stratification. *Estuaries*, *13*(2), 125.

    https://doi.org/10.2307/1351581

Thornton, E. B., & Guza, R. T. (1986). *Surf Zone Longshore Currents and Random Waves: Field*

    Data and Models.

Vallis, G. K. (2017). *Atmospheric and Oceanic Fluid Dynamics: Fundamentals and Large-Scale*

    Circulation (Second). Cambridge University Press.

Vincent, M., Hess, K., & Kelley, J. (2003). *NOS Procedures for Developing and Implementing*

    Operational Nowcast and Forecast Hydrodynamic Model Systems (NOAA Technical

    Report NOS CO-OPS 39, p. 25). National Oceanic and Atmospheric Administration.

von Krusenstiern, K. V. (2021). *Sediment Transport and the Temporal Stability of the Seafloor in*

    the Hampton-Seabrook Estuary, NH: A Numerical Model Study [M.S., University of New

    Hampshire].

    https://www.proquest.com/docview/2583148255/abstract/6366678CCDFC4A9DPQ/1

Whitford, D. J., & Thornton, E. B. (1996). Bed shear stress coefficients for longshore currents

    over a barred profile. *Coastal Engineering*, *27*(3–4), 243–262.

    https://doi.org/10.1016/0378-3839(96)00005-1

Winterwerp, J. C., & Wang, Z. B. (2013). Man-induced regime shifts in small estuaries—I:

Theory. *Ocean Dynamics*, *63*(11–12), 1279–1292. https://doi.org/10.1007/s10236-013-

0662-9

APPENDIX A. BOUNDARY CONDITIONS

Table A-1. Matching conditions at region boundaries. The subscripts on the stream function (ψ), sea surface elevation (η), coefficients, and fraction of depth (α) denote the region (0-3), while the subscript on x denotes the cross-inlet location.

Cross-inlet location, x	Stream function, $\psi(x)$	Sea surface elevation, $\eta(x)$
x = 0 (in Region 0)	$\psi_0(0) = 0$	$\eta_0(0) = \dfrac{1}{g(\alpha_0 h)}\left[(c + \dfrac{i}{k}\dfrac{\lambda}{\alpha_0 h})\,\psi_{0x}\right]$
x = $x_1 = \gamma_1 x_0$ (Region 0 = Region 1)	$\psi_0(x_1) = \psi_1(x_1)$	$\eta_0(x_1) = \eta_1(x_1)$
	$A_0 \sinh(kx_1) =$ $A_1 \sinh(kx_1)$ $+\, B_1 \cosh(kx_1)$	$\dfrac{1}{g(\alpha_0 h)}\left[(c + \dfrac{i}{k}\dfrac{\lambda}{\alpha_0 h})\,\psi_{0x}\right] =$ $-\dfrac{1}{g(\alpha_1 h)}\left[\left(V_m - c - \dfrac{i}{k}\dfrac{\lambda}{\alpha_1 h}\right)\psi_{1x}\right.$ $\left. -\, V_{1x}\psi_1\right]$
x = $x_2 =$ $x_0(\gamma_1 + \delta)$ (Region 1 = Region 2)	$\psi_1(x_2) = \psi_2(x_2)$	$\eta_1(x_2) = \eta_2(x_2)$
	$A_1 \sinh(kx_2)$ $+\, B_1 \cosh(kx_2) =$ $A_2 \sinh(kx_2)$ $+\, B_2 \cosh(kx_2)$	$-\dfrac{1}{g(\alpha_1 h)}\left[\left(V_m - c - \dfrac{i}{k}\dfrac{\lambda}{\alpha_1 h}\right)\psi_{1x}\right.$ $\left. -\, V_{1x}\psi_1\right] =$ $-\dfrac{1}{g(\alpha_2 h)}\left[\left(V_m - c - \dfrac{i}{k}\dfrac{\lambda}{\alpha_2 h}\right)\psi_{2x}\right.$ $\left. -\, V_{2x}\psi_2\right]$
x = $x_3 =$	$\psi_2(x_3) = \psi_3(x_3)$	$\eta_2(x_3) = \eta_3(x_3)$

$x_0(\gamma_1 + 1)$ (Region 2 = Region 3)	$A_2 \sinh(kx_3)$ $+ B_2 \cosh(kx_3) =$ $A_3[\sinh(kx_3)$ $- \tanh(kx_{max})\cosh(kx_3)]$	$-\dfrac{1}{g(\alpha_2 h)}\left[\left(V_m - c - \dfrac{i}{k}\dfrac{\lambda}{\alpha_2 h}\right)\psi_{2x}\right.$ $\left. - V_{2x}\psi_2\right] =$ $\dfrac{1}{g(\alpha_3 h)}\left[(c + \dfrac{i}{k}\dfrac{\lambda}{\alpha_3 h})\,\psi_{3x}\right]$
$x = x_{max} =$ $x_0(\gamma_1 + 1 + \gamma_2)$ (in Region 3)	$\psi_3(x_{max}) = 0$	$\eta_3(x_{max}) = \dfrac{1}{g(\alpha_3 h)}\left[(c + \dfrac{i}{k}\dfrac{\lambda}{\alpha_3 h})\,\psi_{3x}\right]$

APPENDIX B. COEFFICIENT EQUATIONS

The resulting coefficient (A and B) equations after applying boundary conditions (Table A-1). The indexing on the coefficients and fraction of depth (α) indicates the region. Note C is shorthand for the hyperbolic cosine and S is shorthand for the hyperbolic sine. The indexing on C, S, and velocity (V) denotes the location across the inlet, e.g. $C_1 = \cosh(kx_1)$. V_m is the max velocity, k is the wavenumber, and T_L is short hand for $\tanh(x_{max})$.

$$A_0 = A_1 + \frac{B_1 C_1}{S_1}$$

$$\frac{B_1}{A_1} = \frac{\sigma C_1 S_1 (\alpha_1 - \alpha_0) - \alpha_0 V_{1x} S_1^2 + i\frac{\lambda}{h} C_1 S_1 \left(\frac{\alpha_1}{\alpha_0} - \frac{\alpha_0}{\alpha_1}\right)}{\alpha_0 V_{1x} C_1 S_1 - \sigma(\alpha_1 C_1^2 - \alpha_0 S_1^2) - i\frac{\lambda}{h}\left(\frac{\alpha_1}{\alpha_0} C_1^2 - \frac{\alpha_0}{\alpha_1} S_1^2\right)}$$

$$A_2 = A_1 + \frac{B_1 C_2}{S_2} - \frac{B_2 C_2}{S_2}$$

$$\frac{B_1}{A_1} =$$

$$\frac{\sigma C_2 S_2 (\alpha_2 - \alpha_1) + k V_m C_2 S_2 (\alpha_1 - \alpha_2) + S_2^2 (\alpha_2 V_{1x} - \alpha_1 V_{2x}) + i\frac{\lambda}{h} C_2 S_2 \left(\frac{\alpha_2}{\alpha_1} - \frac{\alpha_1}{\alpha_2}\right) + B_2\left(\sigma\alpha_1 - \alpha_1 k V_m + \frac{\alpha_1}{\alpha_2} i\frac{\lambda}{h}\right)}{\sigma(\alpha_1 C_2^2 - \alpha_2 S_2^2) - k V_m (\alpha_1 C_2^2 - \alpha_2 S_2^2) - C_2 S_2 (\alpha_2 V_{1x} - \alpha_1 V_{2x}) + i\frac{\lambda}{h}\left(\frac{\alpha_1}{\alpha_2} C_2^2 - \frac{\alpha_2}{\alpha_1} S_2^2\right)}$$

$$A_3 = \frac{A_2 S_3 + B_2 C_3}{S_3 - T_L C_3}$$

$$\frac{B_2}{A_2} =$$

$$\frac{\sigma[\alpha_2 S_3 (C_3 - T_L S_3) - \alpha_3 C_3 (S_3 - T_L C_3)] - \alpha_3 V_{2x} S_3 (S_3 - T_L C_3) - i\frac{\lambda}{h}\left(\frac{\alpha_3}{\alpha_2} C_3 (S_3 - T_L C_3) - \frac{\alpha_2}{\alpha_3} S_3 (C_3 - T_L S_3)\right)}{\sigma[\alpha_3 S_3 (S_3 - T_L C_3) - \alpha_2 C_3 (C_3 - T_L S_3)] + \alpha_3 V_{2x} C_3 (S_3 - T_L C_3) - i\frac{\lambda}{h}\left(\frac{\alpha_2}{\alpha_3} C_3 (C_3 - T_L S_3) - \frac{\alpha_3}{\alpha_2} S_3 (S_3 - T_L C_3)\right)}$$

APPENDIX C. CUBIC SOLUTION

The cubic equation for linear instabilities of tidal currents through a laterally bounded inlet is below. Note C, S, and T are shorthand for the hyperbolic cosine, sine and tangent, respectively. The indexing on C and S denotes the location across the inlet, e.g. $C_1 = \cosh(kx_1)$. V_m is the max velocity, k is the wavenumber, and T_L is short hand for $\tanh(x_{max})$. Derivatives are expressed in the subscript and the subscript on velocity indicates the velocity magnitude in that region, e.g. V_1 is the velocity magnitude in Region 1, and $V_{1x} = \frac{\partial V_1}{\partial x}$.

$$0 = \sigma^3 \left[\begin{array}{c} (\alpha_1 + C_2^2(\alpha_2 - \alpha_1))(\alpha_1 C_1^2 - \alpha_0 S_1^2)\left(\alpha_2 S_3\left(\frac{C_3}{T_L} - S_3\right) - \alpha_3 C_3\left(\frac{S_3}{T_L} - C_3\right)\right) \\ + (C_2 S_2(\alpha_2 - \alpha_1)(\alpha_1 C_1^2 - \alpha_0 S_1^2) + C_1 S_1(\alpha_1 - \alpha_0)(\alpha_1 C_2^2 - \alpha_2 S_2^2)) \times \\ \left(\alpha_3 S_3\left(\frac{S_3}{T_L} - C_3\right) - \alpha_2 C_3\left(\frac{C_3}{T_L} - S_3\right)\right) \\ + \left((\alpha_1 C_2^2 - \alpha_2 S_2^2) - \alpha_1\right)\left(\frac{C_1 S_1 C_2}{S_2}(\alpha_1 - \alpha_0)\left(\alpha_2 S_3\left(\frac{C_3}{T_L} - S_3\right) - \alpha_3 C_3\left(\frac{S_3}{T_L} - C_3\right)\right)\right) \end{array} \right]$$

$$
+\sigma^2 \left[\begin{array}{c}
-(\alpha_1 + C_2^2(\alpha_2 - \alpha_1))(\alpha_1 C_1^2 - \alpha_0 S_1^2)\left(\alpha_3 V_{2x} S_3\left(\frac{S_3}{T_L} - C_3\right) + i\frac{\lambda}{h}\left(\frac{\alpha_3}{\alpha_2}C_3\left(\frac{S_3}{T_L} - C_3\right) - \frac{\alpha_2}{\alpha_3}S_3\left(\frac{C_3}{T_L} - S_3\right)\right)\right) \\[2mm]
-kV_m(\alpha_1 - C_2^2(\alpha_1 - \alpha_2))(\alpha_1 C_1^2 - \alpha_0 S_1^2)\left(\alpha_2 S_3\left(\frac{C_3}{T_L} - S_3\right) - \alpha_3 C_3\left(\frac{S_3}{T_L} - C_3\right)\right) \\[2mm]
+i\frac{\lambda}{h}\left(\frac{\alpha_1}{\alpha_2}(\alpha_1 C_1^2 - \alpha_0 S_1^2) + \alpha_1\left(\frac{\alpha_1}{\alpha_0}C_1^2 - \frac{\alpha_0}{\alpha_1}S_1^2\right)\right)\left(\alpha_2 S_3\left(\frac{C_3}{T_L} - S_3\right) - \alpha_3 C_3\left(\frac{S_3}{T_L} - C_3\right)\right) \\[2mm]
-\alpha_0 V_{1x} C_1 S_1(\alpha_1 + C_2^2(\alpha_2 - \alpha_1))\left(\alpha_2 S_3\left(\frac{C_3}{T_L} - S_3\right) - \alpha_3 C_3\left(\frac{S_3}{T_L} - C_3\right)\right) \\[2mm]
+S_2\left(kV_m C_2(\alpha_1 - \alpha_2) + S_2(\alpha_2 V_{1x} - \alpha_1 V_{2x}) + i\frac{\lambda}{h}C_2\left(\frac{\alpha_2}{\alpha_1} - \frac{\alpha_1}{\alpha_2}\right)\right) \times \\[2mm]
(\alpha_1 C_1^2 - \alpha_0 S_1^2)\left(\alpha_3 S_3\left(\frac{S_3}{T_L} - C_3\right) - \alpha_2 C_3\left(\frac{C_3}{T_L} - S_3\right)\right) \\[2mm]
+ C_2 S_2(\alpha_1 C_1^2 - \alpha_0 S_1^2)\left(\begin{array}{c} (\alpha_2 - \alpha_1)\left(\alpha_3 V_{2x} C_3\left(\frac{S_3}{T_L} - C_3\right)\right) \\[1mm] -i\frac{\lambda}{h}(\alpha_2 - \alpha_1)\left(\frac{\alpha_2}{\alpha_3}C_3\left(\frac{C_3}{T_L} - S_3\right) - \frac{\alpha_3}{\alpha_2}S_3\left(\frac{S_3}{T_L} - C_3\right)\right) \\[1mm] + \left((\alpha_2 V_{1x} - \alpha_1 V_{2x})\left(\alpha_2 S_3\left(\frac{C_3}{T_L} - S_3\right) - \alpha_3 C_3\left(\frac{S_3}{T_L} - C_3\right)\right)\right) \end{array} \right) \\[2mm]
+ i\frac{\lambda}{h}C_2^2\left((\alpha_1 C_1^2 - \alpha_0 S_1^2)\left(\frac{\alpha_2}{\alpha_1} - \frac{\alpha_1}{\alpha_2}\right) + \left(\frac{\alpha_1}{\alpha_0}C_1^2 - \frac{\alpha_0}{\alpha_1}S_1^2\right)(\alpha_2 - \alpha_1)\right)\left(\alpha_2 S_3\left(\frac{C_3}{T_L} - S_3\right) - \alpha_3 C_3\left(\frac{S_3}{T_L} - C_3\right)\right) \\[2mm]
+C_2 S_2(\alpha_2 - \alpha_1)\left(i\frac{\lambda}{h}\left(\frac{\alpha_1}{\alpha_0}C_1^2 - \frac{\alpha_0}{\alpha_1}S_1^2\right) - \alpha_0 V_{1x} C_1 S_1\right)\left(\alpha_3 S_3\left(\frac{S_3}{T_L} - C_3\right) - \alpha_2 C_3\left(\frac{C_3}{T_L} - S_3\right)\right) \\[2mm]
-C_1 S_1(\alpha_1 - \alpha_0)\left(kV_m(\alpha_1 C_2^2 - \alpha_2 S_2^2) + C_2 S_2(\alpha_2 V_{1x} - \alpha_1 V_{2x}) - i\frac{\lambda}{h}\left(\frac{\alpha_1}{\alpha_2}C_2^2 - \frac{\alpha_2}{\alpha_1}S_2^2\right)\right) \times \\[2mm]
\left(\left(\alpha_3 S_3\left(\frac{S_3}{T_L} - C_3\right) - \alpha_2 C_3\left(\frac{C_3}{T_L} - S_3\right)\right) + \frac{C_2}{S_2}\left(\alpha_2 S_3\left(\frac{C_3}{T_L} - S_3\right) - \alpha_3 C_3\left(\frac{S_3}{T_L} - C_3\right)\right)\right) \\[2mm]
+ C_1 S_1(\alpha_1 - \alpha_0)(\alpha_1 C_2^2 - \alpha_2 S_2^2)\left(\alpha_3 V_{2x}\left(\frac{S_3}{T_L} - C_3\right)\left(C_3 - \frac{C_2 S_3}{S_2}\right) - i\frac{\lambda}{h}\left(\frac{\alpha_2}{\alpha_3}C_3\left(\frac{C_3}{T_L} - S_3\right) - \frac{\alpha_3}{\alpha_2}S_3\left(\frac{S_3}{T_L} - C_3\right)\right)\right) \\[2mm]
+ i\frac{\lambda}{h}\frac{C_1 S_1 C_2}{S_2}(\alpha_1 - (\alpha_1 C_2^2 - \alpha_2 S_2^2))(\alpha_1 - \alpha_0)\left(\frac{\alpha_3}{\alpha_2}C_3\left(\frac{S_3}{T_L} - C_3\right) - \frac{\alpha_2}{\alpha_3}S_3\left(\frac{C_3}{T_L} - S_3\right)\right) \\[2mm]
-S_1\left(\alpha_0 V_{1x} S_1 - i\frac{\lambda}{h}C_1\left(\frac{\alpha_1}{\alpha_0} - \frac{\alpha_0}{\alpha_1}\right)\right)(\alpha_1 C_2^2 - \alpha_2 S_2^2) \times \\[2mm]
\left(\left(\alpha_3 S_3\left(\frac{S_3}{T_L} - C_3\right) - \alpha_2 C_3\left(\frac{C_3}{T_L} - S_3\right)\right) + \frac{C_2}{S_2}\left(\alpha_2 S_3\left(\frac{C_3}{T_L} - S_3\right) - \alpha_3 C_3\left(\frac{S_3}{T_L} - C_3\right)\right)\right) \\[2mm]
+ \alpha_1 \frac{C_2}{S_2}C_1 S_1 \alpha_3 V_{2x} S_3(\alpha_1 - \alpha_0)\left(\frac{S_3}{T_L} - C_3\right) \\[2mm]
+ S_1 \alpha_1 \frac{C_2}{S_2}(C_1 kV_m(\alpha_1 - \alpha_0) + \alpha_0 V_{1x} S_1)\left(\alpha_2 S_3\left(\frac{C_3}{T_L} - S_3\right) - \alpha_3 C_3\left(\frac{S_3}{T_L} - C_3\right)\right) \\[2mm]
-i\frac{\lambda}{h}\frac{C_2}{S_2}C_1 S_1\left(\frac{\alpha_1}{\alpha_2}(\alpha_1 - \alpha_0) + \alpha_1\left(\frac{\alpha_1}{\alpha_0} - \frac{\alpha_0}{\alpha_1}\right)\right)\left(\alpha_2 S_3\left(\frac{C_3}{T_L} - S_3\right) - \alpha_3 C_3\left(\frac{S_3}{T_L} - C_3\right)\right)
\end{array} \right]
$$

$$+\sigma\left[\begin{aligned}
&\left(\alpha_1 k V_m - i\frac{\lambda}{h}\frac{\alpha_1}{\alpha_2}\right)\left(\alpha_3 V_{2x}S_3\left(\frac{S_3}{T_L}-C_3\right)(\alpha_1 C_1^2 - \alpha_0 S_1^2) + \alpha_0 V_{1x}C_1 S_1\left(\alpha_2 S_3\left(\frac{C_3}{T_L}-S_3\right) - \alpha_3 C_3\left(\frac{S_3}{T_L}-C_3\right)\right)\right)\\[4pt]
&+\frac{\lambda}{h}\left(\alpha_1 k V_m i + \frac{\lambda}{h}\frac{\alpha_1}{\alpha_2}\right)\left(\begin{aligned}&(\alpha_1 C_1^2 - \alpha_0 S_1^2)\left(\frac{\alpha_3}{\alpha_2}C_3\left(\frac{S_3}{T_L}-C_3\right) - \frac{\alpha_2}{\alpha_3}S_3\left(\frac{C_3}{T_L}-S_3\right)\right)-\\&\left(\frac{\alpha_1}{\alpha_0}C_1^2 - \frac{\alpha_0}{\alpha_1}S_1^2\right)\left(\alpha_2 S_3\left(\frac{C_3}{T_L}-S_3\right) - \alpha_3 C_3\left(\frac{S_3}{T_L}-C_3\right)\right)\end{aligned}\right)\\[4pt]
&+\frac{\lambda}{h}\left(\alpha_0 V_{1x}C_1 S_1 \alpha_1 i + \alpha_1 \frac{\lambda}{h}\left(\frac{\alpha_1}{\alpha_0}C_1^2 - \frac{\alpha_0}{\alpha_1}S_1^2\right)\right)\left(\frac{\alpha_3}{\alpha_2}C_3\left(\frac{S_3}{T_L}-C_3\right) - \frac{\alpha_2}{\alpha_3}S_3\left(\frac{C_3}{T_L}-S_3\right)\right)\\[4pt]
&+\alpha_1 \alpha_3 V_{2x}S_3\left(\frac{S_3}{T_L}-C_3\right)\left(\alpha_0 V_{1x}C_1 S_1 - i\frac{\lambda}{h}\left(\frac{\alpha_1}{\alpha_0}C_1^2 - \frac{\alpha_0}{\alpha_1}S_1^2\right)\right)\\[4pt]
&+S_2(k V_m C_2(\alpha_1 - \alpha_2) + S_2(\alpha_2 V_{1x} - \alpha_1 V_{2x}))(\alpha_1 C_1^2 - \alpha_0 S_1^2)\times\\[2pt]
&\qquad\left(\alpha_3 V_{2x}C_3\left(\frac{S_3}{T_L}-C_3\right) - i\frac{\lambda}{h}\left(\frac{\alpha_2}{\alpha_3}C_3\left(\frac{C_3}{T_L}-S_3\right) - \frac{\alpha_3}{\alpha_2}S_3\left(\frac{S_3}{T_L}-C_3\right)\right)\right)\\[4pt]
&-C_2 \alpha_3 V_{2x}\left(k V_m C_2 S_3(\alpha_1 - \alpha_2) - i\frac{\lambda}{h}S_2 C_3\left(\frac{\alpha_2}{\alpha_1}-\frac{\alpha_1}{\alpha_2}\right)\right)(\alpha_1 C_1^2 - \alpha_0 S_1^2)\left(\frac{S_3}{T_L}-C_3\right)\\[4pt]
&+\left(\frac{\lambda}{h}\right)^2 C_2 S_2\left(\frac{\alpha_2}{\alpha_1}-\frac{\alpha_1}{\alpha_2}\right)(\alpha_1 C_1^2 - \alpha_0 S_1^2)\left(\frac{\alpha_2}{\alpha_3}C_3\left(\frac{C_3}{T_L}-S_3\right) - \frac{\alpha_3}{\alpha_2}S_3\left(\frac{S_3}{T_L}-C_3\right)\right)\\[4pt]
&-i\frac{\lambda}{h}C_2(k V_m C_2(\alpha_1 - \alpha_2) + S_2(\alpha_2 V_{1x} - \alpha_1 V_{2x}))\times\\[2pt]
&\qquad\left(\begin{aligned}&(\alpha_1 C_1^2 - \alpha_0 S_1^2)\left(\frac{\alpha_3}{\alpha_2}C_3\left(\frac{S_3}{T_L}-C_3\right) - \frac{\alpha_2}{\alpha_3}S_3\left(\frac{C_3}{T_L}-S_3\right)\right)-\\&\left(\frac{\alpha_1}{\alpha_0}C_1^2 - \frac{\alpha_0}{\alpha_1}S_1^2\right)\left(\alpha_2 S_3\left(\frac{C_3}{T_L}-S_3\right) - \alpha_3 C_3\left(\frac{S_3}{T_L}-C_3\right)\right)\end{aligned}\right)\\[4pt]
&-C_2 \alpha_3 V_{2x}S_3\left(S_2(\alpha_2 V_{1x} - \alpha_1 V_{2x}) + i\frac{\lambda}{h}C_2\left(\frac{\alpha_2}{\alpha_1}-\frac{\alpha_1}{\alpha_2}\right)\right)(\alpha_1 C_1^2 - \alpha_0 S_1^2)\left(\frac{S_3}{T_L}-C_3\right)\\[4pt]
&+C_2 \alpha_0 V_{1x}S_1^2\left(C_2(\alpha_2 V_{1x} - \alpha_1 V_{2x}) - \frac{i}{S_2}\frac{\lambda}{h}\left(\frac{\alpha_1}{\alpha_2}C_2^2 - \frac{\alpha_2}{\alpha_1}S_2^2\right)\right)\left(\alpha_2 S_3\left(\frac{C_3}{T_L}-S_3\right) - \alpha_3 C_3\left(\frac{S_3}{T_L}-C_3\right)\right)\\[4pt]
&+i\frac{\lambda}{h}C_1 S_1 \alpha_3 V_{2x}\left(C_3\left(\frac{\alpha_1}{\alpha_0}-\frac{\alpha_0}{\alpha_1}\right)(\alpha_1 C_2^2 - \alpha_2 S_2^2) - \frac{C_2 S_3}{S_2}(\alpha_1 - \alpha_0)\left(\frac{\alpha_1}{\alpha_2}C_2^2 - \frac{\alpha_2}{\alpha_1}S_2^2\right)\right)\left(\frac{S_3}{T_L}-C_3\right)\\[4pt]
&+\left(\frac{\lambda}{h}\right)^2 C_1 S_1 \frac{C_2}{S_2}\left(\left(\frac{\alpha_1}{\alpha_2}C_2^2 - \frac{\alpha_2}{\alpha_1}S_2^2\right)(\alpha_1 - \alpha_0) + \left(\frac{\alpha_1}{\alpha_0}-\frac{\alpha_0}{\alpha_1}\right)(\alpha_1 C_2^2 - \alpha_2 S_2^2)\right)\left(\frac{\alpha_3}{\alpha_2}C_3\left(\frac{S_3}{T_L}-C_3\right) - \frac{\alpha_2}{\alpha_3}S_3\left(\frac{C_3}{T_L}-S_3\right)\right)\\[4pt]
&-i\frac{\lambda}{h}C_1 S_1 \frac{C_2}{S_2}\alpha_3 V_{2x}S_3\left(\frac{\alpha_1}{\alpha_0}-\frac{\alpha_0}{\alpha_1}\right)\left(\frac{S_3}{T_L}-C_3\right)(\alpha_1 C_2^2 - \alpha_2 S_2^2)\\[4pt]
&+\left(\frac{\lambda}{h}\right)^2 C_1 S_1 \frac{C_2}{S_2}\frac{\alpha_1}{\alpha_2}\left(\frac{\alpha_1}{\alpha_0}-\frac{\alpha_0}{\alpha_1}\right)\left(\alpha_2 S_3\left(\frac{C_3}{T_L}-S_3\right) - \alpha_3 C_3\left(\frac{S_3}{T_L}-C_3\right)\right)\\[4pt]
&-\frac{C_2}{S_2}C_1 S_1 \alpha_3 V_{2x}S_3\left(\alpha_1 k V_m - i\frac{\lambda}{h}\frac{\alpha_1}{\alpha_2}\right)(\alpha_1 - \alpha_0)\left(\frac{S_3}{T_L}-C_3\right)\\[4pt]
&-\frac{\lambda}{h}\frac{C_2}{S_2}C_1 S_1\left(i\alpha_1 k V_m + \frac{\lambda}{h}\frac{\alpha_1}{\alpha_2}\right)(\alpha_1 - \alpha_0)\left(\frac{\alpha_3}{\alpha_2}C_3\left(\frac{S_3}{T_L}-C_3\right) - \frac{\alpha_2}{\alpha_3}S_3\left(\frac{C_3}{T_L}-S_3\right)\right)\\[4pt]
&-\frac{C_2}{S_2}\alpha_1 S_1 \alpha_3 V_{2x}S_3\left(\alpha_0 V_{1x}S_1 - i\frac{\lambda}{h}C_1\left(\frac{\alpha_1}{\alpha_0}-\frac{\alpha_0}{\alpha_1}\right)\right)\left(\frac{S_3}{T_L}-C_3\right)\\[4pt]
&-\frac{\lambda}{h}\frac{C_2}{S_2}\alpha_1 S_1\left(i\alpha_0 V_{1x}S_1 + \frac{\lambda}{h}C_1\left(\frac{\alpha_1}{\alpha_0}-\frac{\alpha_0}{\alpha_1}\right)\right)\left(\frac{\alpha_3}{\alpha_2}C_3\left(\frac{S_3}{T_L}-C_3\right) - \frac{\alpha_2}{\alpha_3}S_3\left(\frac{C_3}{T_L}-S_3\right)\right)\\[4pt]
&+S_1 \frac{C_2}{S_2}\left(i\frac{\lambda}{h}C_1 \alpha_1 k V_m\left(\frac{\alpha_1}{\alpha_0}-\frac{\alpha_0}{\alpha_1}\right) + i\frac{\lambda}{h}\frac{\alpha_1}{\alpha_2}\alpha_0 V_{1x}S_1 - \alpha_0 V_{1x}S_1 \alpha_1 k V_m\right)\left(\alpha_2 S_3\left(\frac{C_3}{T_L}-S_3\right) - \alpha_3 C_3\left(\frac{S_3}{T_L}-C_3\right)\right)\\[4pt]
&+\left(\frac{\lambda}{h}\right)^2 C_1 S_1\left(\frac{\alpha_1}{\alpha_0}-\frac{\alpha_0}{\alpha_1}\right)(\alpha_1 C_2^2 - \alpha_2 S_2^2)\left(\frac{\alpha_2}{\alpha_3}C_3\left(\frac{C_3}{T_L}-S_3\right) - \frac{\alpha_3}{\alpha_2}S_3\left(\frac{S_3}{T_L}-C_3\right)\right)
\end{aligned}\right]$$

125

$$\begin{bmatrix}
+ C_2^2 \frac{\lambda}{h}\left(\frac{\lambda}{h}(\alpha_1 C_1^2 - \alpha_0 S_1^2)\left(\frac{\alpha_2}{\alpha_1} - \frac{\alpha_1}{\alpha_2}\right) + i\alpha_0 V_{1x} C_1 S_1(\alpha_2 - \alpha_1)\right)\left(\frac{\alpha_3}{\alpha_2} C_3\left(\frac{S_3}{T_L} - C_3\right) - \frac{\alpha_2}{\alpha_3} S_3\left(\frac{C_3}{T_L} - S_3\right)\right) \\[6pt]
- \alpha_0 V_{1x} C_1 S_1 S_2\left(kV_m C_2(\alpha_1 - \alpha_2) + S_2(\alpha_2 V_{1x} - \alpha_1 V_{2x}) + i\frac{\lambda}{h}C_2\left(\frac{\alpha_2}{\alpha_1} - \frac{\alpha_1}{\alpha_2}\right)\right) \times \\[6pt]
\left(\alpha_3 S_3\left(\frac{S_3}{T_L} - C_3\right) - \alpha_2 C_3\left(\frac{C_3}{T_L} - S_3\right)\right) \\[6pt]
+ \alpha_0 V_{1x} C_1 S_1 C_2 \alpha_3 V_{2x}(C_2 S_3 - C_3 S_2)\left(\frac{S_3}{T_L} - C_3\right)(\alpha_2 - \alpha_1) \\[6pt]
- \alpha_0 V_{1x} C_1 S_1 C_2\left(kV_m C_2(\alpha_1 - \alpha_2) + S_2(\alpha_2 V_{1x} - \alpha_1 V_{2x}) + i\frac{\lambda}{h}C_2\left(\frac{\alpha_2}{\alpha_1} - \frac{\alpha_1}{\alpha_2}\right)\right) \times \\[6pt]
\left(\alpha_2 S_3\left(\frac{C_3}{T_L} - S_3\right) - \alpha_3 C_3\left(\frac{S_3}{T_L} - C_3\right)\right) \\[6pt]
+ \frac{\lambda}{h}S_2\left(ikV_m C_2(\alpha_1 - \alpha_2) + iS_2(\alpha_2 V_{1x} - \alpha_1 V_{2x}) - \frac{\lambda}{h}C_2\left(\frac{\alpha_2}{\alpha_1} - \frac{\alpha_1}{\alpha_2}\right)\right) \times \\[6pt]
\left(\frac{\alpha_1}{\alpha_0}C_1^2 - \frac{\alpha_0}{\alpha_1}S_1^2\right)\left(\alpha_3 S_3\left(\frac{S_3}{T_L} - C_3\right) - \alpha_2 C_3\left(\frac{C_3}{T_L} - S_3\right)\right) \\[6pt]
+ i\frac{\lambda}{h}C_2 \alpha_3 V_{2x}(C_3 S_2 - C_2 S_3)\left(\frac{\alpha_1}{\alpha_0}C_1^2 - \frac{\alpha_0}{\alpha_1}S_1^2\right)\left(\frac{S_3}{T_L} - C_3\right)(\alpha_2 - \alpha_1) \\[6pt]
+ \frac{\lambda}{h}C_2 S_2\left(\alpha_0 V_{1x} C_1 S_1 i + \frac{\lambda}{h}\left(\frac{\alpha_1}{\alpha_0}C_1^2 - \frac{\alpha_0}{\alpha_1}S_1^2\right)\right)(\alpha_2 - \alpha_1)\left(\frac{\alpha_2}{\alpha_3} C_3\left(\frac{C_3}{T_L} - S_3\right) - \frac{\alpha_3}{\alpha_2} S_3\left(\frac{S_3}{T_L} - C_3\right)\right) \\[6pt]
+ C_2^2\left(\frac{\lambda}{h}\right)^2\left(\frac{\alpha_1}{\alpha_0}C_1^2 - \frac{\alpha_0}{\alpha_1}S_1^2\right)\begin{pmatrix}(\alpha_2 - \alpha_1)\left(\frac{\alpha_3}{\alpha_2} C_3\left(\frac{S_3}{T_L} - C_3\right) - \frac{\alpha_2}{\alpha_3} S_3\left(\frac{C_3}{T_L} - S_3\right)\right) - \\[6pt] \left(\frac{\alpha_2}{\alpha_1} - \frac{\alpha_1}{\alpha_2}\right)\left(\alpha_2 S_3\left(\frac{C_3}{T_L} - S_3\right) - \alpha_3 C_3\left(\frac{S_3}{T_L} - C_3\right)\right)\end{pmatrix} \\[6pt]
+ S_1\left(kV_m(\alpha_1 C_2^2 - \alpha_2 S_2^2) + C_2 S_2(\alpha_2 V_{1x} - \alpha_1 V_{2x}) - i\frac{\lambda}{h}\left(\frac{\alpha_1}{\alpha_2}C_2^2 - \frac{\alpha_2}{\alpha_1}S_2^2\right)\right) \times \\[6pt]
\left(\alpha_0 V_{1x}\left(\alpha_3 S_3\left(\frac{S_3}{T_L} - C_3\right) - \alpha_2 C_3\left(\frac{C_3}{T_L} - S_3\right)\right) - C_1 C_3 \alpha_3 V_{2x}(\alpha_1 - \alpha_0)\left(\frac{S_3}{T_L} - C_3\right)\right) \\[6pt]
+ \frac{\lambda}{h}C_1 S_1\left(ikV_m(\alpha_1 C_2^2 - \alpha_2 S_2^2) + iC_2 S_2(\alpha_2 V_{1x} - \alpha_1 V_{2x}) + \frac{\lambda}{h}\left(\frac{\alpha_1}{\alpha_2}C_2^2 - \frac{\alpha_2}{\alpha_1}S_2^2\right)\right) \times \\[6pt]
\left((\alpha_1 - \alpha_0)\left(\frac{\alpha_2}{\alpha_3} C_3\left(\frac{C_3}{T_L} - S_3\right) - \frac{\alpha_3}{\alpha_2} S_3\left(\frac{S_3}{T_L} - C_3\right)\right) - \left(\frac{\alpha_1}{\alpha_0} - \frac{\alpha_0}{\alpha_1}\right)\left(\alpha_3 S_3\left(\frac{S_3}{T_L} - C_3\right) - \alpha_2 C_3\left(\frac{C_3}{T_L} - S_3\right)\right)\right) \\[6pt]
+ C_1 S_1 C_2\left(\frac{kV_m}{S_2}(\alpha_1 C_2^2 - \alpha_2 S_2^2) + C_2(\alpha_2 V_{1x} - \alpha_1 V_{2x})\right) \times \\[6pt]
\begin{pmatrix}(\alpha_1 - \alpha_0)\left(S_3 \alpha_3 V_{2x}\left(\frac{S_3}{T_L} - C_3\right) + i\frac{\lambda}{h}\left(\frac{\alpha_3}{\alpha_2} C_3\left(\frac{S_3}{T_L} - C_3\right) - \frac{\alpha_2}{\alpha_3} S_3\left(\frac{C_3}{T_L} - S_3\right)\right)\right) - \\[6pt] i\frac{\lambda}{h}\left(\frac{\alpha_1}{\alpha_0} - \frac{\alpha_0}{\alpha_1}\right)\left(\alpha_2 S_3\left(\frac{C_3}{T_L} - S_3\right) - \alpha_3 C_3\left(\frac{S_3}{T_L} - C_3\right)\right)\end{pmatrix} \\[6pt]
+ \alpha_0 V_{1x} \alpha_3 V_{2x} S_1^2\left(\frac{C_2 S_3}{S_2} - C_3\right)(\alpha_1 C_2^2 - \alpha_2 S_2^2)\left(\frac{S_3}{T_L} - C_3\right) \\[6pt]
+ \alpha_0 V_{1x} S_1^2(\alpha_1 C_2^2 - \alpha_2 S_2^2)\begin{pmatrix}\frac{C_2}{S_2}kV_m\left(\alpha_2 S_3\left(\frac{C_3}{T_L} - S_3\right) - \alpha_3 C_3\left(\frac{S_3}{T_L} - C_3\right)\right) \\[6pt] + i\frac{\lambda}{h}\frac{C_2}{S_2}\left(\frac{\alpha_3}{\alpha_2} C_3\left(\frac{S_3}{T_L} - C_3\right) - \frac{\alpha_2}{\alpha_3} S_3\left(\frac{C_3}{T_L} - S_3\right)\right) \\[6pt] + i\frac{\lambda}{h}\left(\frac{\alpha_2}{\alpha_3} C_3\left(\frac{C_3}{T_L} - S_3\right) - \frac{\alpha_3}{\alpha_2} S_3\left(\frac{S_3}{T_L} - C_3\right)\right)\end{pmatrix}
\end{bmatrix}$$

$$+ \left[\begin{array}{l}
-\left(\alpha_1 k V_m - i\frac{\lambda}{h}\frac{\alpha_1}{\alpha_2}\right)\left(\begin{array}{c}\alpha_0 V_{1x}C_1 S_1 \alpha_3 V_{2x} S_3\left(\frac{S_3}{T_L}-C_3\right) + \left(\frac{\lambda}{h}\right)^2\left(\frac{\alpha_1}{\alpha_0}C_1^2 - \frac{\alpha_0}{\alpha_1}S_1^2\right)\times \\ \left(\frac{\alpha_3}{\alpha_2}C_3\left(\frac{S_3}{T_L}-C_3\right) - \frac{\alpha_2}{\alpha_3}S_3\left(\frac{C_3}{T_L}-S_3\right)\right)\end{array}\right) \\[4ex]
-\left(i\alpha_1 k V_m + \frac{\lambda}{h}\frac{\alpha_1}{\alpha_2}\right)\left(\begin{array}{c}\alpha_0 V_{1x}C_1 S_1 \frac{\lambda}{h}\left(\frac{\alpha_3}{\alpha_2}C_3\left(\frac{S_3}{T_L}-C_3\right) - \frac{\alpha_2}{\alpha_3}S_3\left(\frac{C_3}{T_L}-S_3\right)\right) - \\ \alpha_3 V_{2x}S_3\frac{\lambda}{h}\left(\frac{S_3}{T_L}-C_3\right)\left(\frac{\alpha_1}{\alpha_0}C_1^2 - \frac{\alpha_0}{\alpha_1}S_1^2\right)\end{array}\right) \\[4ex]
- S_2\left(k V_m C_2(\alpha_1 - \alpha_2) + S_2(\alpha_2 V_{1x} - \alpha_1 V_{2x}) + i\frac{\lambda}{h}C_2\left(\frac{\alpha_2}{\alpha_1}-\frac{\alpha_1}{\alpha_2}\right)\right)\times \\[2ex]
\left(\alpha_0 V_{1x}C_1 S_1 \alpha_3 V_{2x} C_3\left(\frac{S_3}{T_L}-C_3\right) - \left(\frac{\lambda}{h}\right)^2\left(\frac{\alpha_1}{\alpha_0}C_1^2 - \frac{\alpha_0}{\alpha_1}S_1^2\right)\left(\frac{\alpha_2}{\alpha_3}C_3\left(\frac{C_3}{T_L}-S_3\right) - \frac{\alpha_3}{\alpha_2}S_3\left(\frac{S_3}{T_L}-C_3\right)\right)\right) \\[2ex]
+ S_2\frac{\lambda}{h}\left(ik V_m C_2(\alpha_1 - \alpha_2) + iS_2(\alpha_2 V_{1x} - \alpha_1 V_{2x}) - \frac{\lambda}{h}C_2\left(\frac{\alpha_2}{\alpha_1}-\frac{\alpha_1}{\alpha_2}\right)\right)\times \\[2ex]
\left(\alpha_3 V_{2x}C_3\left(\frac{\alpha_1}{\alpha_0}C_1^2 - \frac{\alpha_0}{\alpha_1}S_1^2\right)\left(\frac{S_3}{T_L}-C_3\right) + \alpha_0 V_{1x}C_1 S_1\left(\frac{\alpha_2}{\alpha_3}C_3\left(\frac{C_3}{T_L}-S_3\right) - \frac{\alpha_3}{\alpha_2}S_3\left(\frac{S_3}{T_L}-C_3\right)\right)\right) \\[2ex]
+ C_2\left(k V_m C_2(\alpha_1 - \alpha_2) + S_2(\alpha_2 V_{1x} - \alpha_1 V_{2x}) + i\frac{\lambda}{h}C_2\left(\frac{\alpha_2}{\alpha_1}-\frac{\alpha_1}{\alpha_2}\right)\right)\times \\[2ex]
\left(\alpha_0 V_{1x}C_1 S_1 \alpha_3 V_{2x} S_3\left(\frac{S_3}{T_L}-C_3\right) + \left(\frac{\lambda}{h}\right)^2\left(\frac{\alpha_1}{\alpha_0}C_1^2 - \frac{\alpha_0}{\alpha_1}S_1^2\right)\left(\frac{\alpha_3}{\alpha_2}C_3\left(\frac{S_3}{T_L}-C_3\right) - \frac{\alpha_2}{\alpha_3}S_3\left(\frac{C_3}{T_L}-S_3\right)\right)\right) \\[2ex]
+ \frac{\lambda}{h}\alpha_0 V_{1x}C_1 S_1 C_2\left(ik V_m C_2(\alpha_1 - \alpha_2) + iS_2(\alpha_2 V_{1x} - \alpha_1 V_{2x}) - \frac{\lambda}{h}C_2\left(\frac{\alpha_2}{\alpha_1}-\frac{\alpha_1}{\alpha_2}\right)\right)\times \\[2ex]
\left(\frac{\alpha_3}{\alpha_2}C_3\left(\frac{S_3}{T_L}-C_3\right) - \frac{\alpha_2}{\alpha_3}S_3\left(\frac{C_3}{T_L}-S_3\right)\right) \\[2ex]
- i\frac{\lambda}{h}\alpha_3 V_{2x}S_3 C_2\left(k V_m C_2(\alpha_1 - \alpha_2) + S_2(\alpha_2 V_{1x} - \alpha_1 V_{2x})\right)\left(\frac{\alpha_1}{\alpha_0}C_1^2 - \frac{\alpha_0}{\alpha_1}S_1^2\right)\left(\frac{S_3}{T_L}-C_3\right) \\[2ex]
+ C_2^2\left(\frac{\lambda}{h}\right)^2 \alpha_3 V_{2x}S_3\left(\frac{\alpha_1}{\alpha_0}C_1^2 - \frac{\alpha_0}{\alpha_1}S_1^2\right)\left(\frac{\alpha_2}{\alpha_1}-\frac{\alpha_1}{\alpha_2}\right)\left(\frac{S_3}{T_L}-C_3\right) \\[2ex]
+ S_1\left(k V_m(\alpha_1 C_2^2 - \alpha_2 S_2^2) + S_2 C_2(\alpha_2 V_{1x} - \alpha_1 V_{2x}) - i\frac{\lambda}{h}\left(\frac{\alpha_1}{\alpha_2}C_2^2 - \frac{\alpha_2}{\alpha_1}S_2^2\right)\right)\times \\[2ex]
\left(\alpha_0 V_{1x}S_1 \alpha_3 V_{2x} C_3\left(\frac{S_3}{T_L}-C_3\right) - \left(\frac{\lambda}{h}\right)^2 C_1\left(\frac{\alpha_1}{\alpha_0}-\frac{\alpha_0}{\alpha_1}\right)\left(\frac{\alpha_2}{\alpha_3}C_3\left(\frac{C_3}{T_L}-S_3\right) - \frac{\alpha_3}{\alpha_2}S_3\left(\frac{S_3}{T_L}-C_3\right)\right)\right) \\[2ex]
- \frac{\lambda}{h}\alpha_0 V_{1x}S_1^2\left(ik V_m(\alpha_1 C_2^2 - \alpha_2 S_2^2) + iS_2 C_2(\alpha_2 V_{1x} - \alpha_1 V_{2x}) + \frac{\lambda}{h}\left(\frac{\alpha_1}{\alpha_2}C_2^2 - \frac{\alpha_2}{\alpha_1}S_2^2\right)\right)\times \\[2ex]
\left(\frac{\alpha_2}{\alpha_3}C_3\left(\frac{C_3}{T_L}-S_3\right) - \frac{\alpha_3}{\alpha_2}S_3\left(\frac{S_3}{T_L}-C_3\right)\right) \\[2ex]
- C_2 S_1 \alpha_3 V_{2x}S_3\left(\frac{S_3}{T_L}-C_3\right)\left(\frac{k V_m}{S_2}(\alpha_1 C_2^2 - \alpha_2 S_2^2) + C_2(\alpha_2 V_{1x} - \alpha_1 V_{2x})\right)\left(\alpha_0 V_{1x}S_1 - i\frac{\lambda}{h}C_1\left(\frac{\alpha_1}{\alpha_0}-\frac{\alpha_0}{\alpha_1}\right)\right) \\[2ex]
+ S_1 \alpha_3 V_{2x}\frac{\lambda}{h}\left(\frac{S_3}{T_L}-C_3\right)\left(\frac{\alpha_1}{\alpha_2}C_2^2 - \frac{\alpha_2}{\alpha_1}S_2^2\right)\left(i\alpha_0 V_{1x}S_1 S_3\frac{C_2}{S_2} - \frac{\lambda}{h}C_1 C_3\left(\frac{\alpha_1}{\alpha_0}-\frac{\alpha_0}{\alpha_1}\right)\right) \\[2ex]
- \alpha_0 V_{1x}S_1^2 C_2\frac{\lambda}{h}\left(\begin{array}{c}\frac{i}{S_2}k V_m(\alpha_1 C_2^2 - \alpha_2 S_2^2) + iC_2(\alpha_2 V_{1x} - \alpha_1 V_{2x}) + \frac{1}{S_2}\frac{\lambda}{h}\left(\frac{\alpha_1}{\alpha_2}C_2^2 - \frac{\alpha_2}{\alpha_1}S_2^2\right)x \\ \left(\frac{\alpha_3}{\alpha_2}C_3\left(\frac{S_3}{T_L}-C_3\right) - \frac{\alpha_2}{\alpha_3}S_3\left(\frac{C_3}{T_L}-S_3\right)\right)\end{array}\right) \\[4ex]
- i\frac{\lambda}{h}C_1 S_1 \alpha_3 V_{2x}C_3\left(k V_m(\alpha_1 C_2^2 - \alpha_2 S_2^2) + S_2 C_2(\alpha_2 V_{1x} - \alpha_1 V_{2x})\right)\left(\frac{\alpha_1}{\alpha_0}-\frac{\alpha_0}{\alpha_1}\right)\left(\frac{S_3}{T_L}-C_3\right)
\end{array} \right]$$

$$+\left[\begin{array}{l}+\frac{C_2}{S_2}S_1\left(\alpha_1 kV_m - i\frac{\lambda}{h}\frac{\alpha_1}{\alpha_2}\right)\left(\begin{array}{l}\alpha_0 V_{1x}S_1\alpha_3 V_{2x}S_3\left(\frac{S_3}{T_L}-C_3\right)+\left(\frac{\lambda}{h}\right)^2 C_1\left(\frac{\alpha_1}{\alpha_0}-\frac{\alpha_0}{\alpha_1}\right)\times\\ \left(\frac{\alpha_3}{\alpha_2}C_3\left(\frac{S_3}{T_L}-C_3\right)-\frac{\alpha_2}{\alpha_3}S_3\left(\frac{C_3}{T_L}-S_3\right)\right)\end{array}\right)\\[2em] +\frac{\lambda}{h}\frac{C_2}{S_2}S_1\left(i\alpha_1 kV_m + \frac{\lambda}{h}\frac{\alpha_1}{\alpha_2}\right)\left(\begin{array}{l}\alpha_0 V_{1x}S_1\left(\frac{\alpha_3}{\alpha_2}C_3\left(\frac{S_3}{T_L}-C_3\right)-\frac{\alpha_2}{\alpha_3}S_3\left(\frac{C_3}{T_L}-S_3\right)\right)-\\ C_1\alpha_3 V_{2x}S_3\left(\frac{\alpha_1}{\alpha_0}-\frac{\alpha_0}{\alpha_1}\right)\left(\frac{S_3}{T_L}-C_3\right)\end{array}\right)\\[2em] -\left(\frac{\lambda}{h}\right)^2 C_1 S_1\frac{C_2}{S_2}\left(\frac{\alpha_1}{\alpha_0}-\frac{\alpha_0}{\alpha_1}\right)\left(\frac{\alpha_1}{\alpha_2}C_2^2-\frac{\alpha_2}{\alpha_1}S_2^2\right)\times\\[1em] \left(\left(\alpha_2 S_3\left(\frac{C_3}{T_L}-S_3\right)-\alpha_3 C_3\left(\frac{S_3}{T_L}-C_3\right)\right)-\alpha_3 V_{2x}S_3\left(\frac{S_3}{T_L}-C_3\right)\right)\\[1em] -C_2 C_1 S_1\left(\frac{\lambda}{h}\right)^2\left(\frac{\alpha_1}{\alpha_0}-\frac{\alpha_0}{\alpha_1}\right)\left(\frac{\alpha_3}{\alpha_2}C_3\left(\frac{S_3}{T_L}-C_3\right)-\frac{\alpha_2}{\alpha_3}S_3\left(\frac{C_3}{T_L}-S_3\right)\right)\times\\[1em] \left(\frac{kV_m}{S_2}(\alpha_1 C_2^2-\alpha_2 S_2^2)+C_2(\alpha_2 V_{1x}-\alpha_1 V_{2x})-\frac{i}{S_2}\frac{\lambda}{h}\left(\frac{\alpha_1}{\alpha_2}C_2^2-\frac{\alpha_2}{\alpha_1}S_2^2\right)\right)\end{array}\right]$$

APPENDIX D. REDUCING THE CUBIC EQUATION TO QUADRATIC

The cubic equation for linear instabilities of tidal currents through a bounded inlet reduces to the quadratic equation that Bowen and Holman (1989) solved for in the nearshore over a flat bottom with no friction ($\lambda = 0$). The cross-inlet distance (x) is measured slightly differently in the bounded tidal inlet problem here vs. the nearshore problem since there is an additional region, as shown in Table D-1.

Table D-1. The cross-channel distances in the x-direction marked by region boundaries.

Cross-Inlet Location	Bowen and Holman, 1989	Bounded Tidal Inlet
Region 0 meets Region 1	x = 0 (no Region 0)	$x_1 = \gamma_1 x_0$
Region 1 meets Region 2	$x = x_0 \delta$	$x_2 = x_0(\gamma_1 + \delta)$
Region 2 meets Region 3	$x = x_0$	$x_3 = x_0(\gamma_1 + 1)$
Total cross-channel or inlet distance, x_{max}	$x_{max} = \infty$ (extends seaward without bound)	$x_{max} = x_0(\gamma_1 + 1 + \gamma_2)$

To reduce the cubic equation to quadratic, Region 0 width is set to 0 to remove it and Region 3 width is set to infinity removing the boundary on one side of the flow, i.e. $\gamma_1 = 0$, $\gamma_2 = \infty$, respectively. In doing so, the bounded tidal inlet cross-channel distances marked by region boundaries align with Bowen and Holman (1989) as seen in Table D-1. By extending the last region to infinity, the stream function in the third region (i.e. ψ_3 = A₃ [sinh (kx) – tanh (kx$_{max}$) cosh (kx)]) is modified to allow for exponential decay of velocity since $x_{max} = \infty$ and tanh(∞) = 1. Numerically, setting $\gamma_2 \geq 3$ is nearly equivalent to setting Region 3 width to infinity since tanh(3) $\approx$ 1. To set a flat bottom across the channel in all regions, the fraction of depth (αh) in every region is set to 1, i.e. $\alpha_0 = \alpha_1 = \alpha_2 = \alpha_3 = 1$. Note C is shorthand for the hyperbolic cosine and S is shorthand for the hyperbolic sine. The indexing on C, S, and velocity (V) denotes the

location across the inlet, e.g. $S_1 = \sinh(kx_1) = 0$ where $x_1 = 0$. V_m is the max velocity and k is the wavenumber. Many terms cancel and the remaining equation is:

$$0 = \sigma^3[1] + \sigma^2[-kV_m - V_{2x}S_3(S_3 - C_3) + S_2(V_{1x} - V_{2x})(C_2 - S_2)]$$

$$+ \sigma[V_{2x}S_2(S_2C_3 - C_2S_3)(V_{1x} - V_{2x})(S_3 - C_3) + V_{2x}S_3kV_m(S_3 - C_3)] + [0]$$

Now dividing through by σ, letting $\Delta V_x = V_{1x} - V_{2x}$, where

$$V_{1x} = \frac{V_m - 0}{x_2 - x_1} = \frac{V_m}{x_2} = \frac{V_m}{x_0 \delta}$$

and

$$V_{2x} = \frac{0 - V_m}{x_3 - x_2} = \frac{-V_m}{x_3 - x_2} = \frac{-V_m}{x_0(1 - \delta)}$$

and rearranging, the resulting equation is the solution Bowen and Holman (1989) found in the nearshore:

$$0 = \sigma^2[1] + \sigma[\Delta V_x S_2(C_2 - S_2) + V_{2x}S_3(C_3 - S_3) - kV_m]$$

$$+ [\Delta V_x S_2 V_{2x} C_2 S_3(C_3 - S_3) + \Delta V_x S_2^2 V_{2x}(S_3 C_3 - C_3^2) - V_{2x}kV_m S_3(C_3 - S_3)]$$

Here, $S_2 = \sinh(kx_2)$, where $x_2 = x_0(\gamma_1 + \delta) = x_0\delta$ when Region 0 is set to 0, so $S_2 = \sinh(kx_0\delta)$, which Bowen and Holman (1989) called S_δ and similarly, $C_2 = C_\delta$. Since $S_3 = \sinh(kx_3)$, where $x_3 = x_0(\gamma_1 + 1) = x_0$ when Region 0 is set to 0, $S_3 = \sinh(kx_0)$, which Bowen and Holman (1989) called S_0 and similarly, C_3 is called C_0. Substituting in Bowen and Holman equivalent notation, including V_0 (the max velocity) for V_m, the quadratic solution for the nearshore is:

$$0 = \sigma^2 + \sigma[\Delta V_x S_\delta(C_\delta - S_\delta) + V_{2x}S_0(C_0 - S_0) - kV_0]$$

$$+ [\Delta V_x S_\delta V_{2x} C_\delta S_0(C_0 - S_0) + \Delta V_x S_\delta^2 V_{2x}(S_0 C_0 - C_0^2) - V_{2x}kV_0 S_0(C_0 - S_0)]$$

APPENDIX E. UNSTABLE MOTIONS IN THE PISCATAQUA RIVER

The presence of instabilities of tidal currents flowing through an inlet in the form of rigid-lid low frequency motions, $O(10^{-4} - 10^{-2} \text{ s}^{-1})$ with dominant wavenumbers, $O(10^{-3} - 10^{-2} \text{ m}^{-1})$, that propagate horizontally in the direction of the mean current at a fraction (30 – 70%) of the max current, have been observed (Chapter III) consistent with observations in the nearshore (Oltman-Shay et al., 1989). The output from the numerical hydrodynamic model is analyzed to determine if unstable motions are present and consistent with lateral mixing of momentum under a nonzero horizontal Reynolds stress.

Wavenumber-frequency spectra are used to examine the character of unstable motions, and computed following methods described in Oltman-Shay et al. (1989), Chapter III, and summarized here. Eight virtual ROMS stations were placed in a spatially lagged array along the channel (Table E-1; Figure 4.6), each saving time series of velocities at each vertical level at 0.5 second time intervals. For model Run A, the time series stations 1 - 7 were analyzed over the last two hours of the model run. For model Run C, the time series stations 1 – 6 were analyzed over the last three hours of the model run after the model had spun up. The total length of the array was shortened by not including station 8 in Run A and 7 and 8 in Run C to maintain coherence along the array. The velocity at each station was detrended by regressing against a quadratic to remove low frequency changes to the mean current due to changes in sea surface elevation similar to methods for analysis of surf zone instabilities (Oltman-Shay et al., 1989). For a spatially lagged, linear array that is short relative to the wavelengths of interest, the iterative maximum likelihood estimator (IMLE) developed by Pawka (1982, 1983) can be used to estimate the wavenumber-frequency spectrum of the long wavelength, low frequency motions (Pawka, 1983; Oltman-Shay and Guza, 1984, 1987; Oltman-Shay et al., 1989; Howd et al., 1992). Following Oltman-Shay and Guza (1984), a

Kaiser-Bessel cosine-taper data window with 50% overlap was applied prior to calculating the cross-spectral matrix and the IMLE beta and gamma parameters were set to 1 and 20, respectively. For all calculations, the IMLE wavenumber bin width was set to 0.001 m^{-1}.

Table E-1. Virtual station locations. The stations in the along-channel array are spatially lagging in longitude (x-direction). The stations in the cross-channel transect are equally spaced in latitude (y-direction) by 15 grid cells or 75 m. Stations italicized are in both the along- and cross-channel transects.

| Station number	Grid cell Location (x, y)	Cumulative Distance (m)	Depth (m)
Along-channel lagged array			
1	*(137, 65)*	*0*	*14.4*
2	(151, 65)	70	14.6
3	(157, 65)	100	15.5
4	(167, 65)	150	17.5
5	(171, 65)	170	18.2
6	(195, 65)	290	25.7
7	(215, 65)	390	26.8
8	*(260, 65)*	*615*	*26.3*
Cross-channel transects			
T1	x = 137		
T2	x = 200		
T3	x = 260		

When calculating spectra, velocity data were windowed using a Hanning taper and ensemble averaged using 8 ensembles with no overlap resulting in 16 degrees of freedom (DOF).

The normalized total velocity to pressure variance ratio, $R = \dfrac{\frac{\langle u^2 \rangle + \langle v^2 \rangle}{\langle p^2 \rangle}}{\frac{g}{h}}$, defined by Lippmann et al. (1999) was then calculated for each run and over the full array deployment time period. R can be used to estimate the fraction of gravity waves versus velocity instabilities that make up the infragravity frequency band; when $R \gg 1$, the infragravity band is dominated by velocity fluctuations consistent with rigid-lid motions and when $R \leq 1$, gravity waves are present and dominate in the infragravity band.

The time series of velocity at stations in the lagged array during both ebbing (Run A) and flooding (Run C) currents in the high Reynolds number condition show that the model spins-up over the first hour followed by growth of unstable motions (Figure E-1 and Figure E-2). The character of the ebbing flow qualitatively changes with the initial development of apparent longer period motions followed later by shorter oscillations (Figure E-1). The flooding flow is steadier than the ebb and does not change in character over time (Figure E-2).
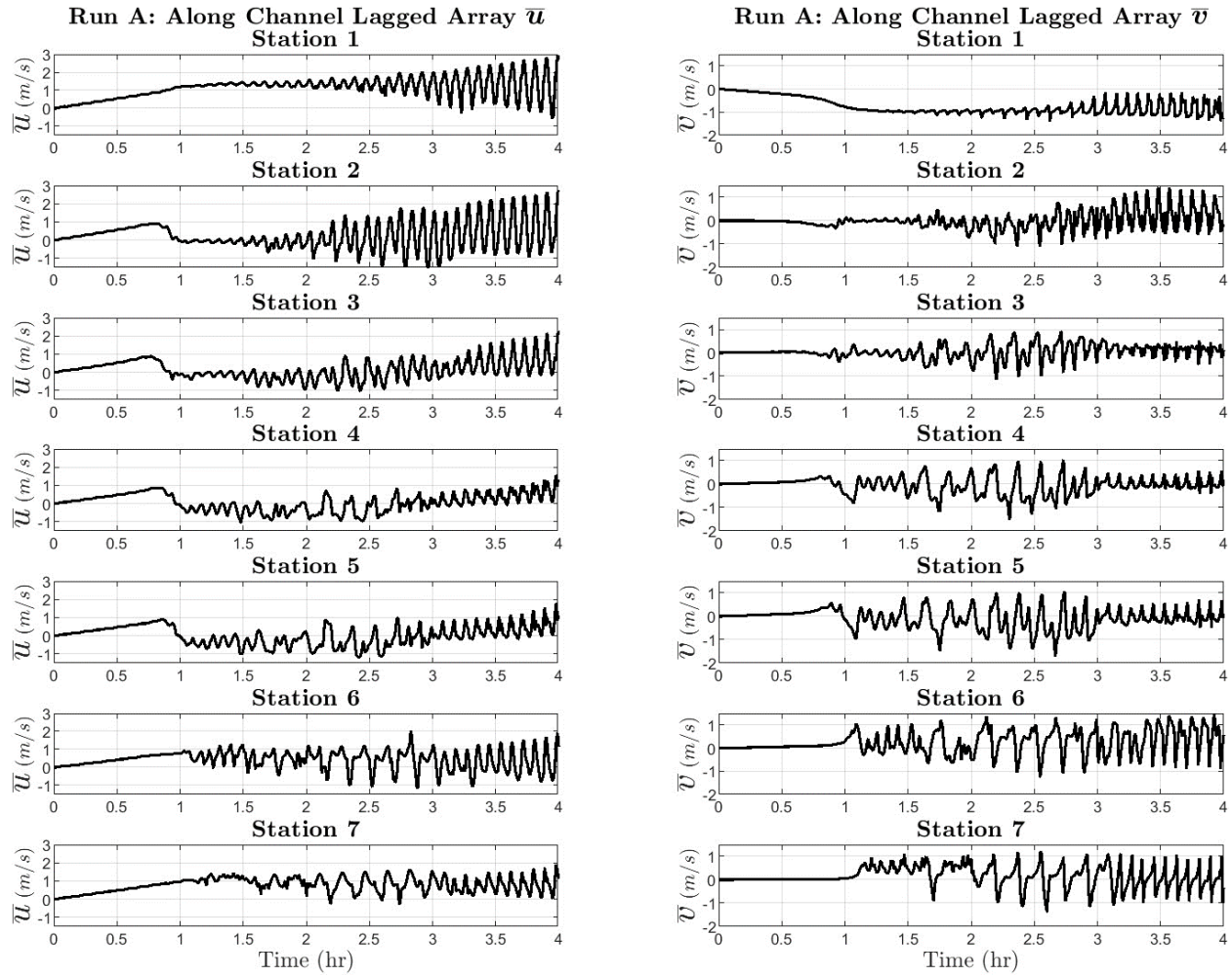
Figure E-1. Run A (ebbing flow). Depth averaged velocity, $\overline{u}$ (left column) and $\overline{v}$ (right column), for stations 1 (top) to 7 (bottom) in the along-channel lagged array.
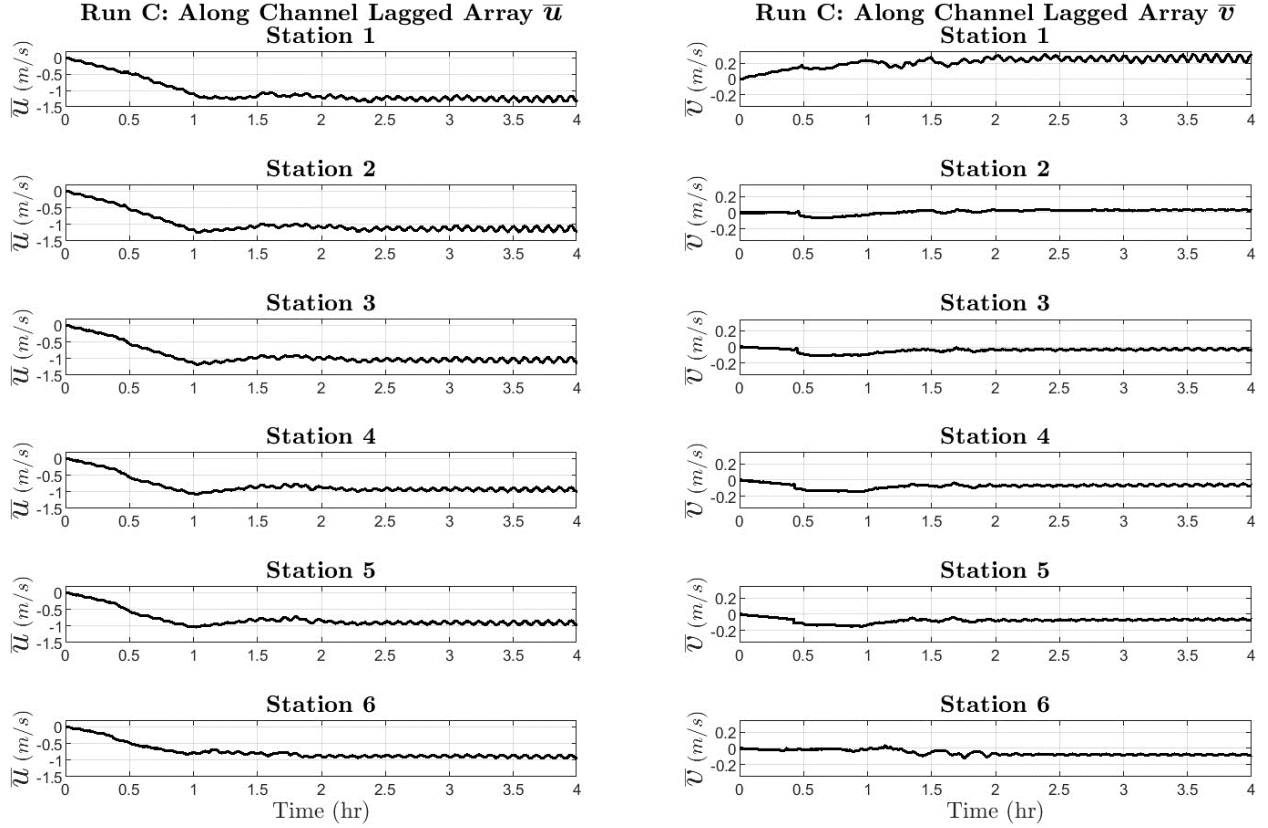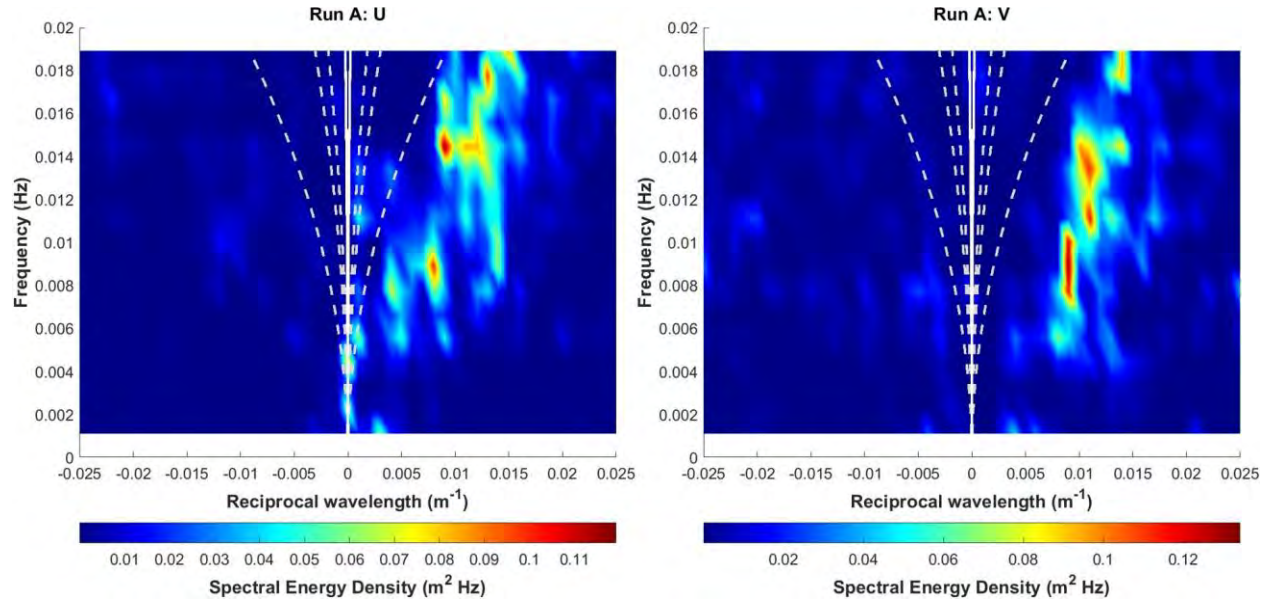
Figure E-2. Run C (flooding flow). Depth averaged velocity, $\overline{u}$ (left column) and $\overline{v}$ (right column), for stations 1 (top) to 6 (bottom) in the along-channel lagged array.

The wavenumber-frequency spectra for both the ebbing and flooding flow shows the energy is concentrated in narrow bands indicating the dominance of fastest growing unstable modes (Figure E-3 and Figure E-4). The unidirectional energy shows that the unstable motions propagate in the direction of the mean currents: for Run A, the energy is associated with positive wavenumbers indicating an eastward direction of propagation following the ebbing currents (Figure E-3) and for Run C, the energy is associated with negative wavenumbers indicating a westward direction of propagation following the flooding currents (Figure E-4).
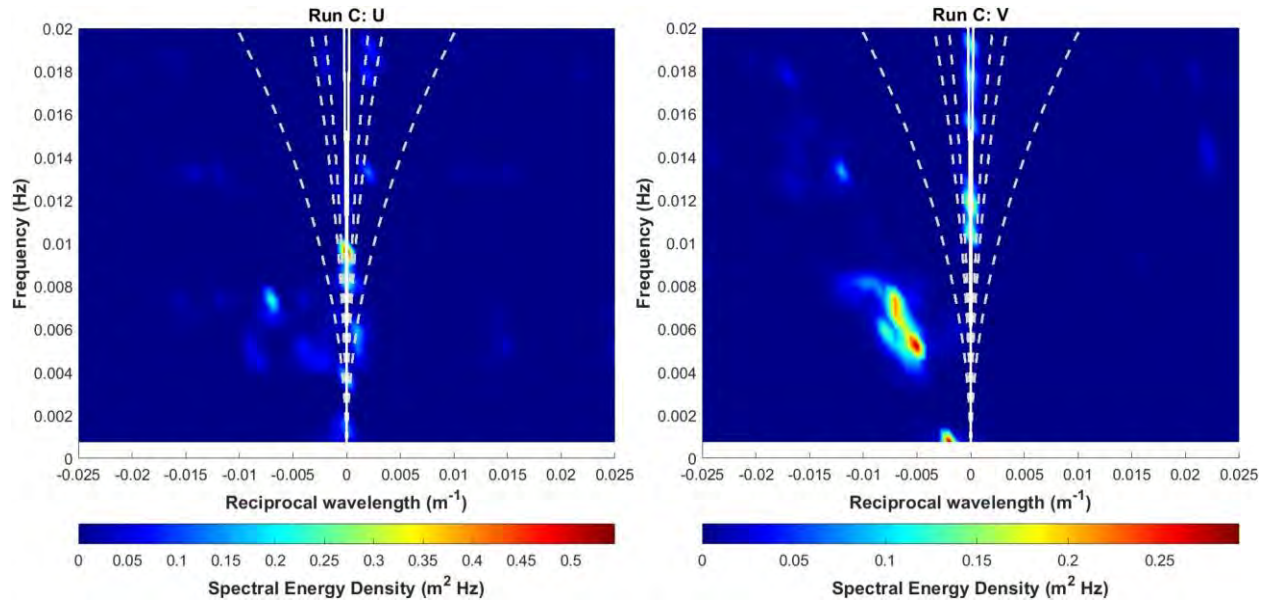
The phase speed of the unstable motions is roughly 1.2 m/s on the ebb (Run A) across stations 1 - 7 during the last two hours of the model run. The corresponding mean and max along-channel, depth-averaged current ($\overline{u}$) speed at stations $1 - 7$ on the ebb flow (Run A) are 0.54 m/s

and 2.90 m/s, respectively. Therefore, the phase speed is roughly 41% of the maximum current aligning with prior studies that have shown unstable motions generated from perturbations in the shear of the tidal current are expected to move between ½ - ¼ of the maximum along-channel current speed (Bowen and Holman, 1989).

Figure E-3. Run A (ebbing flow) wavenumber – frequency spectra of depth averaged velocity, $\bar{u}$ (left) and $\bar{v}$ (right). The white lines show the dispersion curves for leaky (solid) and edge (dashed) waves.

Figure E-4. Run C (flooding flow) wavenumber – frequency spectra of depth averaged velocity, $\bar{u}$ (left) and $\bar{v}$ (right). The white lines show the dispersion curves for leaky (solid) and edge (dashed) waves.

For flooding currents (Run C), the mean and max along-channel, depth-averaged current ($\bar{u}$) speed at stations 1 – 6 for the last three hours of the model run are 1.00 m/s and 1.36 m/s, respectively. The flooding mean along-channel current is 0.46 m/s faster than the mean ebb current, however the maximum flood current speed is 1.54 m/s slower than the maximum ebb speed. The corresponding phase speed of the unstable motions is roughly 0.52 m/s on the flood (Run C), which is approximately 38% of the maximum flood current, consistent with the ebb case and prior studies (Bowen and Holman, 1989; Oltman-Shay et al., 1989; Chapter II; Chapter III).

The nearly linear relationship in wavenumber-frequency space on both the ebb and flood current indicates these motions are non-dispersive, consistent with prior findings (Bowen and Holman, 1989; Church et al., 1992; Oltman-Shay et al., 1989; Chapter II; Chapter III). The velocity to pressure variance ratio normalized by the gravity wave speed, R, as defined by Lippmann et al. (1999) during both the flooding and ebbing currents shows high energy (> 1) in

low frequencies (10^{-3} - 10^{-2} Hz). This indicates the low frequency, unstable motions are consistent with horizontal, rigid-lid-like motions (Figure E-5 and Figure E-6). This suggests that perturbations in horizontal velocities are consistent with instabilities of the flow and contribute to lateral momentum mixing.

The strong horizontal shear at the study site supports the possibility for the growth of rigid-lid, unstable motions as observed in the wavenumber-frequency spectra using the spatially lagged array and the velocity to pressure variance ratio, R (Figure E-3, Figure E-4, Figure E-5, and Figure E-6). The instabilities observed in the ROMS model output are likely generated from perturbations in the shear of the tidal currents. It is worth noting that the instabilities of the mean flow are suppressed when either the bottom friction or the eddy viscosity is increased leading to smaller Reynolds numbers and weaker mean flow, consistent with previous studies (Bowen and Holman, 1989; Dodd and Thornton, 1990; Özkan-Haller and Kirby, 1999; Chapter II). The horizontal, rigid-lid, unstable motions propagate in the direction of the mean current at roughly 38-41% of the maximum current speed consistent with prior studies of instabilities of mean current in the nearshore (Bowen and Holman, 1989; Oltman-Shay et al., 1989; Dodd and Thornton, 1990) and in estuaries (Chapter II; Chapter III).
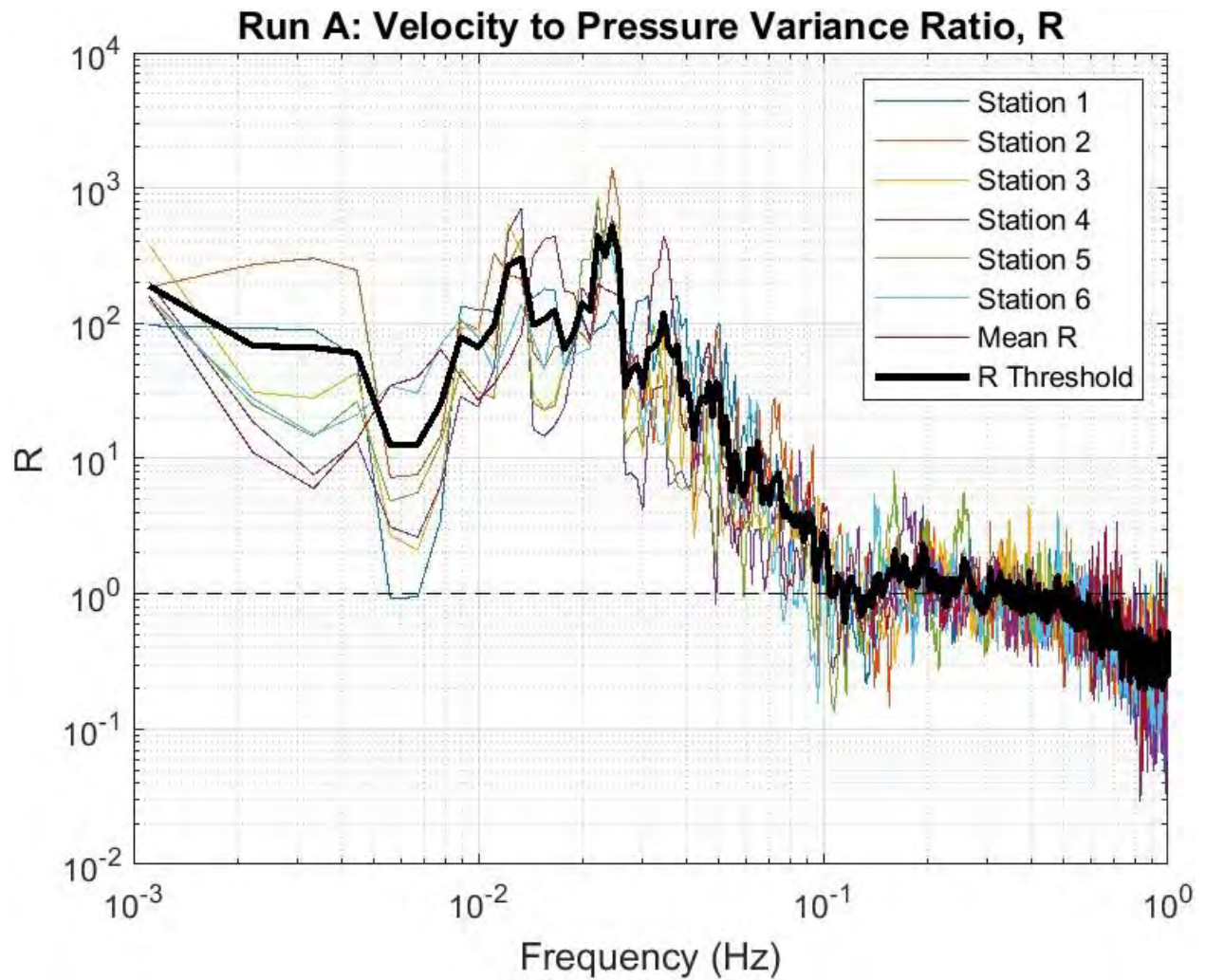
Figure E-5. Run A (ebbing flow) velocity to pressure variance ratio (R) for stations 1 – 7 and the mean across stations. The black dotted line is the R threshold.
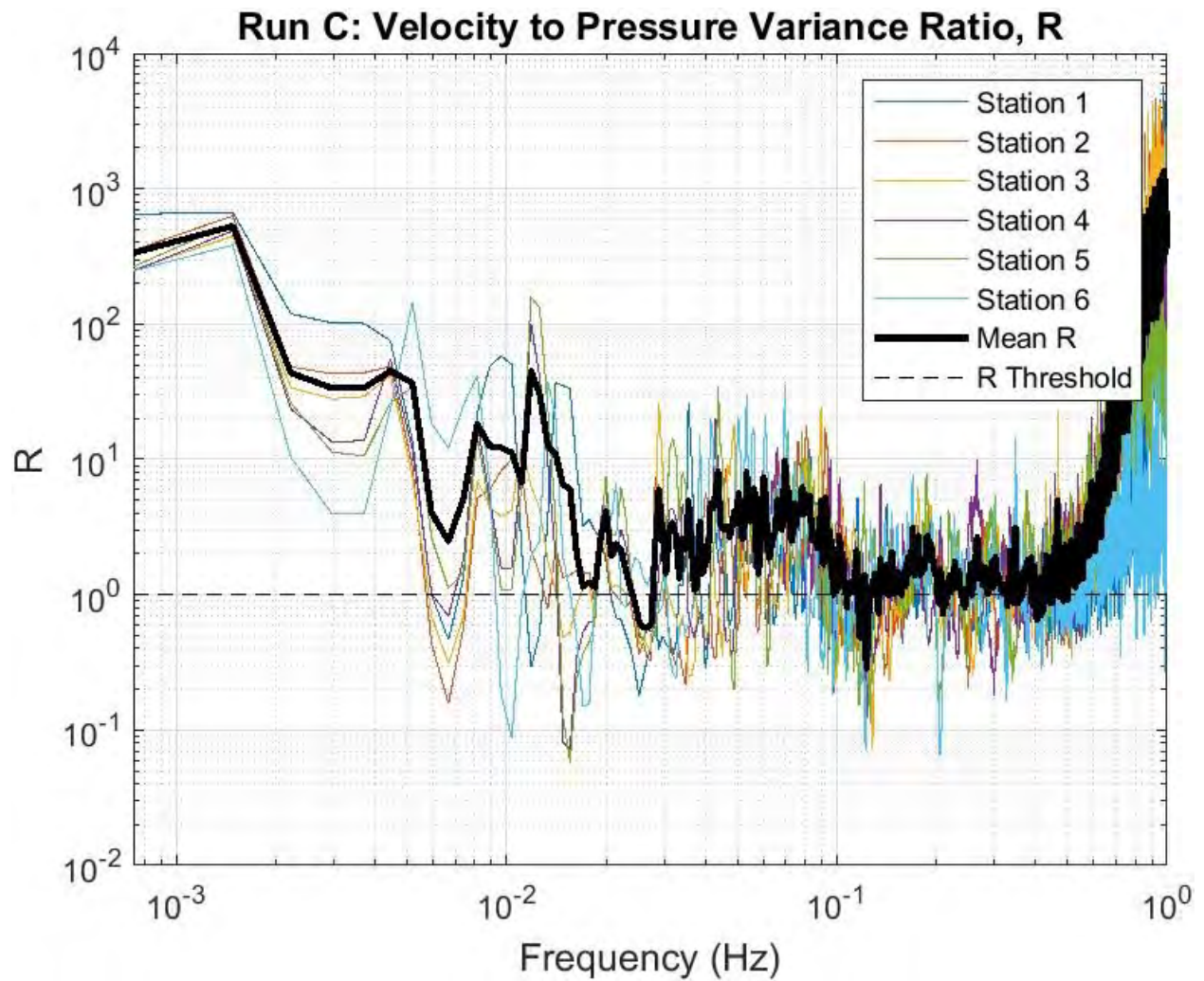
Figure E-6. Run C (flooding flow) velocity to pressure variance ratio (R) for stations 1 – 6 and the mean across stations. The black dotted line is the R threshold.